

**UNIVERSITY OF SÃO PAULO  
SÃO CARLOS SCHOOL OF ENGINEERING**

**Marcel Araujo Clementino**

**Design and experimental verification of a smart  
piezoelectric pitch link for vibration attenuation**

**São Carlos**

**2019**

---

**Marcel Araujo Clementino**

**Design and experimental verification of a smart piezoelectric pitch link for vibration attenuation**

Thesis presented to São Carlos School of Engineering, University of São Paulo, as one of the requisites for obtaining the degree of Doctor in Sciences - Graduate Program of Mechanical Engineering.

Concentration Area: Aeronautics

Supervisor: Prof. Dr. Carlos De Marqui Jr.  
Co-supervisor: Prof. Dr. Fred Nitzsche



**São Carlos**

**2019**

I AUTHORIZE THE TOTAL OR PARTIAL REPRODUCTION OF THIS WORK,  
THROUGH ANY CONVENTIONAL OR ELECTRONIC MEANS, FOR STUDY AND  
RESEARCH PURPOSES, SINCE THE SOURCE IS CITED.

Catalog card prepared by Patron Service at "Prof. Dr. Sergio  
Rodrigues Fontes" Library at EESC/USP

C626d Clementino, Marcel Araujo  
Design and experimental verification of a smart  
piezoelectric pitch link for vibration attenuation / Marcel  
Araujo Clementino; promoters Carlos De Marqui Junior;  
co-promoter Fred Nitzsche. -- São Carlos, 2019.

Doctorate (Thesis) - Graduate Program in Mechanical  
Engineering and Research Area in Aircraft of the School of  
Engineering of São Carlos at University of São Paulo, 2019.

1. Vibration control. 2. Smart structures.  
3. Piezoelectricity. 4. Pitch link. 5. Helicopters. I. Title.

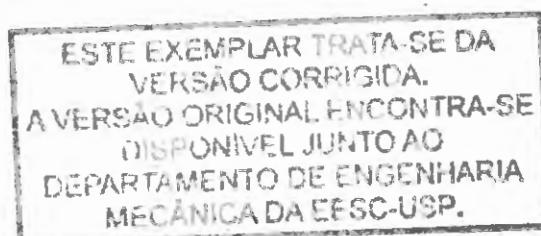
**Marcel Araujo Clementino**

**Projeto e verificação experimental de um pitch link  
piezelétrico inteligente para redução de vibração em  
helicópteros**

Tese apresentada à Escola de Engenharia de São Carlos da Universidade de São Paulo, para obtenção do título de Doutor em Ciências - Programa de Pós-Graduação em Engenharia Mecânica.

Área de Concentração: Aeronaves

Supervisor: Prof. Dr. Carlos De Marqui Jr.  
Co-supervisor: Prof. Dr. Fred Nitzsche



**São Carlos**

**2019**

Class.	TESE ✓
Cutt.	10.272
Tombo	T097/19
Sysno	2939663

31190213429

27.04.19

AUTORIZO A REPRODUÇÃO TOTAL OU PARCIAL DESTE TRABALHO, POR QUALQUER MEIO CONVENCIONAL OU ELETRÔNICO, PARA FINS DE ESTUDO E PESQUISA, DESDE QUE CITADA A FONTE.

Ficha catalográfica elaborada pela Biblioteca Prof. Dr. Sérgio Rodrigues Fontes da EESC/USP com os dados inseridos pelo(a) autor(a).

C626p	Clementino, Marcel Araujo Projeto e verificação experimental de um pitch link piezelétrico inteligente para redução de vibração em helicópteros / Marcel Araujo Clementino; orientador Carlos De Marqui Jr.; coorientador Fred Nitzsche. São Carlos, 2018.  Tese (Doutorado) - Programa de Pós-Graduação em Engenharia Mecânica e Área de Concentração em Aeronáutica -- Escola de Engenharia de São Carlos da Universidade de São Paulo, 2018.  1. Controle de vibração. 2. Estruturas inteligentes. 3. Piezeletricidade. 4. Pitch link. 5. Helicópteros. I. Título.
-------	--

Eduardo Graziosi Silva - CRB - 8/8907

## FOLHA DE JULGAMENTO

Candidato: Engenheiro **MARCEL ARAUJO CLEMENTINO**

Título da tese: "Projeto e verificação experimental de um pitch link piezelétrico inteligente para atenuação de vibração".

Data da defesa: 06.02.2019.

### Comissão Julgadora:

### Resultado:

Prof. Associado **Carlos De Marqui Junior**  
(Orientador)

(Escola de Engenharia de São Carlos/EESC)

Aprovado

Prof. Dr. **Leopoldo Pisanelli Rodrigues de Oliveira**

(Escola de Engenharia de São Carlos/EESC)

APROVADO

Prof. Dr. **Domingos Alves Rade**

(Instituto Tecnológico de Aeronáutica/ITA)

A PROVADO

Prof. Dr. **Luiz Carlos Sandoval Góes**

(Instituto Tecnológico de Aeronáutica/ITA)

APROVADO

Prof. Dr. **Paulo José Paupitz Gonçalves**

(Universidade Estadual Paulista "Júlio de Mesquita Filho"/UNESP - Bauru)

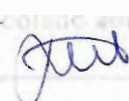
APROVADO

Coordenador do Programa de Pós-Graduação em Engenharia Mecânica:

Prof. Associado **Gherhardt Ribatski**

Presidente da Comissão de Pós-Graduação:

Prof. Associado **Luís Fernando Costa Alberto**

18 04 2019  


## ACKNOWLEDGEMENTS

First and foremost, I am thankful for the person I have become, blessed for having a great family and friends by my side and, especially, for being healthy to follow this work until the end.

I also would like to extend my deepest gratitude to Prof. Carlos De Marqui Jr., my supervisor, for he has been more than an academic advisor during these years. His advises and comments along our conversations have helped me a lot, always showing different ways and paths for the most different problems and difficulties I have encountered over the past years.

To Prof. Fred Nitzsche of Carleton University, for providing the infrastructure to carry out the experimental tests during my staying at Carleton University and also to Eng. Steve Vamosi, who was responsible for constructing and running the whirl tower test facility of Carleton University. His assistance was of great value for the development of the project during my staying in Canada.

To my lab colleagues, thank you for the companionship, conversations, lessons and collaboration during the whole process. I really appreciated the moments of distraction and friendship on our daily routine.

I am truly thankful for my family support, in special, my parents Rosemeri and Edson, and my girlfriend Mariany, for the support when I most need, continuously encouraging me to go ahead with career goals and personal challenges.

I also would like to thank the São Paulo Research Foundation (FAPESP) who provided financial support for my PhD research project (grant number 2013/15264 – 3) and during my research internship abroad in Canada (grant number 2015/04804 – 2).

And many thanks to everyone that somehow contributed to the development and conclusion of this work.

*“O estudo, a busca da verdade e da beleza são domínios  
em que nos é consentido sermos crianças por toda a vida.”*

*Albert Einstein*



## ABSTRACT

CLEMENTINO, M. A. **Design and experimental verification of a smart piezoelectric pitch link for vibration attenuation.** 2019. 138p. Thesis (Doctorate) - São Carlos School of Engineering, University of São Paulo, São Carlos, 2019.

Piezoelectric materials have been extensively employed for vibration reduction purposes in different fields of engineering. In general, the vibration control systems are grouped as active and passive systems, using the inverse and direct piezoelectric effect, respectively. Recently, these materials have been connected to switching circuits to perform the nonlinear management of the electrical output (voltage/current), resulting in the semi-active and semi-passive controllers. Among all configurations presented in the literature, some might be directly compared to mechanical systems used for vibration reduction in helicopters, likewise the Active Pitch Link (APL), which employs the combination of springs to control the variation of the structural stiffness. Although the APL device provides the attenuation of relevant vibration frequencies in a helicopter, the dependence on an external voltage source and possible mechanical failures (due to constant friction) are pointed out as drawbacks of the system. Therefore, this work reports on the design and experimental tests of a new smart pitch link system using piezoelectric materials for vibration attenuation. Different synchronized switching control techniques were investigated for vibration attenuation at a target frequency. A series of experiments are reported, including bench top vibration tests and whirl tower tests. The new configuration proposed here refers to a solid-state electromechanical system to address the issues of the mechanical active pitch link and provide a similar vibration attenuation performance.

**Keywords:** vibration control, smart structures, piezoelectricity, pitch link, helicopters.

## RESUMO

CLEMENTINO, M. A. **Projeto e verificação experimental de um pitch link piezelétrico inteligente para redução de vibração em helicópteros**. 2019. 138p. Tese (Doutorado) - Escola de Engenharia de São Carlos, Universidade de São Paulo, São Carlos, 2019.

Os materiais piezelétricos têm sido amplamente utilizados em pesquisas que visam a atenuação de vibrações em diversos ramos da engenharia. Em geral, os sistemas de controle de vibrações são classificados como sistemas ativos e passivos, os quais utilizam, respectivamente, o efeito piezelétrico inverso e direto. Recentemente, estes materiais passaram a ser conectados a circuitos chaveados para o tratamento não linear de sua saída elétrica (tensão/corrente), resultando nos controladores semiativos e semipassivos. Dentre as diversas configurações apresentadas na literatura, algumas podem ser diretamente comparadas com sistemas mecânicos utilizados para a redução de vibrações em helicópteros, como é o caso do *Active Pitch Link* (APL), o qual possibilita a combinação de molas para controlar a variação de sua rigidez. Embora este dispositivo proporcione a atenuação de frequências relevantes para helicópteros, alguns pontos negativos são apontados, como a dependência de uma fonte externa de energia para seu funcionamento e possibilidade de falhas mecânicas (devido ao atrito constante). Deste modo, o objetivo deste projeto é desenvolver um *pitch link* inteligente, utilizando materiais piezelétricos, do qual se espera ter bom desempenho na redução de vibrações e evitar problemas típicos de sistemas mecânicos, como o APL. Diferentes técnicas de controle foram utilizadas com o novo pitch link visando reduzir vibrações de uma frequência alvo. Esta tese descreve as atividades realizadas durante o desenvolvimento deste projeto e apresenta os resultados obtidos a partir de uma série de ensaios experimentais realizados com o dispositivo proposto, incluindo ensaios de vibração em bancada e ensaios rotativos. A nova configuração proposta refere-se a um sistema eletromecânico em estado sólido, proposto para tentar solucionar os problemas envolvidos com um pitch link mecânico, fornecendo um desempenho similar em termos de atenuação de vibração.

**Palavras-chave:** controle de vibração, estruturas inteligentes, piezeletricidade, *pitch link*, helicópteros.

## LIST OF FIGURES

Figure 1 – Vibratory load path in a helicopter (AUSTRUY, 2011). . . . .	27
Figure 2 – Helicopter main rotor hub components (DOMKE, 1988). . . . .	28
Figure 3 – Schematics of passive shunt circuits: (a) resistive shunt; (b) inductive shunt and (c) capacitive shunt. . . . .	34
Figure 4 – Schematics of semi-passive shunt circuits: (a) State Switching; (b) SSDS and (c) SSDI. . . . .	36
Figure 5 – Voltage waveforms for (a) open circuit, (b) SSDS and (c) SSDI cases. . . . .	39
Figure 6 – Schematics of the SSDV circuit. . . . .	41
Figure 7 – Typical waveforms for (a) SSDVa, (b) SSSC-H (hardening) and (c) SSSC-S (softening) cases. . . . .	42
Figure 8 – Combination of ACT, ACF and APL controllers composing a hybrid vibration control device (FESZTY; NITZSCHE, 2011). . . . .	44
Figure 9 – (a) The schematics of the Smart Spring mechanism and the evolution of the APL prototypes: (b) first generation, 2003; (c) second generation, 2006; and (d) third generation, 2010 (NITZSCHE; D’ASSUNCAO; De Marqui Jr., 2015) . . . . .	46
Figure 10 – (a) The prototype of a piezohydraulic pitch link proposed by John, Wereley and Sirohi (2009), (b) the schematics of a fluidic pitch link (Scarborough III et al., 2014b) and (c) coupled fluidic pitch links (Scarborough III et al., 2014a). . . . .	46
Figure 11 – Schematics of a generic piezoelectric plate structure. . . . .	50
Figure 12 – Schematics illustrating the connection between the piezoelements and their respective circuits, a full-wave bridge rectifier and a switching circuit with voltage sources (SSDVa or SSSC, for example). . . . .	57
Figure 13 – Flow chart of the basic steps required to simulate a piezoelectric device coupled to electric/electronic circuits. . . . .	58
Figure 14 – (a) Schematics of a bimorph piezoelectric structure and (b) its respective model developed using ABAQUS software. . . . .	59
Figure 15 – Electromechanical FRFs comparing the results of De Marqui Jr., Erturk and Inman (2009), Erturk and Inman (2009) and the proposed modeling procedure. . . . .	59
Figure 16 – Schematics of the working principle of the SaPPL device. . . . .	62
Figure 17 – Schematics illustrating (a) the elementary structure of the SaPPL device and (b) the cymbal flextensional structure. . . . .	62

Figure 18 – Maximum mechanical stress on the elementary structure of the SaPPL when an harmonic load (frequency of 160 Hz and amplitude of 32 N) is employed. . . . .	64
Figure 19 – First 4 mode shapes of the elementary structure (with geometry simplification) simply-supported at the bottom metal cap. . . . .	65
Figure 20 – Schematics of the electromechanical structure of the SaPPL prototype illustrating its (a) tridimensional view and (b) working principle. . . . .	66
Figure 21 – Tensile testing results of SaPPL elementary structure material (AISI 5160) after tempering and oil quenching heat treating. . . . .	67
Figure 22 – Schematics showing the coding employed to identify each MFC element and elementary structure of the SaPPL device. . . . .	69
Figure 23 – Schematics of the SSDVa circuit (1 <sup>st</sup> version) that operates with a single piezoelectric element and adaptive voltage sources ( $V_{s1}$ and $V_{s2}$ ). . . . .	70
Figure 24 – Voltage waveform (output) of a half-wave rectifier circuit. . . . .	71
Figure 25 – Typical waveform of resulting voltage signal after the processing of SSDVa circuit. . . . .	73
Figure 26 – Schematics representing the 2 <sup>nd</sup> version of the SSDVa circuit. . . . .	74
Figure 27 – Voltage and displacement waveforms of the piezoelectric element resulting from the SSSC technique: (a) SSSC-H (hardening) and (b) SSSC-S (softening) cases. . . . .	77
Figure 28 – Schematics of the proposed circuit for damping or stiffness control. . . . .	78
Figure 29 – Equipment setup used during the experimental tests: (a) general view and (b) detailed view of the electromechanical beam and control circuit. . . . .	84
Figure 30 – (a) Effect of the control circuits on the first resonance frequency of the electromechanical beam subjected to clamped-free boundary condition and (b) comparison between the typical waveform signal (time series) for the SSDI and SSDVa cases. . . . .	85
Figure 31 – Experimental setup employed in the tests of SaPPL’s elementary structure considering the 2 <sup>nd</sup> version of the SSDVa circuit. . . . .	86
Figure 32 – Response of SaPPL’s elementary structure (enlarged version) under chirp excitation considering the open circuit condition and also the SSDVa and SSDI circuits. . . . .	87
Figure 33 – (a) Voltage time series for SSDVa and SSDI circuits illustrating the switching problem and (b) mechanical FRF obtained from the tests carried out for a lower inversion factor. . . . .	88
Figure 34 – (a) Mechanical FRF after connecting the capacitors (in series “—” and parallel “//”) to adjust the phase, with a detailed view for (b) the <b>softening</b> effect at the 1 <sup>st</sup> resonance frequency and (c) for the <b>hardening</b> effect at the 2 <sup>nd</sup> resonance frequency. . . . .	90

Figure 35 – (a) Mechanical FRF after connecting the capacitors (in series “—” and parallel “//”) to adjust the phase, with a detailed view for (b) the <b>hardening</b> effect at the 1 <sup>st</sup> resonance frequency and (c) for the <b>softening</b> effect at the 2 <sup>nd</sup> resonance frequency. . . . .	92
Figure 36 – Experimental setup used in the benchtop tests performed at Carleton University. . . . .	93
Figure 37 – (a) Phase angle between the MFC piezoelements for open circuit condition and (b) voltage waveform of MFC3 and MFC4 when the SSDVa control circuit is connected. . . . .	95
Figure 38 – (a) Effect of all controller circuits on the elementary structure when the inductor was set to attenuate vibrations of the first structural resonance frequency; (b) the effect of SSSC technique for hardening (SSSC-H) and softening (SSSC-S) cases tuned to attenuate a lower bandwidth (around 30 Hz); (c) Voltage frequency response of MFC3 (primary piezoelement) for open circuit condition and (d) frequency response of the output force when the voltage level of the external power supply was limited to 9V. . . . .	96
Figure 39 – Mechanical frequency response (output force) of the enlarged elementary structure for different excitation amplitudes. . . . .	97
Figure 40 – SaPPL device installed on the benchtop test setup: (a) Front view, (b) general view and (c) side view. . . . .	98
Figure 41 – Voltage frequency response of SaPPL device with (a) aluminum and (b) steel <i>upper handle</i> , considering all piezoelectric sets are in open circuit condition. . . . .	99
Figure 42 – Voltage frequency response of the SaPPL device with MFC elements connected in series to form the piezoelectric sets. . . . .	100
Figure 43 – Result of the static loading test performed with the core structure of the SaPPL device. . . . .	102
Figure 44 – The whirl tower facility of Carleton University: (a) control room and (b) test chamber. . . . .	103
Figure 45 – Perspective view of (a) the rigid pitch link installed in the Whirl Tower facility and (b) the experimental calibration curve of the strain gauge attached on the L-shaped bracket. . . . .	104
Figure 46 – Load results for the rigid pitch link spinning test showing (a) the whole time history, (b) a zoom view of the time history at nominal speed, (c) the normalized PSD signal and (d) the time and frequency results of 300 RPM. . . . .	105
Figure 47 – Prototype of the SaPPL device installed in the whirl tower facility: (a) perspective view and (b) side view. . . . .	106

Figure 48 – Vibratory load acting on the SaPPL device for different rotational speeds: a) whole time history, (b) zoom of time history at nominal speed and (c) the auto PSD of the load signal. . . . .	107
Figure 49 – Voltage time history and the respective auto PSD of <i>SaPPL-stiff</i> for all MFC sets in open circuit. . . . .	109
Figure 50 – Voltage time history and the respective auto PSD of <i>SaPPL-SF1</i> for all MFC sets in open circuit. . . . .	110
Figure 51 – Voltage time history and the respective auto PSD of <i>SaPPL-SF2</i> for all MFC sets in open circuit. . . . .	111
Figure 52 – (a) Effect of controller circuits on the SaPPL load spectrum (auto PSD) for the spinning rates tested and (b) the APL results for 600 RPM reported by Nitzsche, D’Assuncao and De Marqui Jr. (2015). . . . .	111
Figure 53 – Voltage time history of the primary set (Set 3), with emphasis at the switching moments, comparing the control circuits and open circuit condition for 100 RPM rotation speed. . . . .	113
Figure 54 – Voltage time history of the (a) Secondary Set (Set <i>EH3</i> ) and (b) EH Set (Set <i>EH1</i> ), comparing the effects of the control circuits with the open circuit condition for 100 RPM spinning test. . . . .	113
Figure 55 – (a) Magnitude and phase response of the MFC elements that compose (b) the new configuration of piezoelectric sets (u1-2 is the reference element to calculate the phase signal). . . . .	114
Figure 56 – (a) General view of SaPPL installed in the whirl tower with (b) emphasis in the hall effect sensor. . . . .	115
Figure 57 – (a) Block diagram of the new control circuit and (b) magnitude and phase response of the high pass analog filters designed. . . . .	116
Figure 58 – Load time history of all tests performed with the SSSC-H circuit (without the analog filter) for the 350 RPM spinning test. . . . .	117
Figure 59 – Normalized load comparing the performance of the SaPPL device without the filtering ability (the wider bars represent the OFF circuit condition and the narrower bars represent the ON condition). . . . .	118
Figure 60 – Voltage PSD of the signal generated by the primary and secondary sets without the filtering ability. . . . .	119
Figure 61 – Normalized load comparing the performance of the SaPPL device influenced by the filtering process (the wider bars represent the OFF circuit condition and the narrower bars represent the ON condition). . . . .	120
Figure 62 – Voltage PSD of the signal generated by the primary and secondary sets influenced by the filtering process. . . . .	121

## LIST OF TABLES

Table 1 - Parameters of the enlarged (version) elementary structure. . . . .	63
Table 2 - Parameters of elementary structure for enlarged and reduced versions. . .	67
Table 3 - Configuration relative to the input port of OpAmp1 to obtain hardening or softening effects. . . . .	80
Table 4 - Components of the SSSC control circuit. . . . .	94
Table 5 - Piezoelectric elements of the enlarged elementary structure used in each circuit tested during the benchtop tests conducted at Carleton University. . . . .	94
Table 6 - Phase shift between the MFC elements of the SaPPL device. . . . .	100

## LIST OF ABBREVIATIONS AND ACRONYMS

APL	Active Pitch Link
DOF	Degree of Freedom
EH	Energy Harvesting
ER	Electrorheological
MFC	Macro Fiber Composite
MR	Magneto-rheological
PSD	Power Spectral Density
SaPPL	Smart Piezoelectric Pitch Link
SHARCS	Smart Hybrid Active Rotor Control System
SSDI	Synchronized Switch Damping on Inductor
SSDS	Synchronized Switch Damping on Short-circuit
SSDV	Synchronized Switch Damping on Voltage
SSDVa	Synchronized Switch Damping on Adaptive Voltage
SSSC-H	Synchronized Switch on Stiffness Control - Hardening
SSSC-S	Synchronized Switch on Stiffness Control - Softening
VFD	Variable Frequency Drive



## LIST OF SYMBOLS

$\delta$	Represents variation
$\rho$	Mass density [kg/m <sup>3</sup> ]
$A$	Area [m <sup>2</sup> ]
$\dot{\mathbf{u}}$	Velocity vector in x-direction [m/s]
$\mathbf{A}$	State matrix
$\mathbf{B}$	Input matrix
$\mathbf{C}_o$	Output matrix
$\mathbf{D}_o$	Direct transition matrix
$\mathbf{I}$	Identity matrix
$\mathbf{n}$	Number of mode shapes
$\mathbf{q}$	Electric charge vector [C]
$\mathbf{u}$	Displacement vector in x-direction [m]
$\mathbf{v}$	Voltage vector [V]
$\mathbf{x}$	State vector
$\mathbf{y}$	Output vector
$F_c$	Body force [N]
$F_e$	External force [N]
$F_s$	Surface force [N]
$T_c$	Total kinetic energy [J]
$U$	Total potential energy [J]
$V$	Volume [m <sup>3</sup> ]
$W$	Virtual work done by external forces, surface forces and body forces
$W_e$	Electric work [J]
$()_p$	Subscript related to the piezoelectric element
$()_s$	Subscript related to the substructure (beam)

## CONTENTS

<b>1</b>	<b>INTRODUCTION</b> . . . . .	<b>27</b>
<b>1.1</b>	<b>Objective</b> . . . . .	<b>31</b>
<b>1.2</b>	<b>Layout of this dissertation</b> . . . . .	<b>31</b>
<b>2</b>	<b>LITERATURE REVIEW</b> . . . . .	<b>33</b>
<b>2.1</b>	<b>Active and passive techniques for piezoelectric vibration control</b> . . . . .	<b>33</b>
<b>2.2</b>	<b>Synchronized switch techniques for vibration control</b> . . . . .	<b>36</b>
2.2.1	Semi-passive piezoelectric control techniques . . . . .	36
2.2.2	Semi-active piezoelectric control techniques . . . . .	40
<b>2.3</b>	<b>Smart materials and devices for vibration control in helicopters</b> . . . . .	<b>43</b>
<b>2.4</b>	<b>Final remarks</b> . . . . .	<b>47</b>
<b>3</b>	<b>NUMERICAL MODEL OF AN ELECTROMECHANICALLY COU- PLED STRUCTURE</b> . . . . .	<b>49</b>
<b>3.1</b>	<b>General considerations on modeling of a piezoelectric structure</b> . . . . .	<b>50</b>
<b>3.2</b>	<b>Description of the modeling procedure</b> . . . . .	<b>55</b>
<b>3.3</b>	<b>Verification of the modeling procedure</b> . . . . .	<b>58</b>
<b>3.4</b>	<b>Final Remarks</b> . . . . .	<b>60</b>
<b>4</b>	<b>THE NEW SMART PIEZOELECTRIC PITCH LINK (SaPPL)</b> . . . . .	<b>61</b>
<b>4.1</b>	<b>Elementary structure of SaPPL device</b> . . . . .	<b>62</b>
<b>4.2</b>	<b>The electromechanical structure of the SaPPL device</b> . . . . .	<b>66</b>
<b>4.3</b>	<b>Piezoelectric control circuits</b> . . . . .	<b>69</b>
4.3.1	Damping control circuit - SSDVa technique . . . . .	70
4.3.2	Stiffness control circuit - SSSC technique . . . . .	76
<b>4.4</b>	<b>Final Remarks</b> . . . . .	<b>81</b>
<b>5</b>	<b>EXPERIMENTAL RESULTS</b> . . . . .	<b>83</b>
<b>5.1</b>	<b>Preliminary tests performed during the development of the control circuits</b> . . . . .	<b>83</b>
5.1.1	Case A - Bimorph beam connected to the 1 <sup>st</sup> version of the SSDVa circuit . . . . .	83
5.1.2	Case B - SaPPL's elementary structure connected to the 2 <sup>nd</sup> version of the SSDVa circuit . . . . .	85
5.1.3	Case C - SaPPL's elementary structure connected to the SSSC circuit . . . . .	89
<b>5.2</b>	<b>Benchtop tests of the SaPPL device</b> . . . . .	<b>97</b>
<b>5.3</b>	<b>Whirl tower tests of the SaPPL device</b> . . . . .	<b>102</b>
5.3.1	1 <sup>st</sup> series of tests: no target frequency/bandwidth defined . . . . .	106

5.3.2	2 <sup>nd</sup> series of tests: control circuit with filtering capabilities . . . . .	114
5.4	<b>Final Remarks</b> . . . . .	<b>120</b>
6	<b>FINAL REMARKS</b> . . . . .	<b>123</b>
6.1	<b>Future work</b> . . . . .	<b>124</b>
	<b>REFERENCES</b> . . . . .	<b>127</b>

## 1 INTRODUCTION

Helicopters are inherently associated to noise and vibrations due to different phenomena mainly related to fluid and structure interaction that occurs in the main rotor of the aircraft. The induced blade vibrations are transmitted to the fuselage (figure 1) through the rotor hub and control commands (pitch link, for instance - figure 2) affecting the comfort of crew and passengers, increasing the maintenance costs, reducing the aircraft lifespan and, ultimately, limiting the helicopter maximum forward speed (FESZTY; NITZSCHE, 2011).

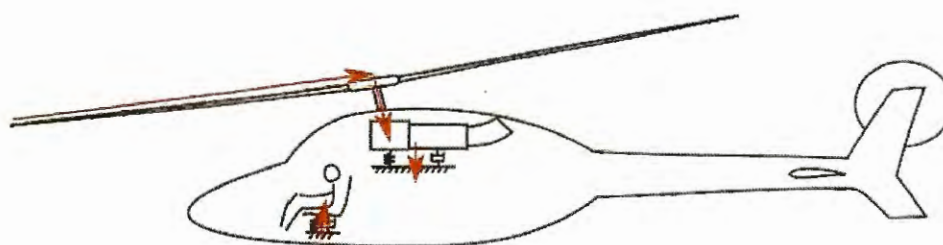


Figure 1 – Vibratory load path in a helicopter (AUSTRUY, 2011).

For an ideal rotor with identical blades, the frequency spectrum of the vibratory load transmitted through the main rotor and the pitch link commands is dominated by some specific harmonic frequencies, usually represented in the helicopter literature as  $pn/rev$ , which depends on the number of blades of the helicopter rotor ( $n$ ) and its rotating speed ( $rev$ ), with  $p$  being an integer number. Experimental results obtained from flight tests with a 4-bladed Bell-412 helicopter that were recently reported by Wickramasinghe (2012) indicated the vibration spectrum was mostly dominated by the  $4/rev$  (21.5 Hz) frequency at the fuselage and by the  $1/rev$  (5.4 Hz) frequency at the pilot and co-pilot bodies. According to Vallejo et al. (1998), the  $1/rev$  frequency, which typically ranges from 2 Hz to 8 Hz (depending on the size of the helicopter), is very close to the resonance frequency of a human's upper body (around 5 Hz). This vibration may cause human body fatigue and possibly health issues if a long exposure occurs. Therefore, reducing the vibration amplitude of the  $n/rev$  frequency and its harmonics, in that case, would benefit the crew as well as the aircraft structure.

Although advances have been achieved on helicopter vibration control for the last fifty years, with the vibration level dropping from 0.5g to 0.1g mostly due to passive solutions as linear and nonlinear mechanical vibration absorbers, it still seems to be a relevant contemporary theme. Moreover, the vibration level of 0.02g recommended by NASA Research and Technology Advisory Council Subpanel on Helicopter Technology, in 1976, has not been reached so far. In this sense, there is still groundbreaking challenges

remaining to achieve this goal.

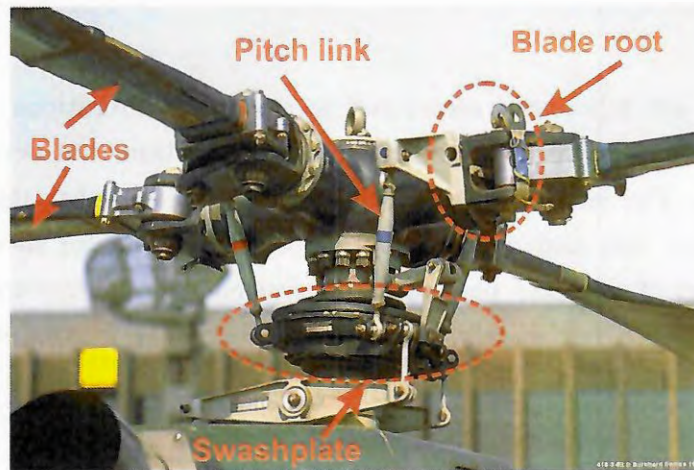


Figure 2 – Helicopter main rotor hub components (DOMKE, 1988).

Regarding helicopter applications, the vibration control systems can be either of fuselage-based type, where the controller (typically an actuator) is resonated at a certain adjustable frequency to counteract cabin vibrations, or rotor-based type, which aims to mitigate the vibrations at the rotor blade itself (FESZTY; NITZSCHE, 2011) or reduce its transmission to the fuselage. Although both approaches have gained much attention in the last four decades, the rotor-based ones are those with more recent advances. Friedmann and Millott (1995), Friedmann (2014), Kessler (2011a), Kessler (2011b) presented review papers that cover most of the techniques that have been studied, in special, the Higher Harmonic Control (HHC) and Individual Blade Control (IBC) systems. According to Friedmann (2014) these techniques consist of introducing time-dependent pitch inputs to the blades in order to modify the unsteady aerodynamic loads acting on them, therefore modifying the vibratory loads at the source before they propagate into the fuselage. The difference between them is that HHC introduces the pitch inputs through the swash plate (non-rotating part of the rotor) whereas in the IBC technique each blade is individually controlled on the blade or at its root, directly in the rotating frame. Hence, IBC allows different control inputs to each blade and overcomes the limitations of HHC, which provides the same pitch input to all blades. The IBC systems can be divided into four categories: the Actively Controlled Flap (ACF), Active Twist Rotor (ATR) and Active Controlled Tip (ACT), which consist of including actuators in the blade structure in order to change the blade dynamic characteristics such that the vibratory load produced are mitigated; and the Active Pitch Link (APL) that usually comprehend control devices placed between the swash plate and blades in order to attenuate (or even eliminate) the vibration transmitted to the fixed frame of the helicopter. Several researchers have investigated the use different devices and techniques in wind tunnel, whirl tower and flight tests (ROTH, 2004; KONSTANZER et al., 2008; GIURGIUTIU, 2000).

The main focus of this work is related to pitch link devices for vibration attenuation. One example is the patented Smart Spring device (NITZSCHE; GREWAL; ZIMCIK, 1999), which is a mechanical device capable of achieving effective modulation of its stiffness through the use of semi-active control strategies. The controlled change of the Smart Spring mechanical impedance has been investigated both experimentally (WICKRAMASINGHE; CHEN; ZIMCIK, 2008; NITZSCHE et al., 2004) and numerically (NITZSCHE et al., 2005) for vibration attenuation in fixed and rotary wing aircraft. Significant suppression of vibrations transferred from the rotating wing system of a helicopter to the non rotating system fixed to the fuselage is reported in the literature (OXLEY; NITZSCHE; FESZTY, 2009). An independent study also showed that the controlled modulation of the stiffness at the root of a helicopter blade could result in significant reduction of vibration energy at target frequencies (ANUSONTI-INTHRA; GANDHI, 2000). More recently, Nitzsche, D'Assuncao and De Marqui Jr. (2015) reported the successful experimental attenuation of vibrations at a specific frequency ( $2/rev$ ) by applying the smart spring concept into an Active Pitch Link (APL), which was associated to a dynamically and geometrically scaled helicopter blade during whirl tower tests. The smart spring mechanism and other semi-active pitch link devices are briefly discussed in chapter 2.

Although a good control performance has been observed, drawbacks related to the APL device has also been reported in the literature. As will be later discussed in details in this dissertation, the working mechanism of the APL is based on friction to engage/disengage springs, which can lead to early mechanical failure. Furthermore, the system requires external power to work, a significant issue in rotary systems. Therefore, this work presents the concept of an innovative piezoelectric based pitch link system that can be understood as a solid-state electromechanical version of the mechanical active pitch link.

Piezoelectric materials have the ability to exchange energy between mechanical and electrical domains, and thus, have been largely exploited in several active control applications as actuators (inverse piezoelectric effect) as well as in passive control, as sensors (direct piezoelectric effect), either simultaneously or separately. Although active control systems present good performance in vibration mitigation, they require external power and hardware. Piezoelectric passive controllers, on the other hand, are characterized by simple electrical circuits, but operate with good performance in a quite narrow bandwidth around the target frequency. Semi-passive and semi-active controllers have been pointed out as alternatives to address the issues of passive and active control systems. In general, the classification of semi-passive and semi-active techniques is based on the fact that external energy is directly applied (or not) to control the vibratory movement. In this sense, the semi-passive controllers might require external power to supply secondary systems that do not perform vibration control action but are essential to the process. In semi-active concepts, the vibration is suppressed by modulating the stiffness, damping or inertial

properties of a dynamic system. Hence, in most devices designed for semi-active control, the work done by the actuator forces is independent from the work done by the excitation forces that are the objective of control. Therefore, in contrast to active approaches, the power requirements are relatively low because the actuator forces are not used to directly counteract the vibratory motion. (NITZSCHE, 2012).

In this work different semi-passive and semi-active piezoelectric control techniques are investigated in order to verify the vibration attenuation performance of a new piezoelectric pitch link device. In particular, the switching techniques (GUYOMAR et al., 2000; RICHARD et al., 1999; RICHARD et al., 2000) that introduce the nonlinear treatment of the voltage output of the piezoelectric elements, inducing an increase in mechanical to electrical energy conversion, are of interest. Two semi-passive methods are explored, where the piezoelectric material is kept in open circuit condition except for a small period of time in which voltage is canceled due to switch to a small resistance (SSDS - Synchronized Switch Damping on Short-circuit) or inverted as a result of brief switching to an inductor (SSDI - Synchronized Switch Damping on Inductor). In a similar fashion, a semi-active approach that was developed to overcome the performance issues of the semi-passive SSDI technique is also investigated. The so-called Synchronized Switch Damping on adaptive Voltage (SSDVa) technique (GUYOMAR; LALLART; MONNIER, 2008; JI et al., 2009a; JI et al., 2009b; JI et al., 2010) performs the same switching operation to an inductance but includes additional external adaptive voltage sources to artificially complete the inversion of the SSDI method, which is limited due to internal losses of the switching circuit. Furthermore, another semi-active technique designated by Synchronized Switch Stiffness Control (SSSC) (GUYOMAR; LALLART; MONNIER, 2008) changes the equivalent stiffness of the structure by performing the switch operation on zero displacement is also considered. In this case, two different effects can be obtained: softening (reduced stiffness) or hardening (increased stiffness).

In this sense, this work combines switching piezoelectric techniques to present a piezoelectric-based pitch link that includes, simultaneously, vibration control and energy harvesting capabilities, features that had never been observed in modified pitch links earlier presented in the literature, characterizing an original contribution of this work. The proposed device is a solid-state system, with simple design, which does not require mechanical engagement/disengagement to operate, reducing the risk of failures due to mechanical wear caused by friction. Moreover, the device is able to operate with damping enhancement and/or stiffness control purpose, according to the application requirement, being the switch circuit topology proposed also an original contribution of this work.

## 1.1 Objective

The main objective of this work is to develop, design and experimentally test the concept of a Smart Piezoelectric Pitch Link (SaPPL) device that should be able to mitigate the vibratory load transmitted from the rotating frame (main rotor) to the fixed frame (fuselage) of helicopters. The device basically comprehends a flexible structure with piezoelectric elements attached and an electronic control/energy harvesting circuit. The system (electromechanical structure and control circuits) yields increasing energy dissipation and/or changing the stiffness of the resulting pitch link (and, consequently, blade root region), by properly managing the electrical output of the piezoelectric elements. In addition, since the electromechanical structure disposes of several piezoelements, some of them might be used for energy harvesting and provide electrical power in the rotating frame of the aircraft. In the end, the proposed system will have vibration control and/or energy harvesting capabilities.

For that purpose, the following goals were established:

- Design the structural part of the smart pitch link using commercial finite element software as modeling tool;
- Design self-powered electronic circuits that refer to the concepts of the switching techniques using software dedicated to simulate electric/electronic circuits (Multisim, Simulink);
- Perform vibratory benchtop tests with the smart pitch link developed (structure + circuit) using an electrodynamic exciter;
- Manufacture a prototype of the proposed device that allows to carry out rotating experimental tests in a facility (whirl tower) that simulates, in a reduced scale, the behavior of a helicopter rotor;
- Perform the rotating experimental tests with the SaPPL prototype in the whirl tower facility.

## 1.2 Layout of this dissertation

The main body of this dissertation consists of 5 chapters focusing on describing the development of a smart device for vibration reduction in helicopters. Starting with the second chapter, the contents of this work is organized as follows:

The **second chapter** of this dissertation presents the literature review about vibration control using piezoelectric materials, essentially regarding the semi-passive and semi-active techniques as well as the pitch link devices already developed for vibration control in helicopters. The **third chapter** describes a modeling procedure that enables the



development of numerical simulations considering a piezoelectric-based electromechanical structure connected to electric circuits, which are both part of the new pitch link proposed. **Chapter 4** introduces the Smart Piezoelectric Pitch Link device, describing its main characteristics and working principle for both the electromechanical structure and control circuits that composes the SaPPL. **Chapter 5** describes the benchtop and rotational experimental tests carried out to characterize the behavior of the SaPPL device and asses its performance for different conditions tested, also presenting the corresponding results obtained. **Chapter 6** summarizes the results of this work and describes the future perspectives about the development of this research topic.

## 2 LITERATURE REVIEW

In the past decades, the scientific community has reported several investigations regarding the use of smart materials and devices in order to reduce or re-use the vibration energy available in different systems. Smart materials, which are defined in the literature as materials that exhibit coupling between different physical domains, have been frequently investigated in applications related to helicopters (SPANGLER; HALL, 1986; BARRET, 1990; CHOPRA, 1992; FABUNMI, 1991; STREHLOW; RAPP, 1992; FENN, 1992; STRAUB et al., 2004; CESNIK; SHIN, 2001; WALL et al., 2008; NITZSCHE et al., 2005) with emphasis to shape memory alloys (coupling between thermal and mechanical domains) and piezoelectric materials (coupling between electrical and mechanical domains). The so-called Individual Blade Control (IBC) methods, such as the Active Controlled Flap (ACF), Active Twist Rotor (ATR), Active Controlled Tip (ACT) and Active Pitch Link (APL), are a few alternatives that employ smart materials with the purpose of reducing helicopter vibration. In general, it is of interest that different IBC techniques are used simultaneously such that its main advantages are combined to improve general rotor performance.

The increased popularity of materials exhibiting piezoelectric properties, as the PVDF polymers (*PolyVinylidene Fluoride*), the Macro Fiber Composites (MFC) and the *Lead Zirconate Titanate* (PZT) ceramics, has mainly occurred due to the fact that these materials require few additional components to be used in different control applications as well as they do not rely on complex geometries to properly convert vibration to electric energy (BEEBY; TUDOR; WHITE, 2006). Besides, they operate efficiently within a wide frequency bandwidth, are ease to attach in metallic and composite structures and, if employed correctly, add low mass and volume to the structures they are attached to (DONG; MENG; PENG, 2006). Due to those characteristics, piezoelectric materials have been used in several vibration control systems including the passive, active, semi-passive and semi-active ones. The remainder of this section presents a literature review mostly focused on piezoelectric based vibration control systems and techniques since they are the basis for the pitch link device proposed in this dissertation. The last section focus on enhanced pitch link devices presented in the literature for vibration control, although reference is also made to other piezoelectric devices for rotor-based applications.

### 2.1 Active and passive techniques for piezoelectric vibration control

In active control cases, the piezoelectric elements are applied as actuators (through the inverse piezoelectric effect) and are attached along the flexible structure which vibration needs to be controlled. That is, such controllers are based on a limited number of actuators

that are strategically placed in a system of bigger dimensions and are responsible for reducing the structural vibration (QIU et al., 2009).

The first works on this subject (CRAWLEY; De Luis, 1987; HAGOOD; CHUNG; Von Flotow, 1990; CRAWLEY; LAZARUS, 1991; DOSCH; INMAN; GARCIA, 1992) were mainly concerned about modelling issues and development of control laws for active controllers with focus on vibration reduction of simple structures like beams and plates, for example. The literature also includes papers addressing vibration control issues due to aeroelastic phenomena such as flutter (HEEG, 1993; MCGOWAN et al., 1998) and buffeting (MOSES, 1997; MOSES, 1999; DÜRR, 1998; HOPKINS et al., 1998). However, the application of active controllers in different fields of engineering (including fixed and rotary wing aircraft, for example) is still a challenge due to the high power required to operate the actuators associated to issues regarding the additional equipment involved to power such actuators.

In passive methods, the electric energy converted through the direct piezoelectric effect is dissipated in the resistive part of a shunt circuit. The first applications of this effect (designated shunt damping effect) found in the literature include the resistive, inductive and capacitive circuits, as well as series and parallel association of those elements. The simplest case of such systems was first presented by Uchino and Ishii (1988) and includes a resistive shunt circuit (figure 3a), therefore, inducing structural damping due to the dissipation of mechanical energy in the form of Joule heating.

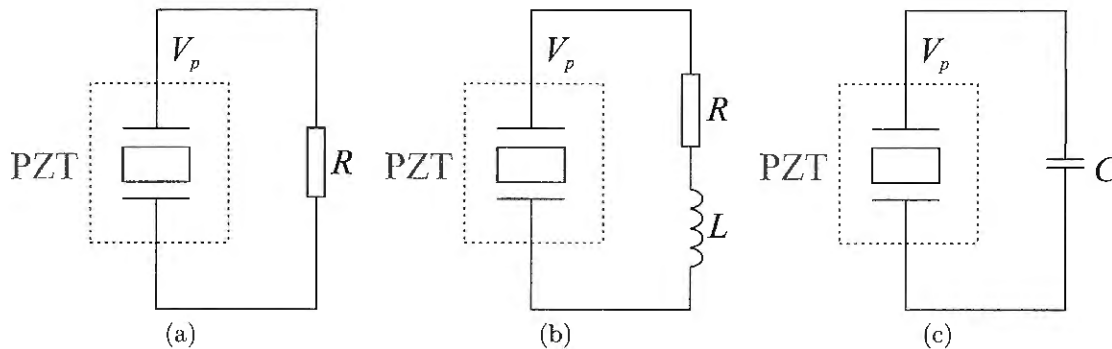


Figure 3 – Schematics of passive shunt circuits: (a) resistive shunt; (b) inductive shunt and (c) capacitive shunt.

On the other hand, an inductive shunt is the electromechanical analogous of an undamped mechanical absorber, originally presented by Forward (1979), likewise, adding a resistance in series with the inductor (series resistive-inductive shunt, figure 3b), in which the system behavior is equivalent to a damped mechanical absorber (HAGOOD; Von Flotow, 1991). In either case, the inductance ( $L$ ) forms a resonant circuit with the piezoelectric material, and the oscillation frequency of this new system is given by  $\omega_i^2 = (L - R^2 C_p)/(L^2 C_p)$  (WU, 1996), where  $\omega_i$  is the resonant frequency of the  $i$ th

structural mode shape and  $C_p$  is the capacitance of the piezoelectric material. Hence, selecting the appropriate values for  $R$  and  $L$  would lead to a reduction of the vibration associated to a specific frequency. In general, low frequencies ( $\omega_i < 50\text{Hz}$ , such as cases addressing aeroelastic vibratory loads like the present project) require high inductance values, around several hundreds of Henries, resulting in large and bulky inductors.

Following a similar concept, Wu (1996) presented a parallel resistive-inductive shunt circuit and pointed out a few issues related to the optimal resistance of the series resistive-inductive case presented by Hagood and Von Flotow (1991) such as optimal inductor and optimal resistor calculation. Moreover, Wu (1996) suggests that the parallel topology is less sensitive to changes in the resistive element. Hollkamp (1994), Dell'Isola, Maurini and Porfiri (2004) and Zhao (2010) extended the single frequency technique to a broader vibration bandwidth (i.e., multimodal vibration control). In such cases, the circuit is formed by several parallel resonant branches, each one tuned to a specific target frequency.

Finally, the capacitive shunt circuits (figure 3c) modify the effective stiffness of the electromechanically coupled structure. Edberg and Bicos (1991), Davis and Lesieutre (2000) investigated the use of capacitive shunt circuits, although this approach has not been much explored so far.

Nevertheless, it is important to point out that passive controllers have good performance around a target frequency (narrow bandwidth). That is, small variations in the target frequency might reduce the controller performance. In addition, low target frequencies require high inductance values, as already mentioned. In such cases, synthetic inductance circuits are pointed out as a solution. (EDBERG et al., 1992; FLEMING; MOHEIMANI, 2003; RIORDAN, 1967). However, the higher the inductance value (i.e. low frequency of interest) the higher is the internal resistance inherent to the synthetic inductor (VIANA, 2005). This may also affect the passive controller's performance since the equivalent resistance resultant from the synthetic circuit might differ from the optimal resistance value required to maximize the damping of the system. Researchers have also explored different types of nonlinear piezoelectric shunt circuits to enhance the vibration suppression bandwidth of piezoelectric absorbers. They include the tuned vibration absorber designed to attenuate vibrations of a nonlinear primary system (SOLTANI; KERSCHEN, 2015) and the practical implementation of a piezoelectric based nonlinear energy sink (SILVA et al., 2018). Piezoelectric semi-passive or semi-active switch shunting techniques introduce nonlinear treatment of the electrical output of piezoelectric elements and induce enhanced damping or stiffness modification in systems with weak electromechanical coupling - see the papers by Guyomar and co-workers (GUYOMAR; LALLART; MONNIER, 2008; RICHARD et al., 1999; RICHARD et al., 2000; LALLART et al., 2015) - as will be discussed in the next section.

## 2.2 Synchronized switch techniques for vibration control

Piezoelectric semi-passive or semi-active switch shunting techniques were introduced (RICHARD et al., 1999; RICHARD et al., 2000; CLARK, 2000; GUYOMAR; RICHARD; MOHAMMADI, 2007a; CORR; CLARK, 2002) to overcome the previously mentioned drawbacks of passive and active control techniques. In the semi-passive approach, the piezoelement is intermittently switched, synchronously with the structural motion, from open circuit to a specific electrical boundary condition (short circuit in the SSDS case or resonant circuit in the SSDI case). The nonlinear treatment of the electrical output of an electroelastic system increases the conversion of mechanical to electrical energy and consequently the shunt damping effect (ZHU; CHEN; LIU, 2012). In the semi-active approach, voltage sources are added to the external circuit in order to increase the dissipated energy (LEFEUVRE, 2006). In this section, the semi-passive (SSDS and SSDI) and semi-active (SSDVa and SSSC) methods are briefly presented and discussed. It is important to remember that different semi-passive and semi-active methods are included in the literature (CLARK, 2000; CORR; CLARK, 2002; LALLART; GUYOMAR, 2010) although not discussed in this section. Figure 4 shows the schematics of the main SSD techniques reported in the literature: (a) State Switching (SS), (b) Synchronized Switch Damping on Short (SSDS) and (c) Synchronized Switch Damping on Inductor (SSDI).

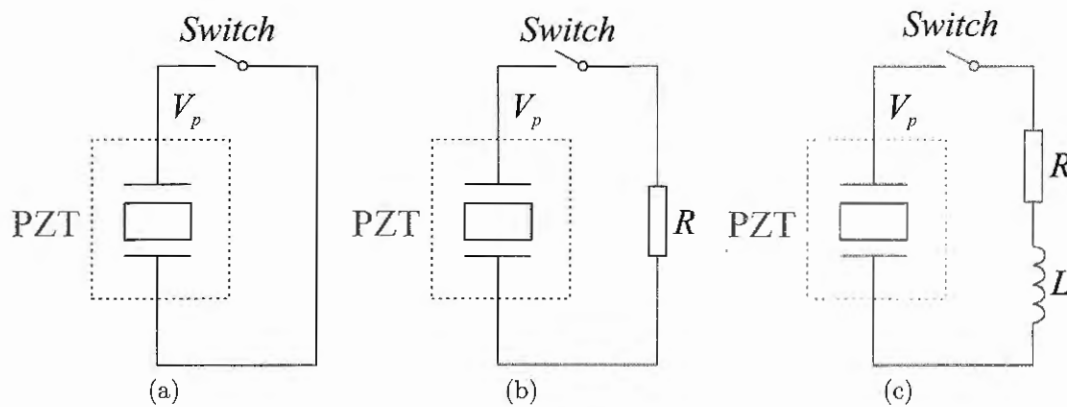


Figure 4 – Schematics of semi-passive shunt circuits: (a) State Switching; (b) SSDS and (c) SSDI.

### 2.2.1 Semi-passive piezoelectric control techniques

According to the classification criterion adopted in this dissertation, the semi-passive term is designated to techniques that do not directly apply external energy to the piezoelectric element. Nevertheless, external energy might be used to power secondary systems such as those accounting for switching actions.

One of the first semi-passive techniques reported in the literature is known as State Switching (SS) (figure 4a). This technique was first introduced by Larson and

Rogers (1994) applied to communication systems and later by Larson, Rogers and Munk (1998) in subaquatic SONAR applications. The SS technique consists of periodic switching operations, where the piezoelement is kept in open circuit state (maximum voltage and higher stiffness achieved) until a local maximum strain occurs. It is important to point out that once in open circuit, the piezoelement exhibits in-phase behaviour between voltage and displacement signals (ERTURK; INMAN, 2011). Thus, when a maximum displacement occurs, the circuit is switched to short circuit (or to a low resistance,  $R \rightarrow 0$ , which approximates to short circuit). This new electrical boundary condition remains until zero displacement occurs when the switch is turned off and the system operates in open circuit again. In other words, comparing to an harmonic motion, one may say the system is in open circuit while it moves away from the equilibrium state and in short circuit while it moves toward the equilibrium state. Since the switching process changes the structural stiffness between two discrete values every quarter of the oscillation period, it starts dissipating energy after the maximum displacement occurs. Consequently, less energy is available in every next period of oscillation and vibration attenuation is achieved.

Clark (1999) extended this approach and numerically investigated the SS technique applied to an electromechanically coupled cantilever. In a similar fashion, Clark (2000) numerically compared three different configurations: a resistive shunt, regular State Switching (SS) and the State Switching connected to a resistive shunt (SS-RS). The results showed that the regular SS and SS-RS techniques were less sensitive to changes on the resistance value, exhibiting good performance for low frequency ranges in broader bandwidth. However, the stiffness variation caused by the nonlinear change from short to open circuit state is small and leads to low energy dissipation per cycle of oscillation.

The SSDS method is a nonlinear semi-passive technique originally proposed by Richard et al. (1999) (figure 4b presents its schematics). The technique consists of switching the voltage signal from open to short circuit condition synchronously with mechanical oscillations. When a local maximum (or minimum) voltage is detected (which corresponds to maximum or minimum strain), the piezoelement is briefly switched to short circuit condition, canceling the voltage across its electrodes, and re-switched to open circuit condition until the next local maximum (or minimum) voltage (or strain) occurs again. The switching process provides a phase tuning between voltage and structural velocity signals, hence, increasing the dissipative contribution of the piezoelectric material in part of each oscillation cycle of the system. In addition, one might observe that the switching increases the voltage amplitude and, consequently, increases the electromechanical conversion. Figure 5a shows the voltage and displacement signals for the open circuit condition and figure 5b illustrates the voltage signal that results from the SSDS nonlinear processing.

The SSDI method is another nonlinear semi-passive method (RICHARD et al., 1999; RICHARD et al., 2000; GUYOMAR et al., 2000; PETIT et al., 2004). In this

approach, the switching circuit is composed of a switch and an external inductance ( $L$ ). The switch is briefly closed when a local maximum displacement (or voltage) is detected. At this point, the internal capacitance of the piezoelement ( $C_p$ ) and the inductance of the electrical circuit constitute an electrical oscillator. During the switch ON condition, the voltage of the piezoelement is inverted after half period of the electrical oscillator ( $\Delta t_i$ ), when the switch is opened again (LALLART et al., 2008). The inversion time is directly proportional to the inductance  $L$ ,

$$\Delta t_i = \left(\frac{T}{2}\right) = \pi\sqrt{LC_p}, \quad (2.1)$$

where  $T$  is the period of oscillation of the electrical circuit. In practice, the inductance ( $L$ ) is chosen to give an inversion time 20 – 50 times smaller than the period of mechanical vibration (BADEL et al., 2007) in order to provide a rapid inversion. Therefore, the SSDI technique does not require high inductances even when tuned to damp low mechanical frequencies. One should note that the inversion is not perfect since part of the energy stored in the piezoelement is lost in the switching device. The losses are related to the electrical quality factor  $Q$  and the voltage of the piezoelectric element ( $V_p$ ) after the inversion process may be written as,

$$V_p(t) = -V_0 \exp\left(-\frac{\pi}{2Q}\right) = -\gamma V_0, \quad (2.2)$$

where  $V_0$  is the voltage before the inversion,  $\gamma$  is the inversion coefficient and the negative sign implies that the voltage is inverted. The quality factor is given as,

$$Q = \frac{L\omega_{ne}}{R_i} = \frac{1}{R_i} \sqrt{\frac{L}{C_p}}, \quad (2.3)$$

where  $R_i$  is the internal resistance of the switching circuit and  $\omega_{ne}$  is the resonance frequency of the electrical circuit. The lower the internal resistance of the switching circuit the higher the quality factor and, consequently, the inversion factor tends to one. Since the inversion coefficient is related to the electrical quality factor (eq. 2.3), the SSDS method is a particular case of the SSDI with quality factor equal to zero and, consequently, the inversion coefficient is zero (MOHAMMADI, 2008). Figures 5a to 5c show the voltage and displacement waveforms for the semi-passive techniques (compared to open circuit condition) and illustrates the switching moments of both techniques.

Several researchers have been seeking to improve the performance of the semi-passive controllers regarding their dissipative characteristics in order to make their application more practical and realistic. Ducarne, Thomas and Deü (2010) investigated the behaviour of piezoelectric elements connected to SSDS and SSDI circuits in order to quantify the amount of energy dissipated and optimize the parameters of the system. The numerical investigation was performed with an electromechanical structure with 0.2 modal electromechanical coupling factor and 0.1% damping ratio and the results indicated the structural damping

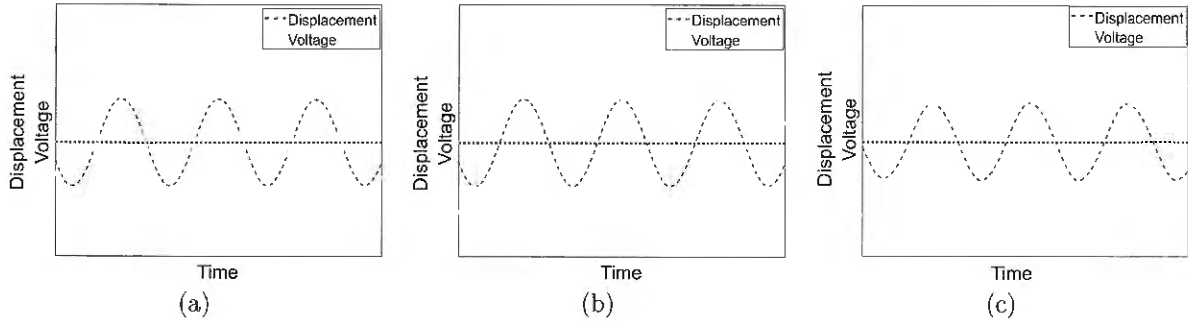


Figure 5 – Voltage waveforms for (a) open circuit, (b) SSDS and (c) SSDI cases.

was increased in, approximately, 2.5% for the SSDS case and approximately 10% for the SSDI.

Guyomar, Richard and Mohammadi (2007b) performed a statistical analysis that allowed the definition of a criterion to identify the switching point more accurately when random input signals were applied. In practice, the switch might occur before or after the maximum voltage point, which affects the performance of the switching controllers. Therefore, such analysis is fundamental for the development of semi-passive techniques. Based on the investigations of Guyomar, Richard and Mohammadi (2007b), Khodayari, Ahmadi and Mohammadi (2011) proposed an analogical adaptive circuit that compared the piezoelement's voltage signal to its statistical data (temporal average and standard deviation) to predict the next switching time instant. The circuit was able to reduce vibrations of a cantilever subjected to harmonic, impulsive and random excitations requiring low power supply, which could allow the development of a system powered by the energy converted by the piezoelectric element. However, the technical limitation of both studies relies on the fact that such statistical approach requires previous information of the system behavior to estimate the next switching points.

An alternative solution to avoid this issue is found in the circuit presented by Richard, Guyomar and Lefeuvre (2007). The authors proposed a self-powered electronic breaker that detects maximum/minimum voltage points and performs the switching operation. The circuit does not depend on external power supply in order to work properly and is able to execute the following tasks: detect the signal's envelope, compare the piezoelectric voltage and its envelope signal to determine the switching point and perform the switching operation. The internal resistance of the switching circuit is low and, therefore, the inversion factor is usually high. In practice, any switching circuit has internal resistance and part of the energy of the system is dissipated through the circuit. Zhu, Chen and Liu (2012) provides a more detailed analysis of the behaviour of the electronic switching breaker circuit.

In order to increase the electrical quality factor of SSDI circuits, Delpero et al.



(2011) presented an autonomous circuit that improves the switching circuit originally proposed by Niederberger and Morari (2006). Both approaches include two piezoelectric elements with vibration control purposes where one element is employed as sensor and generates a signal to detect the switching points using a low-pass filter, while the other is connected to the switching system and is subjected to the nonlinear processing of the SSDI technique. The difference, however, is that the circuit presented by Delpero et al. (2011) includes a nano operational amplifier as comparator that transforms the filtered signal in a square waveform and is applied to MOSFET transistors that account for the activation of the switching circuit. Those low-power components require a few microwatts to work and, therefore, might even be supplied by the sensor piezoelement in case a full wave rectifier circuit is used. After comparing both investigations one may observe that the circuit presented by Delpero et al. (2011) has the advantage of increasing the electrical quality factor and reducing the inversion time.

Chen et al. (2013) also presented an autonomous switching circuit for SSDI controllers. Nevertheless, instead of detecting maximum/minimum voltages, the circuit detects the zero velocity instant of the mechanical system, which corresponds to maximum displacement and maximum voltage of the electromechanical system when the piezoelement is in open circuit. The proposed system was able to determine the switching instants more accurately if compared to the conventional SSDI technique. Designated by the authors as Self-Powered Synchronized Switch Damping on Inductor (SP-SSDI), the proposed system requires three piezoelectric elements: one connected to the switching circuit whose electric output is processed according to the conventional SSDI technique; a second one, which is smaller, accounts for the energy harvesting and, therefore, supplies energy to the comparator circuit; and a third one that is employed as velocity sensor. A comparison between the SP-SSDI and SSDI circuits was performed using all three piezoelectric elements in both cases and the results indicated the SP-SSDI approach achieved an average efficiency<sup>1</sup> of 86%, approximately. In addition, the authors compared the performance of both techniques when only one piezoelement was employed in the SSDI case, reporting an average efficiency of 95% (in this case, the piezoelement and circuitry power supply were externally driven by a function generator and a power source, respectively). Nevertheless, in terms of absolute displacement the results of SP-SSDI did not outperformed the standard SSDI technique.

### 2.2.2 Semi-active piezoelectric control techniques

The semi-active techniques (SSDV and SSSC, for example) were developed as an improvement of the semi-passive ones. The SSDV method follows the control strategy of the SSDI approach combining the use of external voltage sources (figure 6) to artificially

<sup>1</sup> The authors define efficiency by  $\frac{u - u_{SP-SSDI}}{u - u_{SSDI}}$ , comparing the displacement of the uncontrolled case ( $u$ ) with the displacement of the SP-SSDI and SSDI cases.

increase the inversion coefficient (that is always smaller than the one discussed in the previous section) and, therefore, increase the control performance. The concept of switching the piezoelectric voltage to an external voltage source was first introduced by Petit et al. (2004). The authors compared the performance of SSDS, SSDI and SSDV approaches and reported that increasing the voltage across the piezoelement using the SSDV technique allows to enhance the control performance of structures with low piezoelectric coupling factor. Following the same line, Lefeuvre (2006) reported theoretical and experimental analysis of a piezoelectric cantilever beam connected to the SSD circuits. The results indicated the SSDV technique (using a symmetrical  $\pm 10V$  voltage source) could achieve similar vibration levels of SSDS and SSDI techniques with the benefit of reducing the volume of piezoelectric materials in approximately 86%.

Nevertheless, according to Badel et al. (2006) the use of constant voltage sources to improve the inversion factor could lead to instability. That is, as the vibration amplitude becomes lower the constant voltage sources could excite the structure subjected to vibration control. In attempting to overcome this issue, Badel et al. (2006) proposed the use of adaptive voltage sources (adaptive SSDV or SSDVa technique) where the amplitude of the voltage source relied on the magnitude of the piezoelectric voltage.

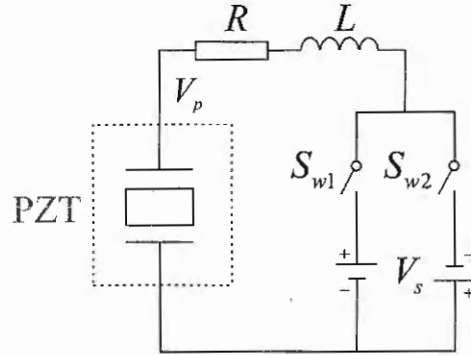


Figure 6 – Schematics of the SSDV circuit.

Figure (7a) shows the voltage waveform of the piezoelectric element when the SSDVa circuit is activated and the extra voltage ( $V_s$ ) supplied by the external voltage sources may be written as,

$$V_s = -\max(V_p) \operatorname{sgn}(V_p) \frac{\gamma_f - \gamma_{SSDI}}{1 + \gamma_{SSDI}}, \quad (2.4)$$

where  $\gamma_{SSDI}$  is the inversion factor of SSDI technique (without applying the extra voltage),  $\gamma_f$  is the final inversion factor that resulted from the SSDVa process and  $\operatorname{sgn}(V_p)$  is the sign function of  $V_p$ . Equation (2.4) provides means of defining the voltage level ( $V_s$ ) based on the desired value for the final inversion coefficient  $\gamma_f$ .

Many researchers have been working on semi-active piezoelectric-based techniques (MARNEFFE; PREUMONT, 2008; GUYOMAR; LALLART; MONNIER, 2008; JI et al.,

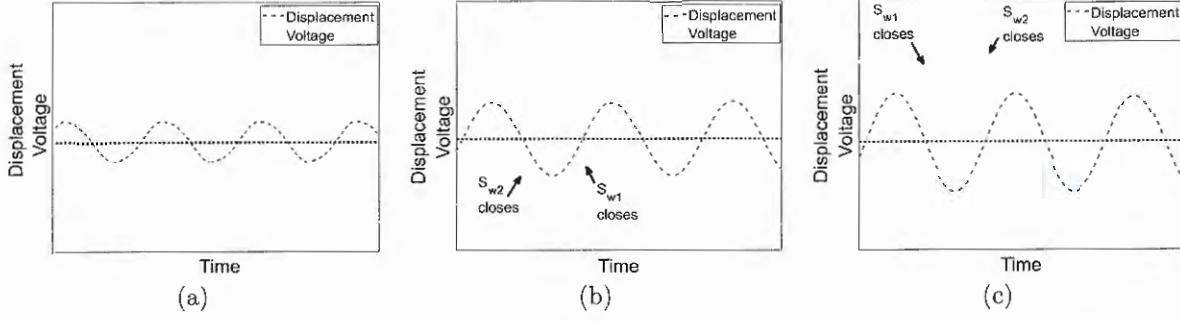


Figure 7 – Typical waveforms for (a) SSDVa, (b) SSSC-H (hardening) and (c) SSSC-S (softening) cases.

2009a; Hongli Ji et al., 2009; JI et al., 2010; MOKRANI et al., 2012), but the focus is not only restricted to vibration reduction due to damping enhancement. The so-called Synchronized Switching Stiffness Control technique, for instance, is employed to modify the structural equivalent stiffness of the electromechanical system (LALLART; GUYOMAR, 2010). In this sense, even though it considers the same working principle of the SSD techniques, the stiffness control method performs the switch operation when the structural displacement is zero, i.e. at maximum and minimum velocities. The stiffness variation results, then, from the phase adjustment between the voltage output of the piezoelectric element ( $V_p$ ) and the structural displacement of the system ( $u$ ). If both signals are in phase (figure 7b), there is an increase in the equivalent stiffness (hardening effect). However, if there is  $180^\circ$  phase shift (figure 7c), the equivalent stiffness is reduced (softening effect). In this case, the additional voltage is written as:

$$V_s = \beta \frac{\theta^t \mathbf{u}_{\max}}{C_p} \text{sign}(\mathbf{u}_{(t-\tau)}), \quad (2.5)$$

where  $\beta$  is a non-dimensional parameter and  $\mathbf{u}_{(t-\tau)}$  is the structural displacement at the  $\tau$  instant of time before the structural displacement reaches zero.  $\tau$  is required to determine if the displacement is increasing or decreasing before reaching zero and should be as small as possible to avoid delay issues in the switching operations. The equivalent stiffness  $\bar{\mathbf{K}}_{eq}$  and the new resonant frequency ( $\omega_{eq}$ ) of the system are described by (LALLART; GUYOMAR, 2010)

$$\bar{\mathbf{K}}_{eq} = \bar{\mathbf{K}} + \frac{\bar{\theta}^t \bar{\theta}}{C_p} \left( 1 \pm \frac{4}{\pi} \frac{1 + \gamma}{1 - \gamma} \beta \right), \quad (2.6)$$

$$\omega_{eq} = \sqrt{\frac{\bar{\mathbf{K}} + \frac{\theta^t \theta}{C_p} \left( 1 \pm \frac{4}{\pi} \frac{1 + \gamma}{1 - \gamma} \beta \right)}{\bar{\mathbf{M}}}}, \quad (2.7)$$

where the signal  $\pm$  is positive when the controller acts to provide a hardening effect and negative in case the softening effect is aimed, indicating that there is indeed an

increase and reduction, respectively, in the equivalent stiffness of the system. The stiffness control technique achieved with SSSC controller might be compared to mechanical systems developed with the same purpose such as the Smart Spring device, which is briefly described in the next section.

### 2.3 Smart materials and devices for vibration control in helicopters

Based on the considerations discussed in chapter 1, one may notice that the development of vibration control systems for helicopter has received great attention over the last decades. Passive controllers that are currently employed in commercial helicopters are typical mechanical vibration absorbers (spring-mass system), which have good control performance only in specific flight conditions and, therefore, are very restrict in terms of applications. The active controllers, on the other hand, usually located on the fuselage or rotor hub region, might adapt to different flight conditions and, thus, are able to mitigate undesired vibrations during most part of the helicopter's flight envelope. When they are in the fuselage, the control system function is specifically to reduce vibrations in the cabin, therefore, increasing the comfort during flight (HANAGUD; BABU, 1994). Nevertheless, in that case, the source of those vibrations is the interaction of main rotor blades and surrounding fluid. For this reason the literature has also reported vibration control either in the rotor hub or blades in order to be more effective, since it addresses the problem at its origin.

The vibration control systems strictly related to the rotating frame of helicopters can be separated in two groups within the Individual Blade Control (IBC) class: the On Blade Control (OBC) devices, which include the ACF, ATR and ACT; and the enhanced pitch link devices. The Actively Controlled Flap (ACF) system uses trailing edge flaps to reduce noise and vibration. The flaps can be activated by smart material based electromechanical systems that includes piezoelectric activated flaps (SPANGLER; HALL, 1986; BARRET, 1990; CHOPRA, 1992; FABUNMI, 1991; STREHLOW; RAPP, 1992), magnetostriction (FENN, 1992) or shape memory alloy systems (LIANG et al., 1996; STRAUB; EALEY; SCHETKY, 1997). The Active Twist Rotor (ATR) is a control system where smart materials are distributed blade-length wise in order to perform active vibration control by changing blade twist angle (CESNIK; SHIN, 2001; WALL et al., 2008), providing means to optimize the twist specifically for different flight condition such as hover or forward flight. In the case of Active Controlled Tip (ACT) systems the goal is to modify the blade geometry at the tip region to achieve noise and vibration reduction. And at last, the enhanced pitch links (also called, Active Pitch Links - APL), modify the blade root characteristics in order to reduce vibratory load transmitted from the blade to the fuselage.

Despite several studies have shown the feasibility of vibration reduction employing

each of the aforementioned techniques, it is important to mention that, individually, one of the four IBC systems could partially control noise and vibration caused by different phenomena (KLOEPEL; ENENKI, 2005). In fact, in some cases controlling a specific phenomenon could imply a deterioration of the other. In order to overcome this issue, Nitzsche et al. (2005) and later Feszty et al. (2008) proposed a hybrid vibration control system that consisted of using two or more independent IBC systems in the same blade. Through numerical simulations, the authors investigated the feasibility of combining flow (ACT and ACF) and structural (APL) control to modify the blade characteristics (figure 8). However, although a hybrid configuration was proposed, the researches focused on assessing the performance of each device individually, with a lot of effort concentrated on the development of an active pitch link.

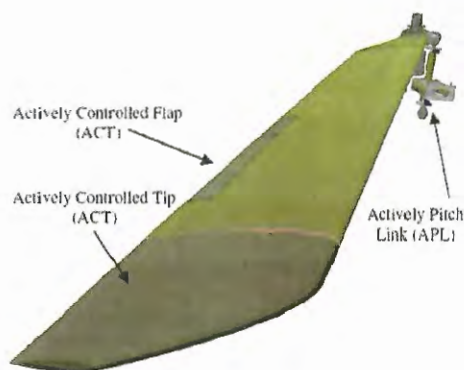


Figure 8 – Combination of ACT, ACF and APL controllers composing a hybrid vibration control device (FESZTY; NITZSCHE, 2011).

Originally, APL devices were developed to counteract the loading originated in the blade with the purpose of canceling the higher harmonic frequencies that would be transferred to the fixed frame of the helicopters. APL devices activated by hydraulic and magnetic actuators were successfully tested to reduce noise and vibration (JACKLIN et al., 1995b; JACKLIN et al., 1995a; LORBER et al., 2001; JACKLIN et al., 2002; ARNOLD; STRECKER, 2002; ELLISON, 2004). However, despite several successful flight campaigns have been carried out with hydraulic-based IBC actuators (TEVES; KLÖPPEL; RICHTER, 1992; SCHIMKE et al., 1997; MORBITZER; ARNOLD; MÜLLER, 1998; ROTH, 2004) the use of hydraulic systems has yet not shown appropriate characteristics to helicopter industry since they usually require heavy and bulky mechanisms to properly work. Moreover, these systems require pressurized fluid to work properly and a slip ring system for power supply and fluid transmission, which are also pointed out as drawbacks. The electrically actuated pitch links were investigated (FUERST; ARNOLD; GRAHAM, 2011; ARNOLD; FUERST, 2015) as alternative to this issue but designing and manufacturing electric APL is still a challenge since the power density of electric systems is usually much lower than that hydraulic systems can provide (WOODS et al., 2011).

The literature has also reported another approach for pitch-link-based IBC systems. Nitzsche and Breitbach (1992), Nitzsche, Lammering and Breitbach (1993), Anusonti-Inthra and Gandhi (2000), Anusonti-inthra and Gandhi (2001) showed that vibration control of APL devices could be understood as stiffness control at the blade root region and demonstrated, numerically and experimentally, that a periodic variation of the stiffness in that region could significantly reduce the vibration levels. The APL device reported by Nitzsche et al. (2005), Feszty et al. (2008), Nitzsche et al. (2013) is based on the Smart Spring concept (NITZSCHE et al., 2005) and it does not directly counter-act the aerodynamic loads but changes the effective spring constant of the device (or, more precisely, its impedance). It is the change of the blade's flex-torsional characteristics (i.e., its boundary conditions) that allows to control the aeroelastic response of the system.

The smart spring basically comprehends a mechanism (figure 9a) that associates springs using a piezoelectric actuator according to a specific control law (CREDE; CAVANAUGH, 1958) that determines the instants the springs should be engaged or disengaged. It consists of two mass-spring-damper systems<sup>2</sup> arranged in parallel. The system denoted with subscript 1 is called the main load path whereas the system denoted with subscript 2 is called the auxiliary load path. The auxiliary load path can be connected/disconnected by the action of a piezoelectric stack actuator, which contracts or expands in case a voltage level is applied to its terminals. This action results in contact between the piezoelectric actuator and the fixed mechanical sleeve, generating friction force and ultimately engagement to the sleeve (consequently, the main and secondary load paths are connected). In practice, the springs are aligned along the rotor shaft whereas the piezoelectric actuator (a piezo-stack, in this case) is oriented 90° relative to the shaft direction. Therefore, the piezoelectric actuator does not add energy to the system since it does not perform work. Moreover, the APL mechanism does not rely on actuators to achieve high stroke and force simultaneously. An issue with that approach is that it relies on both friction and external power (approximately 150V) to perform the control action. Figure 9 shows the evolution of the APL prototypes developed by Carleton University Rotorcraft Research Group.

In a similar fashion, Sirohi and Chopra (2003), John, Wereley and Sirohi (2009) employed a piezo-stack to drive a pump in order to pressurize an hydraulic fluid that was then utilized to transmit power to an output hydraulic cylinder. The device was designated by piezohydraulic pitch link and it is shown in figure 10a. According to Sirohi and Chopra (2003), the result was a localized, self-contained actuation system that combined the advantages of the power transmission flexibility of hydraulics and the high energy density of piezoelectric stacks. Despite the simpler design of this approach compared to regular servo-hydraulic systems, the piezohydraulic device still relies on external power source and fluid pressurization (although no hydraulic slip ring is required).

<sup>2</sup> Here, these two mass-spring-damper systems are designated as load paths in reference to the path which the load is transmitted during the smart spring operating process.

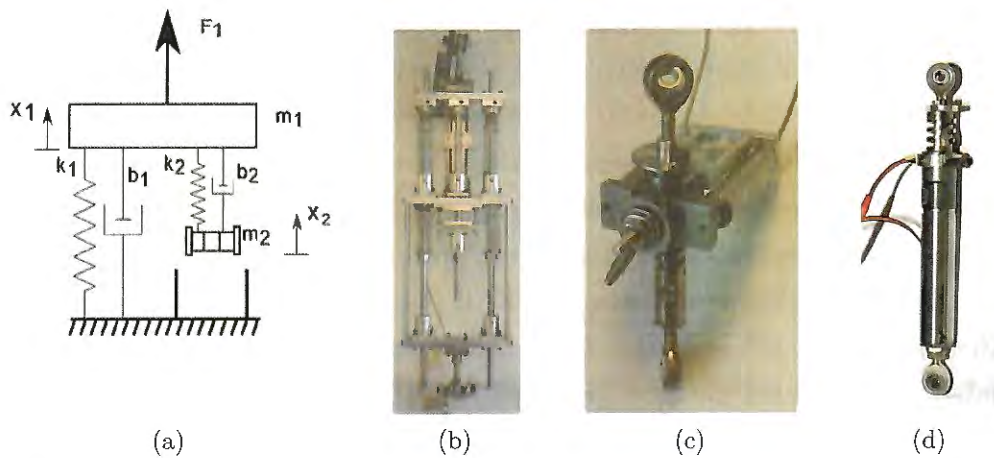


Figure 9 – (a) The schematics of the Smart Spring mechanism and the evolution of the APL prototypes: (b) first generation, 2003; (c) second generation, 2006; and (d) third generation, 2010 (NITZSCHE; D’ASSUNCAO; De Marqui Jr., 2015)

The fluidic pitch link (figure 10b) is another concept that was proposed by Han, Rahn and Smith (2014) in order to reduce higher harmonic loads using fluidlastic isolators. Such device relies on the effect of fluid flowing through smaller pipes (fluid track) to accelerate the fluid and absorb more energy, whereas the geometry of the fluid track dictates the frequency that should be isolated. Scarborough III et al. (2014b) numerically examined impedance tailoring fluidic pitch links for reduction of hub loads in high speed flight conditions and the simulation results demonstrated the ability of the device to influence all six hub forces and moments. However, these fluidic pitch links can only target a single higher harmonic. Thus, Scarborough III et al. (2014a) proposed connecting fluidic pitch links in order to target simultaneous higher harmonic loads (figure 10c).

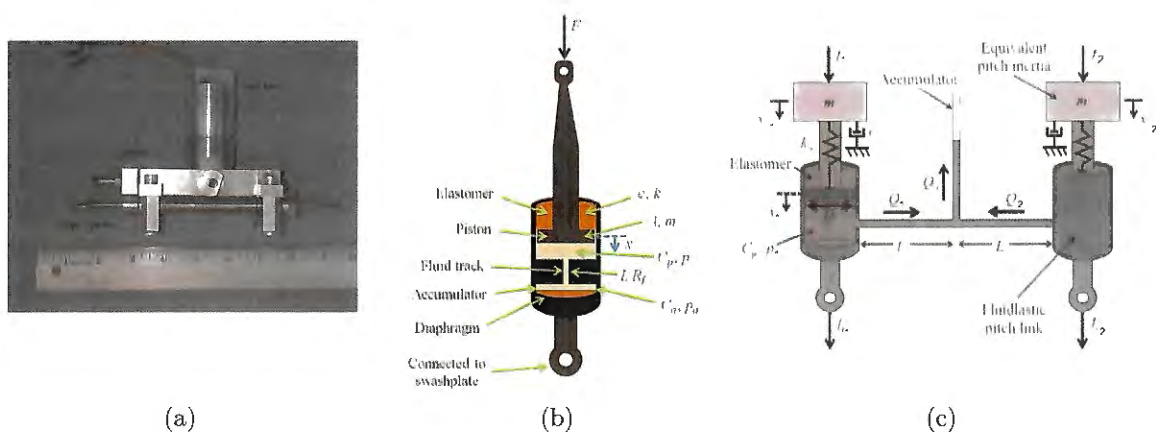


Figure 10 – (a) The prototype of a piezohydraulic pitch link proposed by John, Wereley and Sirohi (2009), (b) the schematics of a fluidic pitch link (Scarborough III et al., 2014b) and (c) coupled fluidic pitch links (Scarborough III et al., 2014a).

## 2.4 Final remarks

This section presented a literature review focusing on piezoelectric-based vibration control techniques as well as the development of enhanced pitch links for helicopter vibration reduction. As it could be noticed along this chapter, such techniques have been largely exploited with modeling and experimental approaches and the results reported in the literature have been demonstrating their great potential to reduce vibrations. Furthermore, there have been several applications that use piezoelectric materials for vibration reduction in helicopters, but so far no evidence was found, in the literature, of piezoelectric-based pitch links that enable both vibration control and energy harvesting capabilities on the same device such as the one that is presented in this dissertation.





### 3 NUMERICAL MODEL OF AN ELECTROMECHANICALLY COUPLED STRUCTURE

This chapter introduces the modeling of electromechanical systems that are composed of both an electromechanically coupled structure and a electric/electronic circuit. Such modeling strategy allows to represent piezoelectric devices developed for vibration control and/or energy harvesting purposes, likewise the new pitch link device proposed in this dissertation. Here, the electromechanical structure is represented using the Finite Element Method (FEM) while the electronic circuit, as well as the connection structure-circuit, is implemented using the Matlab-Simulink computational environment.

The modeling of dynamic systems, including those with electromechanical characteristics, might be given from different methods. The literature presents techniques that ranges from lumped parameter single degree of freedom (SDOF) models (ROUNDY; WRIGHT; RABAEY, 2003) to distributed parameter models with analytical solution (CHEN; WANG; CHIEN, 2006; ERTURK et al., 2009), Rayleigh-Ritz (SODANO; INMAN; PARK, 2004) and Finite Element approximations (De Marqui Jr.; ERTURK; INMAN, 2009). Among others, the FEM approach is implemented in a diversity of dedicated commercial software and open-source codes that allow practical and accurate modeling of complex systems. However, there are specific cases where this class of software has limited capability to attend the issues related to the interaction between mechanical and electrical domains. In general, such platforms allow to represent the connection of electromechanical structures to linear electrical circuits like resistors, capacitors and inductors. Hence, it is possible to model simple passive and active controllers and not more complex circuits that include more complex electric (or electronic) elements such as transistors, MOSFETs and operational amplifiers, for example.

In order to overcome such limitations, researchers have developed the models of each domain independently, at first, and account for their interaction afterwards. In this sense, two approaches are usually employed to model electromechanical structures connected to electric/electronic circuits:

- (a) Represent the electromechanical structure using the equivalent circuit modeling approach and perform simulations using software dedicated to model electric circuits such as Spice and Multisim (YANG; TANG, 2009; ELVIN; ELVIN, 2008);
- (b) Represent the electromechanical structure using the equation of motion and perform simulations with the Matlab-Simulink interface, where the model of the electromechanical structure would be connected to electric circuit models implemented in a single simulation environment (WU; GUYOMAR; RICHARD, 2013).

In this project, the Finite Element Method is employed as modeling tool to develop and design the piezoelectric structure of the new smart device proposed. Figure 11 shows the schematics of a cantilevered piezoelectric plate, where  $L_s$  and  $t_s$  are the length and thickness of the substructure, respectively;  $L_p$  and  $t_p$  are, the length and thickness of the piezoelement, respectively;  $L_x$  is the distance<sup>1</sup> between the fixed end (i.e., encastre) and the piezoelectric element; and the subscript 1 and 2 refer to the upper and lower piezoelements, respectively.

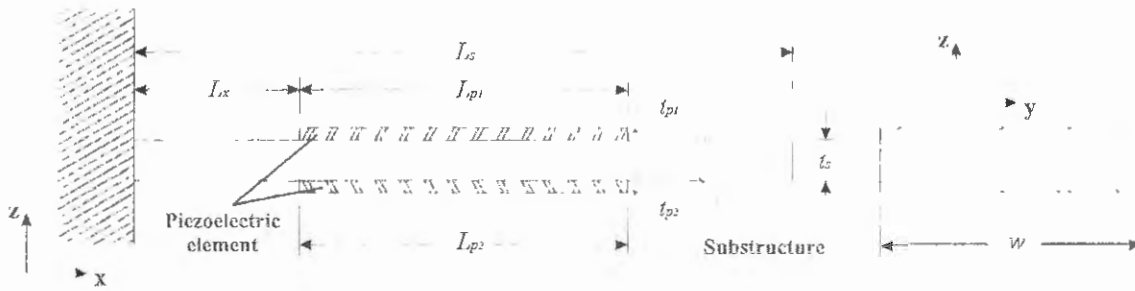


Figure 11 – Schematics of a generic piezoelectric plate structure.

It is important to mention, however, that the Finite Element Method is used in this project as an effective tool to design the structure hereafter proposed. Thus, since the formulation of this method for piezoelectric problems is very solid and well documented in the literature, the remainder of this section describes, briefly, the premises of FEM and the assumptions presumed to develop the model.

### 3.1 General considerations on modeling of a piezoelectric structure

The equation of motion for electromechanical systems can be derived from the Generalized Hamilton's Principle (GHP) (TIERSTEN, 1969; ALLIK; HUGHES, 1970), which can be defined as

$$\int_{t_1}^{t_2} [\delta (T_c - U + W_e) + \delta W] = 0, \quad (3.1)$$

where  $t_1$  and  $t_2$  are two arbitrary instants,  $T_c$  is the total kinetic energy,  $U$  is the total potential energy,  $W_e$  is the electrical work and  $\delta W$  is the variation of the virtual work due

<sup>1</sup> Generally, this value is zero because the fixed region of the cantilevered structure provides better energy conversion since it is the region with the highest strain levels.

to external  $F_e$ , surface  $F_s$  and body  $F_c$  forces. These variables are defined as follows:

$$T_c = \frac{1}{2} \int_{V_s} \rho_s \dot{\mathbf{u}}^T \dot{\mathbf{u}} dV_s + \frac{1}{2} \int_{V_p} \rho_p \dot{\mathbf{u}}^T \dot{\mathbf{u}} dV_p, \quad (3.2)$$

$$U = \frac{1}{2} \int_{V_s} \mathbf{S}^T \mathbf{T} dV_s + \frac{1}{2} \int_{V_p} \mathbf{S}^T \mathbf{T} dV_p, \quad (3.3)$$

$$W_e = \frac{1}{2} \int_{V_p} \mathbf{E}^T \mathbf{D} dV_p, \quad (3.4)$$

$$\delta W = \int_{V_s} \delta \mathbf{u}^T \mathbf{F}_e dV + \int_{A_s} \delta \mathbf{u}^T \mathbf{F}_s dA_s + \delta \mathbf{u}^T \mathbf{F}_c + \int_{A_p} \delta \mathbf{v}^T \mathbf{q} dA_p, \quad (3.5)$$

and  $\mathbf{T}$  is the stress tensor [N/m<sup>2</sup>],  $\mathbf{S}$  is the strain tensor [m/m],  $\mathbf{q}$  is the electric charge vector [C],  $\mathbf{v}$  is the electric potential vector [V],  $V$  represents volume [m<sup>3</sup>],  $A$  represents area [m<sup>2</sup>],  $\mathbf{u}$  is the displacement vector [m],  $\dot{\mathbf{u}}$  is the velocity vector [m/s],  $\rho$  is the mass density [kg/m<sup>3</sup>] and the subscripts  $p$  and  $s$  relates to the piezoelectric material and the substructure, respectively. In equation 3.5, the last term is written with positive signal since the load extracts energy from the system.

Since the electromechanical system includes piezoelectric elements, equations (3.3) and (3.4) must account for the constitutive properties of piezoelectricity. Assuming the model will only experience linear behaviour, these properties may be represented for the direct and inverse effect, in the three-dimensional form, as follows (IEEE, 1987):

$$\begin{pmatrix} T_{11} \\ T_{22} \\ T_{33} \\ 2T_{23} \\ 2T_{31} \\ 2T_{12} \\ D_1 \\ D_2 \\ D_3 \end{pmatrix} = \begin{bmatrix} c_{11}^E & c_{12}^E & c_{13}^E & 0 & 0 & 0 & 0 & 0 & -e_{31} \\ c_{12}^E & c_{11}^E & c_{13}^E & 0 & 0 & 0 & 0 & 0 & -e_{31} \\ c_{13}^E & c_{13}^E & c_{33}^E & 0 & 0 & 0 & 0 & 0 & -e_{33} \\ 0 & 0 & 0 & c_{44}^E & 0 & 0 & 0 & 0 & 0 \\ 0 & 0 & 0 & 0 & c_{55}^E & 0 & 0 & -e_{15} & 0 \\ 0 & 0 & 0 & 0 & 0 & c_{66}^E & -e_{15} & 0 & 0 \\ 0 & 0 & 0 & 0 & 0 & e_{15} & \varepsilon_{11}^S & 0 & 0 \\ 0 & 0 & 0 & 0 & e_{15} & 0 & 0 & \varepsilon_{11}^S & 0 \\ e_{31} & e_{31} & e_{33} & 0 & 0 & 0 & 0 & 0 & \varepsilon_{33}^S \end{bmatrix} \begin{pmatrix} S_{11} \\ S_{22} \\ S_{33} \\ S_{23} \\ S_{31} \\ S_{12} \\ E_1 \\ E_2 \\ E_3 \end{pmatrix}, \quad (3.6)$$

where  $D$  is the electric displacement [C/m<sup>2</sup>],  $E$  is the electric field [N/C], the subscript  $(\ )_{ij}$  relates to the polling direction ( $i$ ) of the piezoelectric material and the direction of the external force or electric field applied ( $j$ ), while the superscripts  $E$  and  $S$  represent constant electric field and constant strain, respectively. In addition, one should note that the symmetry conditions applied to equation (3.6) affects the elastic  $c$ , dielectric  $\varepsilon$  and piezoelectric stress  $e$  constants ( $c_{11}^E = c_{22}^E$ ,  $e_{31} = e_{32}$ ,  $\varepsilon_{11}^S = \varepsilon_{22}^S$ , etc.) due to the plane-stress assumption for a transversely isotropic thin piezoelectric beam (ERTURK; INMAN, 2011).

Hence, substituting the linear constitutive properties of the piezoelectric effect into the GHP expression (equation 3.1) gives

$$\int_{t_1}^{t_2} \left[ \begin{aligned} & \int_{V_s} \rho_s \delta \dot{\mathbf{u}}^T \dot{\mathbf{u}} dV_s + \int_{V_p} \rho_p \delta \dot{\mathbf{u}}^T \dot{\mathbf{u}} dV_p - \int_{V_s} \delta \mathbf{S}^T \mathbf{c}_s \mathbf{S} dV_s - \int_{V_p} \delta \mathbf{S}^T \mathbf{c}_p^E \mathbf{S} dV_p + \\ & \int_{V_p} \delta \mathbf{S}^T \mathbf{e}^T \mathbf{E} dV_p + \int_{V_p} \delta \mathbf{E}^T \boldsymbol{\varepsilon}^s \mathbf{E} dV_p + \int_{V_s} \delta \mathbf{E}^T \mathbf{e} \mathbf{S} dV_p + \int_{V_s} \delta \mathbf{u}^T \mathbf{F}_e dV_s + \\ & \int_{A_s} \delta \mathbf{u}^T \mathbf{F}_s dA_s + \delta \mathbf{u}^T \mathbf{F}_c + \int_{A_p} \delta \mathbf{v}^T \mathbf{q} dA_p \end{aligned} \right] dt = 0, \quad (3.7)$$

whose solution results in a (partial differential) equation of motion for any mechanical system that incorporates piezoelectric elements. Here, the Finite Element Method (FEM) is employed to approximate this solution.

In general, the FEM essentially approximates the region of analysis by a finite number of smaller regions, known as *finite elements* (FE), where are defined the unknown variables of interest that depends on the nature of the problem to solve (a piezoelectric structure involves displacement and voltage, for example). The intersection point of such regions, designated by the term *node*, provides the connectivity between neighboring finite elements. Thus, through the nodal variables it is possible to find a local solution for each FE, since the boundary conditions are less complex if compared to the global domain investigated. The unknown nodal variables are expressed in terms of shape functions in order to map their behavior in any coordinate of the FE, such that a global solution may be approximated for the problem.

According to Bhatti (2005), applying the FEM to an specific problem involves the following steps:

- A. Derive the element's equation;
- B. Perform the discretization of the domain into a mesh of finite elements;
- C. Assemble the element's equation for the whole domain;
- D. Introduce the boundary conditions (geometrical restrictions);
- E. Solve the equations for the unknown variables;
- F. Calculate the solution and related quantities over each element.

Therefore, by applying the FE approach to equation (3.7) the governing equations of the system are

$$\mathbf{M}_u \ddot{\Psi} + \mathbf{C} \dot{\Psi} + \mathbf{K}_u \Psi - \mathbf{K}_{uv} \mathbf{v} = \mathbf{F}, \quad (3.8)$$

$$\mathbf{K}_{vv} \mathbf{v} + \mathbf{K}_{uv}^T \Psi = -\mathbf{Q}, \quad (3.9)$$

where  $\mathbf{M}_u$  is the global mass matrix,  $\mathbf{K}_u$  is the global stiffness matrix,  $\mathbf{K}_{uv}$  is the global electromechanical coupling matrix,  $\mathbf{K}_{vv}$  is the global capacitance matrix,  $\Psi$  is the vector of global mechanical coordinates,  $\mathbf{v}$  is the global electric potential vector,  $\mathbf{Q}$  is the global electrical charge vector and  $\mathbf{F}$  is the vector that comprehends the external forces applied to the structure. The damping<sup>2</sup> of the electromechanical structure is assumed to be proportional to the mass and stiffness,

$$\mathbf{C} = \alpha\mathbf{M}_u + \beta\mathbf{K}_u, \quad (3.10)$$

where  $\alpha$  and  $\beta$  are the proportionality constants.

In order to account for the connection between both the electrical and structural models one must consider a few assumptions. First, according to the procedure presented by Guo, Cawley and Hitchings (1992), it is possible to separate the electric potential vector ( $\mathbf{v}$ ) in three different parts based on the geometry of the piezoelectric element:

- $\mathbf{v}^{(i)}$  - represents the electric potential of the inner nodes and all other nodes that are not located in the electrodes of the piezoelement;
- $\mathbf{v}^{(P)}$  - represents the electric potential of the upper electrode (or positive electrode);
- $\mathbf{v}^{(G)}$  - represents the electric potential of the electrode in contact to the substructure (also known as reference electrode);

Consequently, the force  $\mathbf{F}$  and electric charge  $\mathbf{Q}$  vector, as well as, the electromechanical coupling  $\mathbf{K}_{uv}$  and capacitance  $\mathbf{K}_{vv}$  matrices can be separated in subvectors and submatrices, respectively.

In this sense, splitting the piezoelement in different regions allows to mathematically manipulate the electric potential of the reference electrode to zero, simulating the case where the electrode is "grounded". Therefore, in the equation of motion, one may separate the electric degrees of freedom related to the grounded surface from the remainder DOFs. Besides, acknowledging the electric charge is null for nodes that are not located on the electrodes, i.e.  $\mathbf{Q}^{(i)} = 0$ , equations (3.8) and (3.9) may be rewritten as follows (KOCBACH; LUNDE; VESTRHEIM, 1999):

$$\begin{bmatrix} \mathbf{M}_u & \mathbf{0} \\ \mathbf{0} & \mathbf{0} \end{bmatrix} \begin{Bmatrix} \ddot{\Psi} \\ \ddot{\mathbf{v}}^{(P)} \end{Bmatrix} + \begin{bmatrix} \mathbf{H}_u & \mathbf{H}_{uvP} \\ \mathbf{H}_{uvP}^T & \mathbf{H}_{vPvP} \end{bmatrix} \begin{Bmatrix} \Psi \\ \mathbf{v}^{(P)} \end{Bmatrix} = \begin{Bmatrix} \mathbf{F} \\ -\mathbf{Q}^{(P)} \end{Bmatrix}, \quad (3.11)$$

$$\mathbf{H}_u = \mathbf{K}_u + \mathbf{K}_{uv_i} \mathbf{K}_{v_i v_i}^{-1} \mathbf{K}_{uv_i}^T, \quad (3.12)$$

$$\mathbf{H}_{uvP} = \mathbf{K}_{uvP} + \mathbf{K}_{uv_i} \mathbf{K}_{v_i v_i}^{-1} \mathbf{K}_{v_i vP}, \quad (3.13)$$

$$\mathbf{H}_{vPvP} = \mathbf{K}_{vPvP} - \mathbf{K}_{v_i vP}^T \mathbf{K}_{v_i v_i}^{-1} \mathbf{K}_{v_i vP}. \quad (3.14)$$

<sup>2</sup> This term is omitted hereafter in order to simplify the mathematical notation and will be included again at the end of this section.



It is worthwhile to mention that equation (3.11) employs a condensed matrix notation only to ease the viewing and understanding of the assumptions made, in a way that the previous notation used in equations (3.8) and (3.9) is again employed for the next sessions in the remainder of this chapter. In addition, this transformation was performed in order to consider the influence of the inner nodal variables over the electrodes variables, since the electric potential difference (i.e., voltage) is measured across the electrodes.

Another assumption made during the modeling procedure involves the discretization of the domain. According to the premises of the FEM, in order to represent the electromechanical structure one must divide the piezoelectric material in several elements assuming it is composed of several electrodes and, consequently, several DOFs. Nevertheless, in practice the piezoelectric layers have conductive continuous electrodes. Therefore, only one degree of freedom should be used in order to represent the electric response of the piezoelement, being appropriate to assume that all finite elements of the electrode's surface generate the same voltage output  $v$  (GUO; CAWLEY; HITCHINGS, 1992; De Marqui Jr.; ERTURK; INMAN, 2009):

$$\mathbf{v} = \left\{ v_1 \quad v_2 \quad \cdots \quad v_{n_e} \right\}^T = \left\{ 1 \quad 1 \quad \cdots \quad 1 \right\}^T v_p = \mathbf{I}_p^T v_p, \quad (3.15)$$

where  $n_e$  is the total number of electric DOFs in the electrodes. This transformation is extended to the electromechanical coupling matrix,  $\mathbf{H}_{uv} = \mathbf{I}_p^T \mathbf{H}_{uv_p}$  (which turns into a vector), and capacitance matrix,  $H_{vv} = \mathbf{I}_p^T \mathbf{H}_{v_p v_p} \mathbf{I}_p$  (which turns into a scalar). Besides, regarding the interaction between the electromechanical structure and the electric circuits, one can express equations (3.8) and (3.9) as

$$\mathbf{M}_u \ddot{\Psi} + \mathbf{C} \dot{\Psi} + \mathbf{H}_u \Psi - \mathbf{H}_{uv} v = \mathbf{F}, \quad (3.16)$$

$$H_{vv} \dot{v} + \mathbf{H}_{uv}^T \dot{\Psi} = -\dot{Q}. \quad (3.17)$$

Thus, by differentiating equation (3.9), which describes the inverse piezoelectric effect of the electromechanical system, one can notice the term  $\dot{Q}$  that appears in equation (3.17), representing the electric current that flows in the circuit and, consequently, feeds back the piezoelement. This simple manipulation allows to implement the equation of motion including the effect of connecting the electromechanical structure to the circuit<sup>3</sup>. This approach is presented in the next section.

Finally, it is well known from the literature of dynamic systems that distributed parameter models might involve an extensive number of DOFs depending on the problem analyzed and due to this fact, manipulating the variables that represent those degrees of freedom may be hindered. Therefore, modal domain representation and state space realization (both hereafter employed) are considered to be convenient techniques employed

<sup>3</sup> The term piezoelectric circuit might be used hereafter

to assure the system is represented in a more practical fashion. Hence, from the eigenvalue problem ( $[H_{uu} - \omega^2 M_{uu} \Phi] = 0$ ) it is possible to obtain the eigenvalues and eigenvectors<sup>4</sup> of the system and, thus, rewrite the equations of motion as

$$\bar{\mathbf{M}}_u \ddot{\boldsymbol{\eta}} + \bar{\mathbf{C}} \dot{\boldsymbol{\eta}} + \bar{\mathbf{H}}_u \boldsymbol{\eta} - \bar{\mathbf{H}}_{uv} v = \bar{\mathbf{F}}, \quad (3.18)$$

$$H_{vv} \dot{v} + \bar{\mathbf{H}}_{uv}^T \dot{\boldsymbol{\eta}} = -\dot{Q}, \quad (3.19)$$

$$\bar{\mathbf{M}}_u = \Phi^T \mathbf{M}_u \Phi, \quad \bar{\mathbf{H}}_u = \Phi^T \mathbf{H}_u \Phi, \quad \bar{\mathbf{H}}_{uv} = \Phi^T \mathbf{H}_{uv}, \quad \bar{\mathbf{F}} = \Phi^T \mathbf{F}, \quad (3.20)$$

where  $\boldsymbol{\eta}$  is the vector of modal coordinates,  $\Phi$  is the mode shape matrix,  $\bar{\mathbf{M}}_u$  is the modal mass matrix,  $\bar{\mathbf{C}}$  is the modal damping matrix,  $\bar{\mathbf{H}}_u$  is the modal stiffness matrix and  $\bar{\mathbf{F}}$  is the vector of external forces in modal domain. In equations 3.18 and 3.19,  $\Phi$  is a  $N \times n$  matrix with  $N$  being the total number of DOFs (boundary conditions included) and  $n$  is the number of modes considered during the analysis. In other words, the modal matrices are truncated in a way that the analysis (or simulation) contemplates only the more relevant modes. According to Bathe (1982) and Kocbach, Lunde and Vestrheim (1999), in order to accurately approximate the exact solution one must include in the analysis, mode shapes that correspond to frequencies that are at least 50% greater than the highest frequency analyzed.

### 3.2 Description of the modeling procedure

The Finite Element Method was employed using the software ABAQUS<sup>TM</sup> version 6.10 (ABAQUS, 2010) as modeling tool to represent an electromechanical structure composed of piezoelectric elements attached to a metallic substructure. In this sense, in order to follow the approach presented in section 3.1 one must obtain the matrices that describe the electromechanical structure ( $\mathbf{M}_u$ ,  $\mathbf{K}_u$ ,  $\mathbf{K}_{uv}$  and  $\mathbf{K}_{vv}$ ).

In this work, the management of the matrices provided by the FE modeling tool was carried out using a code developed by the author using the software MATLAB. The code reads a file extracted from ABAQUS (which contains the FE matrices in vectorial form), assembles the global matrices that represent the electromechanical system and separates them according the approach previously described. In addition, a sub-routine was developed using Python programming language with the purpose of automatizing the modeling procedure carried out with the FE software. Thus, once a base configuration was set for the structure, a parametric assessment (involving geometric parameters and structural properties, for instance) could be easily performed in order to optimize the electromechanical structure specifically for each application. The Python code is also executed using the software MATLAB.

<sup>4</sup> When mass normalized, such variables provide means of obtaining the natural frequencies and mode shapes of the system.



Furthermore, it is important to highlight at this point that the extraction of the FE matrices from software ABAQUS must occur prior the application of the boundary conditions, as suggested by the software's documentation (ABAQUS, 2010), since altering the matrices to account for such conditions might increase their order, make them more dense and, consequently, require more computational processing. Therefore, the boundary conditions are applied after the extraction of the matrices by truncating the rows and columns referred to the degrees of freedom that must be restrained. This procedure is employed for both the mechanical and electrical boundary conditions.

After the electromechanical modeling procedure has been concluded, one should account for the connection between the structure and the piezoelectric circuit models. According to Rupp, Dunn and Maute (2010), such connection can be performed assuming a continuity condition between the electric current and voltage of both systems, which requires, therefore, incorporating, into the model, the effect of the electrical feedback current flowing from the circuit to piezoelectric element as follows:

$$v_{circuit} = v_{Piezo}, \quad (3.21)$$

$$i_{circuit} = i_{Piezo}. \quad (3.22)$$

In addition, because of the multiphysics characteristic of the problem, it is frequently of concern to use software packages that allow to model the interaction between the electromechanical system and circuit using one computational environment only. Hence, assuming, for example, a case where two piezoelectric elements are attached to a metallic thin beam, each one connected to a different rectifier circuit (figure 12), it is possible to rewrite the electromechanical equations of motion using a state-space realization

$$\dot{\mathbf{x}} = \mathbf{A}\mathbf{x} + \mathbf{B}_1\mathbf{u}_1 + \mathbf{B}_2\mathbf{u}_2 + \mathbf{B}_3\mathbf{u}_3, \quad (3.23)$$

$$\mathbf{y} = \mathbf{C}_o\mathbf{x} + \mathbf{D}_1\mathbf{u}_1 + \mathbf{D}_2\mathbf{u}_2 + \mathbf{D}_3\mathbf{u}_3, \quad (3.24)$$

where the state vector is  $\mathbf{x} = \{\boldsymbol{\eta}(t) \ \dot{\boldsymbol{\eta}}(t) \ v_1(t) \ v_2(t)\}^T$  and the mechanical variable are expressed in the modal domain. The state matrix  $\mathbf{A}$ , the input matrix  $\mathbf{B}$ , the output matrix  $\mathbf{C}_o$  are defined as:

$$\mathbf{A} = \begin{bmatrix} \mathbf{0}_{n \times n} & \mathbf{I}_{n \times n} & \mathbf{0}_{n \times 1} & \mathbf{0}_{n \times 1} \\ -\mathbf{M}_u^{-1}\mathbf{H}_u & -\mathbf{M}_u^{-1}\mathbf{C} & \mathbf{M}_u^{-1}(\mathbf{H}_{uv})_1 & \mathbf{M}_u^{-1}(\mathbf{H}_{uv})_2 \\ \mathbf{0}_{1 \times n} & -\left(H_{vv}^{-1}\mathbf{H}_{uv}^T\right)_1 & 0 & 0 \\ \mathbf{0}_{1 \times n} & -\left(H_{vv}^{-1}\mathbf{H}_{uv}^T\right)_2 & 0 & 0 \end{bmatrix} \quad (3.25)$$

$$\mathbf{B} = [\mathbf{B}_1 \ \mathbf{B}_2 \ \mathbf{B}_3] = \begin{bmatrix} \mathbf{0}_{n \times 1} & \mathbf{0}_{n \times 1} & \mathbf{0}_{n \times 1} \\ \mathbf{M}_u^{-1}\mathbf{F}_o & \mathbf{0}_{n \times 1} & \mathbf{0}_{n \times 1} \\ 0 & (H_{vv}^{-1})_1 & 0 \\ 0 & 0 & (H_{vv}^{-1})_2 \end{bmatrix} \quad \mathbf{C}_o = \begin{bmatrix} \mathbf{0}_{1 \times n} & \mathbf{0}_{1 \times n} & 1 & 0 \\ \mathbf{0}_{1 \times n} & \mathbf{0}_{1 \times n} & 0 & 1 \\ \boldsymbol{\Phi} & \mathbf{0}_{1 \times n} & 0 & 0 \\ \mathbf{0}_{1 \times n} & \boldsymbol{\Phi} & 0 & 0 \end{bmatrix},$$

and the direct transition matrix  $\mathbf{D}_o$  is the zero matrix (in this case). Here, the mode shape vector is  $\Phi = \{\Phi_1(x) \ \Phi_2(x) \ \dots \ \Phi_n(x)\}$ ,  $\mathbf{0}$  a zero matrix,  $\mathbf{I}$  is the identity matrix, and the subscripts  $( )_1$  and  $( )_2$  refers to piezoelements 1 and 2, respectively. Besides, the output matrix  $\mathbf{C}_o$  gives the mechanical and electrical response of the electromechanical system  $\mathbf{y} = \{v_1(t) \ v_2(t) \ \Psi(t) \ \dot{\Psi}(t)\}^t$ .

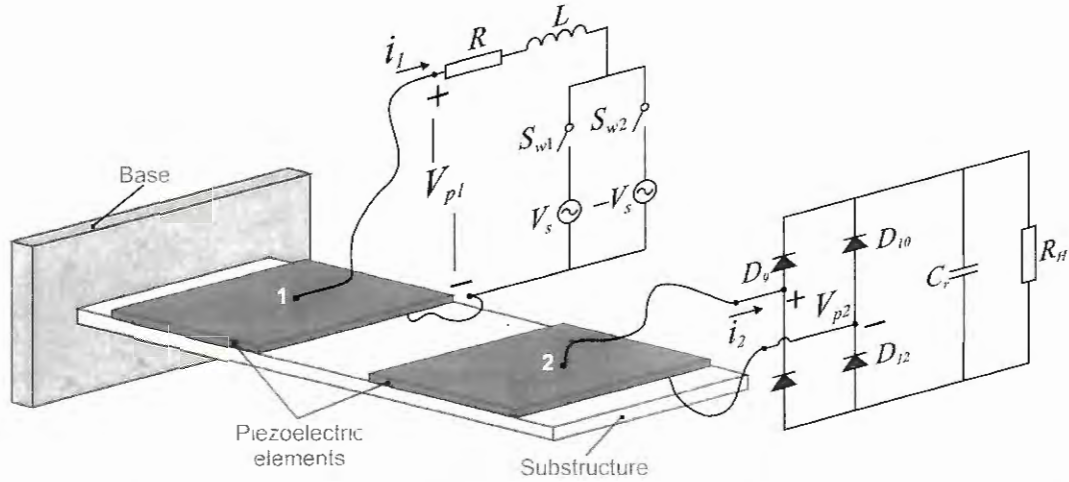


Figure 12 – Schematics illustrating the connection between the piezoelements and their respective circuits, a full-wave bridge rectifier and a switching circuit with voltage sources (SSDVA or SSSC, for example).

The input vectors are defined as  $\mathbf{u}_1 = \sin(\omega t)$ ,  $\mathbf{u}_2 = -\dot{\mathbf{q}}_1(t)$  and  $\mathbf{u}_3 = -\dot{\mathbf{q}}_2(t)$ , where  $\mathbf{u}_1$  must be multiplied by  $\mathbf{F}_o$  in order to represent the external applied force. The electric current signals  $\mathbf{i}_1(t) = \dot{\mathbf{q}}_1(t)$  and  $\mathbf{i}_2(t) = \dot{\mathbf{q}}_2(t)$  resulting from the circuits coupled to the electrodes of piezoelectric elements 1 and 2, respectively, are fed back to the piezoelements as shown in figure (12). In this sense, one shall observe that a case where  $k$  piezoelectric elements are added to the electromechanical system may result in two possible connections for the piezoelectric circuit: 1– perform a series or parallel connection of both piezoelements in order to increase the electric response (current or voltage, respectively); 2– connect each piezoelement, separately, to a distinct circuit. The second approach allows to simulate a case where one piezoelectric element would account for sending the control signal while the other could harvest vibratory energy from the system and, thus, supply the converted energy to the active elements of the controller circuit, for example. Besides, this approach also provides the possibility of designing self-powered controllers where the circuit's parameters and topology could be determined from numerical simulations performed using the MATLAB/Simulink interface together with the procedure described in this section. Therefore, in this work, the numerical simulation procedure is divided in four basic parts (figure 13):

1. To model the electromechanical system using the FEM and implement the equations of motion in MATLAB's environment;

2. To implement the piezoelectric circuit model in Simulink using the SimScape library;
3. To connect both implemented models into Simulink's environment;
4. To simulate the unified model for the desired cases and extract the results.

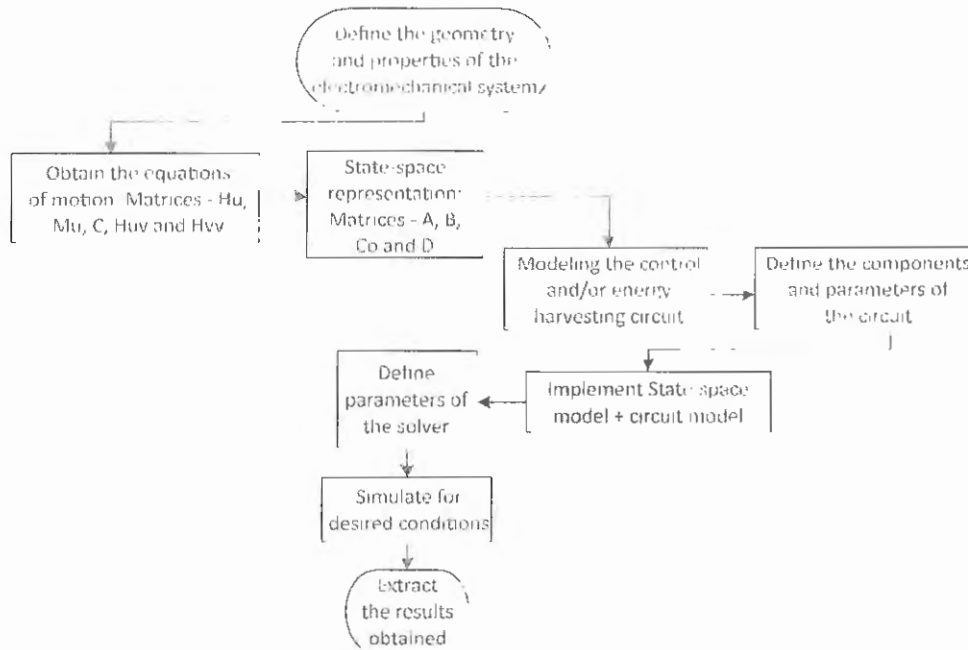


Figure 13 – Flow chart of the basic steps required to simulate a piezoelectric device coupled to electric/electronic circuits.

### 3.3 Verification of the modeling procedure

The presented modeling procedure proposes using the software ABAQUS and MATLAB/Simulink as effective tools to simulate both the electromechanical structure and electric/electronic circuits that comprehend a piezoelectric vibration control system. Hence, it is primarily essential to verify whether the approach provides consistent results or not. Therefore, at first, the results achieved with the proposed model were compared to results previously reported in the literature by De Marqu. Jr., Erturk and Inman (2009), where a cantilever bimorph beam (i.e, with both faces completely covered by piezoelectric materials, figure 14a) was modeled. The piezoelectric device comprehended two PZT elements attached to a 50.8 mm × 31.8 mm × 0.14 mm substructure (figure 14a), with a tip mass  $m_{tip} = 12 \times 10^{-3}$  kg added to the free end of the cantilever. De Marqui Jr., Erturk and Inman (2009) assessed the Frequency Response Functions (FRF) for both open and short circuit cases when the piezoelements were connect to a shunt resistor and verified their FE model against experimental and analytical results.

Concerning the approach here proposed, the electromechanical structure was modeled using three-dimensional solid elements with parabolic interpolation. All finite

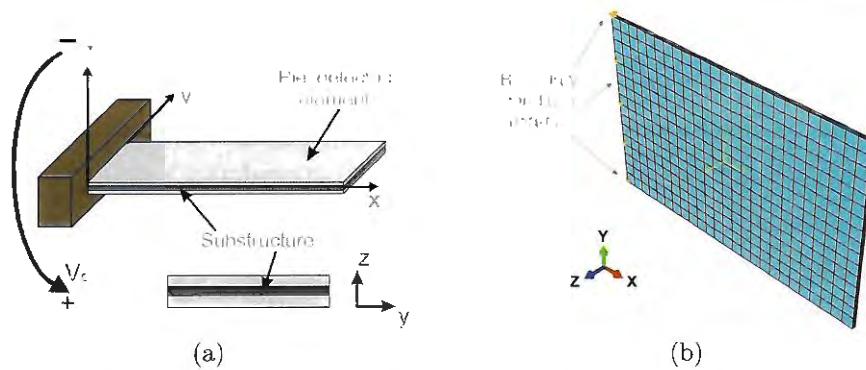


Figure 14 – (a) Schematics of a bimorph piezoelectric structure and (b) its respective model developed using ABAQUS software.

elements included 20 nodes and 3 DOFs, in each node, which represented displacement in three directions ( $x,y,z$ ) for both the structure and the piezoelectric material<sup>5</sup>. In addition, the finite elements used to model piezoelectric materials included an additional degree of freedom to account for the electric potential.

Figure (15) compares the FRFs of the electromechanical system for the model proposed in this work and the model presented in De Marqui Jr., Erturk and Inman (2009), Erturk and Inman (2009), indicating the results of both procedures match accordingly. Therefore, the proposed model provides a good approximation of simulations regarding such electromechanical systems.

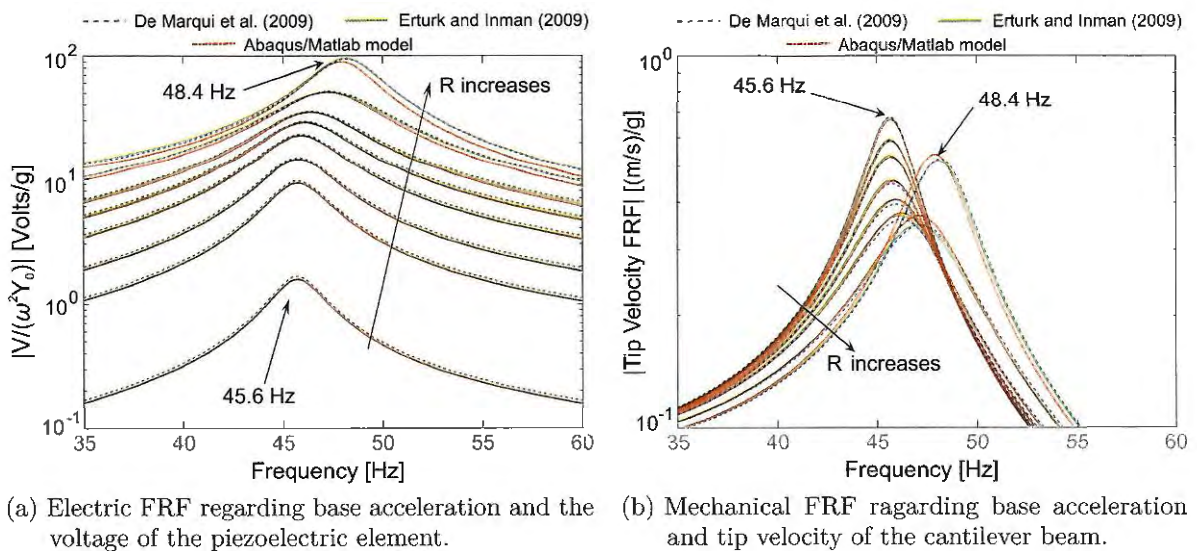


Figure 15 – Electromechanical FRFs comparing the results of De Marqui Jr., Erturk and Inman (2009), Erturk and Inman (2009) and the proposed modeling procedure.

<sup>5</sup> ABAQUS software designates the code C3D20 for purely structural finite elements and C3D20E for piezoelectric finite elements.

### **3.4 Final Remarks**

This chapter presented a modeling approach to represent an electromechanically coupled (piezoelectric) structure connected to electric circuits for vibration control and/or energy harvesting purpose. The modeling approach considered a finite element model to represent the structural domain and the electric/electronic circuit was modeled using the Matlab/Simulink platform, which also accounted for modeling the interaction of the complete electromechanical system. The proposed approach was successfully verified with numerical results reported in the literature for a cantilevered electromechanically coupled beam under base excitation. Nevertheless, further simulations of the new piezoelectric pitch link were not performed considering the combination of the electromechanical structure and the electric/electronic circuit due to issues occurred during the estimation of the damping matrix.

#### 4 THE NEW SMART PIEZOELECTRIC PITCH LINK (SaPPL)

The mechanic pitch link (APL) proposed by [Nitzsche and Feszty \(2008\)](#) has been shown a successful alternative to the active pitch links based on hydraulic and magnetic actuators. However, despite its fail safe concept (since the stiffness of a regular rigid pitch link is obtained in case the piezoelectric material fails), the APL is sensitive to (undesired) mechanical wear because its working principle depends on friction between different parts. In this sense, it would be interesting to avoid the drawbacks of a mechanical device by combining a piezoelectric-based pitch link to electric/electronic circuits for vibration reduction in helicopters.

The Smart Piezoelectric Pitch Link (SaPPL) proposed here may be understood as an electrical solid-state device that might be an alternative to increase energy dissipation (thus, increase damping) and/or change the effective stiffness of the pitch link and, consequently, attenuate vibration at a target frequency or bandwidth. The new system comprehends mainly two devices: an electromechanical structure with attached piezoelectric patches and an electric/electronic circuit. The structure would be capable of modifying the structural characteristics of the pitch link by properly managing the electrical output of the piezoelectric patches with the circuits, such as those used by the switching techniques ([CLARK, 2000](#); [GUYOMAR; RICHARD; MOHAMMADI, 2007a](#); [LALLART; GUYOMAR, 2010](#)). In addition, since the structure is equipped with several piezoelectric elements, part of them may be employed for energy harvesting (EH) purposes, therefore, producing energy in the rotating frame of the aircraft. Figure 16 depicts an schematics that represents the functionality of the device, which should basically reduce the vibration transmitted through its body as result of the proper operation of electric/electronic circuits. Besides, ideally the available energy produced by the #EH piezoelements could be used as power supply not only for the control circuit but also for other low power devices located at the rotating frame.

Another interesting aspect of this approach relies on the fact that it is very versatile in terms of applicability (considering other vehicles or mechanical systems, for instance), since different vibration control and EH methods could be employed by simply replacing the circuit. Here, the semi-active piezoelectric switching techniques (SSDVa and SSSC) are used for vibration reduction and the remainder of this chapter describes the main characteristics of both the electromechanical structure and the control circuit considered. Furthermore, the control resulting from the circuit action does not depend on previous knowledge of any characteristics of the aerodynamic system neither on any external sensors nor complex control algorithm. That is, it depends on the capacity of the piezoelectric elements in converting mechanical to electrical energy and on the circuit topology.

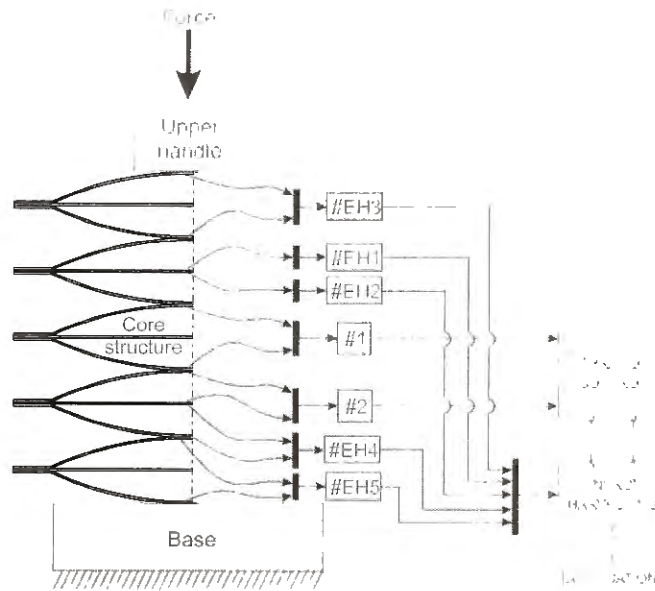


Figure 16 – Schematics of the working principle of the SaPPL device.

#### 4.1 Elementary structure of SaPPL device

The basic structure of the SaPPL (figure 17a) is based on the cymbal and moonie flextensional transducers (DOGAN; UCHINO; NEWNHAM, 1997; OCHOA et al., 2002; ONITSUKA et al., 1995). Such transducers generally consist of a piezoelectric element connected to a flexible mechanical structure that converts (transversal to axial motion) and amplifies the output displacement (and also the strain) of the piezoelement, therefore, combining the contribution of the  $d_{33}$  and  $d_{31}$  piezoelectric properties to provide an effective  $d^{eff}$  value (KIM et al., 2004). Figure 17b illustrates the cymbal device, which basically comprehends a disc-shaped piezoelement sandwiched by two metal caps and is usually employed regarding energy harvesting applications.

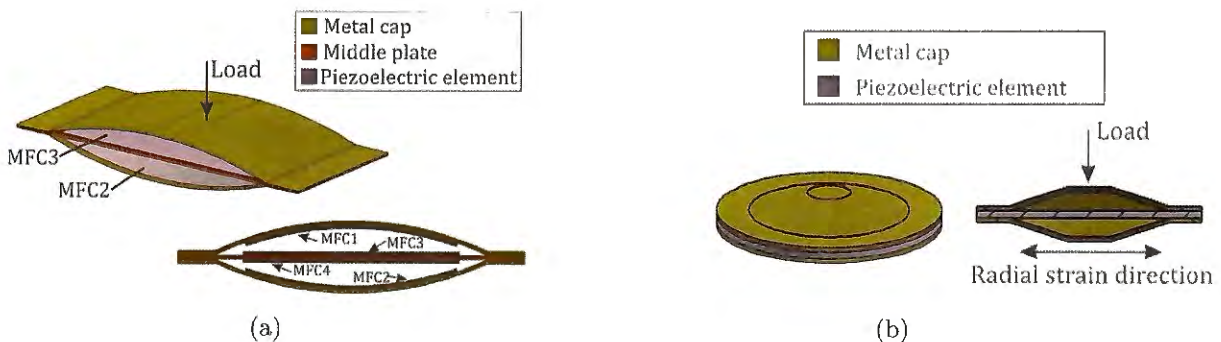


Figure 17 – Schematics illustrating (a) the elementary structure of the SaPPL device and (b) the cymbal flextensional structure.

The elementary structure of the SaPPL has an electromechanically coupled flat plate bracketed by two *Macro Fiber Composite* (MFC) piezoelectric patches (MFC3 and MFC4,

in figure 17a) and two curved metal caps, each one with a MFC piezoelectric patch bonded on the inner surface (MFC1 and MFC2 in figure 17a). The current design was chosen to accommodate as many piezoelements as possible, allowing series (or parallel) electrical connections between them in attempt to increase the voltage (or current) generation if required and, eventually increase the vibration reduction effect. An enlarged version of the elementary structure was first designed and manufactured. This version was used during the preliminary characterization tests performed in a bench top setup. In addition, the structural components were assembled using a set of bolts and nuts (instead of using an adhesive material, such as, epoxy resin) so that changes of the prototype configuration could be easily performed (for example, modify or remove the center plate). Table 1 summarizes the dimensions and properties of the enlarged elementary structure manufactured. However, it is important to point out that such dimensions are not suitable to perform experimental tests in the whirl tower facility housed in Carleton University, where the rotational tests were performed. The facility required a reduced scale device and the adjustments performed to achieve such requirements are described in section 4.2 along with the description of the first complete prototype SaPPL device.

Table 1 – Parameters of the enlarged (version) elementary structure.

Domain	Parameters	Magnitude
<b>Structural</b>	Material	Cr-Mn Steel Alloy (AISI 5160)
	Length ( $L_b$ )	145.0 mm
	Height ( $h_b$ )	10.41 mm
	Thickness ( $t_b$ )	0.5 mm
	Width ( $w_b$ )	70.0 mm
	Mass density ( $\rho_b$ )	7850.0 kg/m <sup>3</sup>
	Young's modulus ( $E_b$ )	205.0 GPa
<b>Piezoelectric</b>	Model	MFC 8557-P1
	Length ( $L_p$ )	103.0 mm
	Thickness ( $t_p$ )	$\simeq 0.3$ mm
	Width ( $w_p$ )	64.0 mm
	Mass density ( $\rho_p$ )	5440.0 kg/m <sup>3</sup>
	Dielectric constant	
	$\epsilon_{11} = \epsilon_{22}$	0.455 nF/m
	$\epsilon_{33}$	9.08 nF/m
	Piezoelectric constant	
	$e_{31} = e_{32}$	-0.1768 C/m <sup>2</sup>
$e_{15}$	0.0044 C/m <sup>2</sup>	
$e_{33}$	12.3696 C/m <sup>2</sup>	

The material specified to manufacture the elementary structure was a high carbon and chromium steel alloy, also know as spring steel. This alloy, designated by AISI 5160, exhibits outstanding toughness, a high level of ductility, and excellent fatigue resistance, which are important characteristics for applications involving cyclic and periodic loading, such as the pitch link. In addition, its yield and ultimate strength are considerably



high and might get to 1793MPa e 2220MPa, respectively, if a heat treating is performed properly (FREUDENBERGER et al., 2009). The structure was designed through numerical simulation using software ABAQUS to assure the structure would not experience yielding nor plastic behavior during the experimental tests (the yield strength is approximately 276MPa for the annealed AISI 5160 steel alloy, the same condition of the alloy employed to manufacture the enlarged structure). In other words, one might say the structure would only be exposed to linear elastic deformation in case a dynamic load was applied to the center point of the upper metal cap. Nevertheless, the structure would operate properly even if yielding occurs (except for stresses close to the ultimate strength) because the selected Cr-Mn steel alloy has high tenacity.

The numerical simulation was performed considering a concentrated harmonic load (160 Hz) of 32N magnitude while a simply supported boundary condition was set to the external contact surface of the lower metal cap. The force amplitude matches the maximum load provided by the electrodynamic shaker used in the experimental tests, thus, assuring the material would not experience failure during the tests. Figure 18 shows the simulation result and indicates the maximum stress is 190,5MPa, which strongly suggested the structure would resist to the loading applied during the benchtop tests. Furthermore, since the concentrated load used in the simulation does not occur in the experimental test, where the load is transmitted to the structure through the force sensor, the simulation corresponded to a much more severe condition. That is, since the experimental setup transmitted the force through a larger area, the compressive stress experienced by the structure, which is inversely proportional to the area, is lower (compared to the concentrated loading condition).

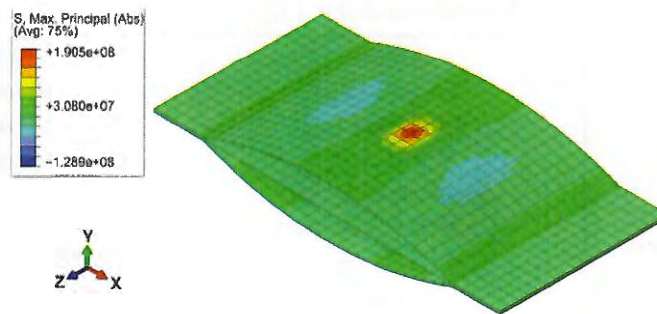


Figure 18 – Maximum mechanical stress on the elementary structure of the SaPPL when an harmonic load (frequency of 160 Hz and amplitude of 32 N) is employed.

Figure 19 presents the first 4 mode shapes of the SaPPL's elementary structure for the simplified geometry (without the fixing holes and bolt/nut sets). Such simplifications were performed to avoid meshing issues and did not cause significant changes to the overall behavior of the mode shapes (and their respective frequencies) that are most relevant to the proposed application. Information regarding the mode shapes and phase difference of the three metallic parts that compose the elementary structure was fundamental to design

the semi-active control circuit (as will be later discussed), since the electromechanical structure holds two non-collocated<sup>1</sup> piezoelements, which may result in undesired phase difference between the electric response of these elements. Therefore, the control circuit, which performs switching operations on specific periods, might have its configuration altered according to the phase difference of the piezoelements.

It is important to notice that the excitation force should be applied at the central point of the upper metal cap surface, as illustrates figure 17a (the same situation should occur in experimental tests of the complete SaPPL in a whirl tower). In this case, if the elementary structure is assembled accordingly (avoiding geometrical asymmetry issues, for instance) the structure would not exhibit torsion mode shapes. In addition, if one considers a case where the excitation frequency is tuned to the structural resonance frequency, given the elementary structure geometry, only mode shapes corresponding to bending would emerge, affecting mostly the piezoelements attached to the metal caps. On the other hand, the piezoelectric layers of the central plate deform mostly in the longitudinal direction (x-coordinate in figure 19) due to the working principle of flextensional transducers. Furthermore, when exciting the structure in its first resonance frequency, for instance, the piezoelements attached to the central plate would experience voltage cancellation issues as reported in the literature (ERTURK et al., 2009). Hence, such characterization process is fundamental to define which operational conditions for the elementary structure result in a better performance of the system.

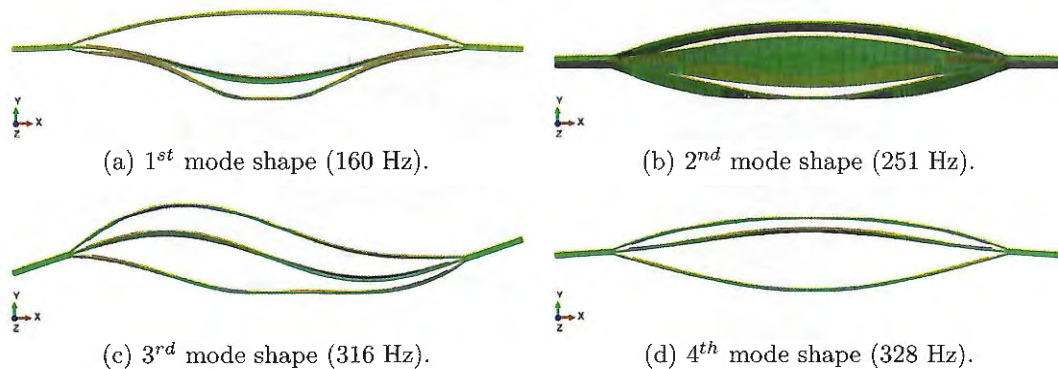


Figure 19 – First 4 mode shapes of the elementary structure (with geometry simplification) simply-supported at the bottom metal cap.

In fact, by analyzing figure 19 it is possible to note the phase difference between the upper metal cap and the central plate (piezoelectric elements 1, 3 and 4). Regarding the 1<sup>st</sup> mode, for instance, the piezoelements 1 and 3 are close to in-phase condition whereas for the 2<sup>nd</sup> mode they are almost 180° out of phase. Both phase conditions are

<sup>1</sup> Co-localization should be understood as the condition in which two piezoelectric elements have a location in a three-dimensional space where two spacial coordinates coincide. A bimorph beam (or plate), for example, has both surfaces covered by piezoelements where the position of each element (both relative to the same spatial reference) differs only thickness-wise.

required for the stiffness control technique hereafter presented, as described in section 4.3.2. Nevertheless, it is important to emphasize that both unimorph and bimorph configuration were experimentally tested with the enlarged version of SaPPL's elementary structure and the results are presented in chapter 5. The unimorph configuration was used only during preliminary tests.

## 4.2 The electromechanical structure of the SaPPL device

A schematic of the 1<sup>st</sup> version of the complete SaPPL device is shown in figure (20a), where five elementary structures are combined in a stack configuration to form the device's core structure. The dimensions of the elementary structure were chosen accordingly to fit in the whirl tower of Carleton University since there are geometrical restrictions to install a pitch link in the test facility (in special, those involving the connections between the pitch link, pitch horn and hub parts). The combination of 5 elementary structures provides flexibility to electrically connect, in series (or parallel), piezoelements of different elementary structures in order to increase the voltage (or current) supplied to the control circuit. Such association might be necessary since smaller MFCs used in this version (required due to limited room in whirl tower) produce lower voltage output.

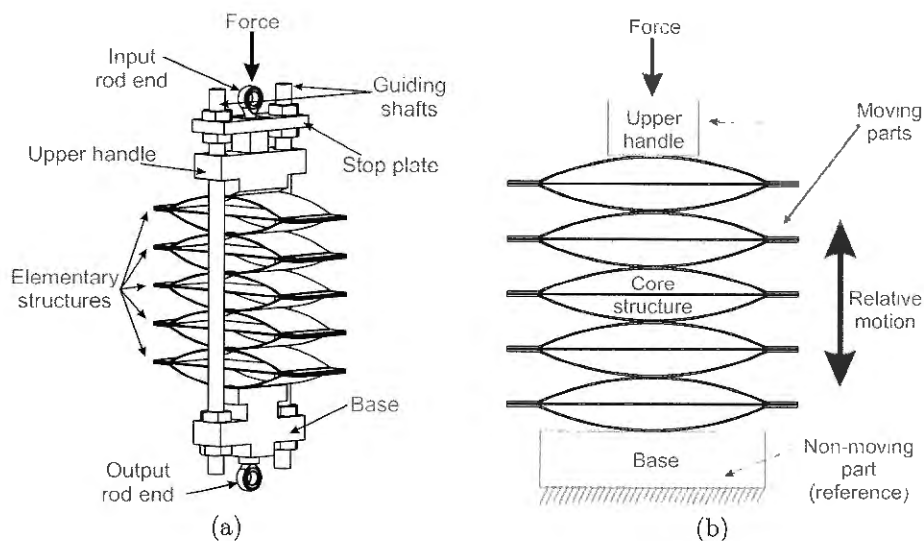


Figure 20 – Schematics of the electromechanical structure of the SaPPL prototype illustrating its (a) tridimensional view and (b) working principle.

Table 2 summarizes the dimensions of both the enlarged and reduced scale SaPPL's elementary structure. From there one may notice that two different MFCs were employed in the reduced scale version, which was also due to the dimensional and geometrical restrictions of the whirl tower facility. However, it is important to highlight the stacked configuration includes a total of 20 piezoelectric elements and, thus, allows using different piezoelements regarding different purposes, such as vibration control and energy harvesting,

for example. Therefore, the reduced potential of smaller piezoelectric elements individually should not affect the overall performance of the device.

The material specified to manufacture the elementary structure was the same high carbon and chromium steel alloy (AISI 5160) employed in the enlarged scale structure. However, the reduced scale elementary structure of SaPPL was tempered and oil quenched in attempt to obtain a higher ultimate strength. Figure (21) shows the result of a tensile test performed with three different specimens from where it can be inferred the mean ultimate strength and mean Young Modulus of 1320.5 MPa and 118.8 GPa, respectively. The specimens dimensions were 200.0 mm, 20.0 mm and 0.5 mm (length, width and thickness, respectively), according to the Standard Test Methods for Tension Testing of Metallic Materials (AASHTO, 2013); and the tests were performed in an Universal Testing Machine (Instron 5985).

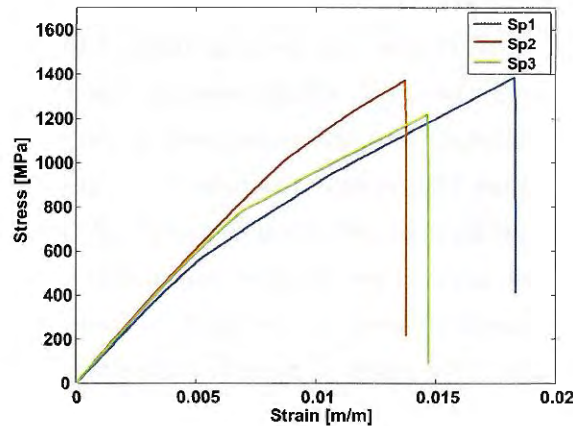


Figure 21 – Tensile testing results of SaPPL elementary structure material (AISI 5160) after tempering and oil quenching heat treating.

The first prototype of the SaPPL device was manufactured such that all interfaces

Table 2 – Parameters of elementary structure for enlarged and reduced versions.

Domain	Parameters	Elementary Structure Type		
		Enlarged scale	Reduced scale	
Structural	Material	Cr-Mn Steel alloy (AISI 5160)		
	Length	145.0 mm	80.0 mm	
	Width	70.0 mm	27.0 mm	
	Height	10.4 mm	15.2 mm	
	Thickness	0.5 mm	0.5 mm	
Piezoelectric	Model	M8557-P1	M4010-P1 ( <i>metal cap</i> )	M4312-P1 ( <i>flat plate</i> )
	Length	103.0 mm	50.0 mm	60.0 mm
	Width	64.0 mm	16.0 mm	21.0 mm
	Height	-	-	-
	Thickness	≈ 0.3 mm	≈ 0.3 mm	≈ 0.3 mm

between different parts were performed through a threaded connection (except sliding between the shaft and bearings). In fact, each elementary structure (including the enlarged version) was assembled using a set of bolts and nuts to facilitate the assembly procedure as well as other adjustments during the experimental tests. Moreover, to form the stacked configuration, all elementary structures were connected to each other also using a set of bolts and nuts, where the bottom metal cap of one elementary structure was connected to the top metal cap of the subsequent one. This connection was implemented to avoid the disassemble of the core structure due to the centrifugal force action during the whirl tower tests. However, it is important to point out that some of the threaded connections used in the SaPPL could be replaced by rivets or even other non-mechanical fixing techniques such as adhesive or welding, which might be useful to reduce the device's overall volume and mass.

In general, the working principle of the device can be described as follows: the electromechanical structure, excited by the loading induced from aeroelastic oscillations that occurs on the blades of the main rotor, converts mechanical energy (strain) to electrical energy (voltage/current) and the processing of the produced electrical signal by the controller circuits alters the energy dissipation or the equivalent stiffness of the device. Consequently, the mechanical vibration transmitted through the new pitch link is mitigated. From the mechanics point of view, one might say the structural part of the SaPPL device was designed to work in a condition that causes relative transverse movement between its constitutive parts. Figure 20b illustrates the movement direction of the core structure and indicates the region of applied force as well as the part that performs the transverse relative motion and the fixed frame of the device. Hence, apart the core structure, the SaPPL's structure includes the following parts:

- The "**upper handle**" part, made of 6061-T6 aluminum alloy, is responsible for applying the load originated from aeroelastic interactions to the core structure, which is fixed to the moving part by two small screws. In addition, this part contains two axi-symmetric holes to allow the insertion of two guiding shafts. Each hole houses a *KS Permaglide*<sup>®</sup> bearing model PAPZ 0406P10, which is designed for dry running (i.e., it contains dry lubricant and therefore does not require any lubricant).
- A **base** part, also made of 6061-T6 aluminum alloy, supports the core structure of the SaPPL device and connects the device to the fixed frame of the hub assembly. Two axi-symmetric holes allow to fix the two guiding shafts that pass through this part.
- The **stop plate** limits the "upper handle" movement, preventing the device from dismantling in case an excessive tensile load is applied to the core structure thus, involving, higher displacements.

- Two **guiding shafts**, manufactured by *MISUMI USA, Inc.* and made of 52100 bearing steel, guide the "upper handle" movement while the SaPPL is operating. With both ends threaded, the shafts are fixed to the stop plate and base parts by a set of nuts, allowing a relative motion between the "upper handle" and base parts. Therefore, the stop plate and base form the device's fixed frame relative to the "upper handle" (moving part);
- Finally, two **#MM-3-T rod ends** manufactured by *Aurora Bearing* are responsible for connecting the "upper handle" and base parts to the pitch horn (moving part of the assembly) and swash-plate (fixed part of the hub assembly), respectively.

Figure (22) shows another schematic of the SaPPL device and illustrates the coding used to identify the MFC elements according to its location in the device. The elementary structures are numbered in ascending order from top to bottom and inside each elementary structure the numbering follows the same pattern of figure (17a). Hence, the MFC elements of the SaPPL device are described by the  $ux-y$ , where  $u$  stands for unit<sup>2</sup>,  $x$  represents the elementary structure (or unit) number and  $y$  refers to the MFC element number of the elementary structure  $x$ .

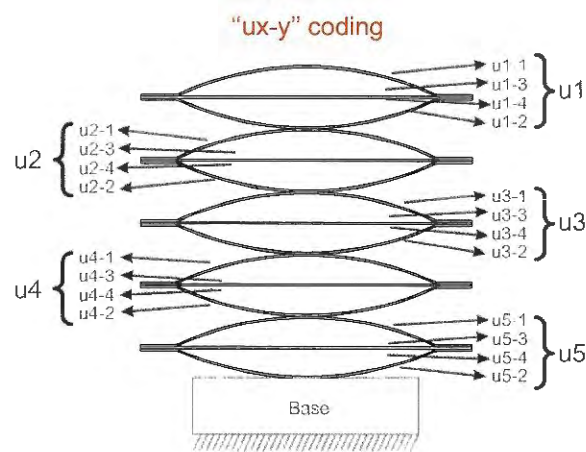


Figure 22 – Schematics showing the coding employed to identify each MFC element and elementary structure of the SaPPL device.

### 4.3 Piezoelectric control circuits

The control circuits presented in this section refer to the concept of the semi-active switching circuits, SSDVa and SSSC, mentioned in chapter 2. The employed switching system was based on the semi-passive circuit (SSDS and SSDI techniques) that was recently applied for *flutter* suppression by the research group of which the author is a member (D'ASSUNCAO; De Marqui Jr., 2015). The following sections describes the

<sup>2</sup> This term is used instead of "elementary structure" to simplify the notation in figures and plots.

working principle of each technique employed and the correspondent circuits developed to implement them. Here, the topology presented for the SSDVa circuit demands a single piezoelectric element to operate properly whereas the SSSC circuit requires at least two piezoelements. However, an important characteristic of the SSSC circuit is that it can be employed for both stiffness and damping control techniques considering minor modifications in the topology, as will later described.

#### 4.3.1 Damping control circuit - SSDVa technique

The control strategy of the SSDVa circuits (figure 23) consists on activating the switch  $S_{w1}$  when a local maximum (positive) piezoelectric voltage is detected.  $S_{w1}$  closes during a brief period of time ( $\Delta t$ ) and connects the piezoelectric element to an inductor  $L$  (which has a parasitic resistance  $R_{in}$ ). The resulting  $RLC$  circuit causes a voltage inversion that is complemented by a negative voltage source  $V_{s1}$  in order to compensate for internal losses of the circuit. The switch  $S_{w2}$  operates in a similar fashion for negative voltages. When a local minimum is detected, during the negative half cycle,  $S_{w2}$  closes and the piezoelectric material is connected to the inductor. Thus, the piezoelectric voltage inverts but a positive voltage source  $V_{s2}$  is employed to improve the voltage inversion. Here, it is relevant to point out that considering the piezoelements are subject to harmonic excitation (without DC component) both  $V_{s1}$  and  $V_{s2}$  should be symmetric, i.e. must have the same voltage amplitude with opposite polarity.

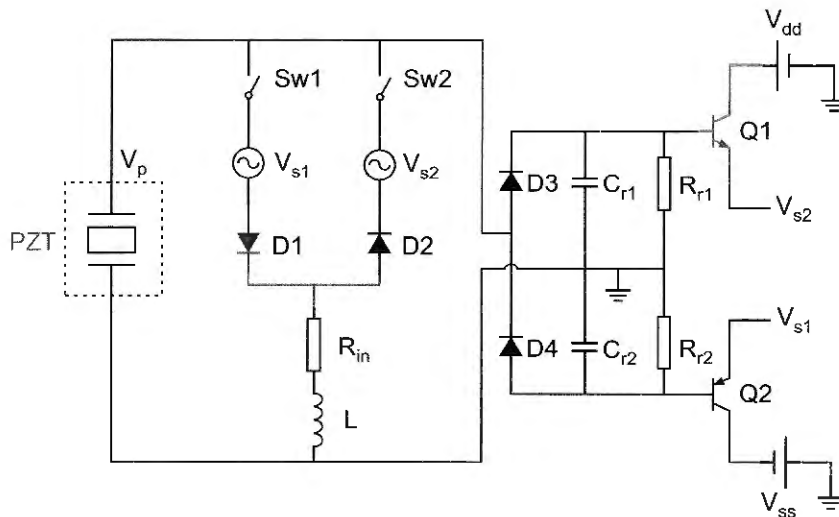


Figure 23 – Schematics of the SSDVa circuit (1<sup>st</sup> version) that operates with a single piezoelectric element and adaptive voltage sources ( $V_{s1}$  and  $V_{s2}$ ).

The voltages  $V_{s1}$  and  $V_{s2}$  are obtained from the half-wave rectifier circuit composed of the diodes D3 and D4, capacitors  $C_{r1}$  and  $C_{r2}$ , resistors  $R_{r1}$  and  $R_{r2}$  and transistors Q1 and Q2. In this circuit, the diode D3 allows the current flow during the positive half-cycle but remains in open circuit condition during the negative half-cycle. In other

words, D3 forces a positive polarity on the output signal of the capacitor  $C_{r1}$ , resistor  $R_{r1}$  and transistor Q1 regardless the polarity produced by the piezoelectric material. Using only D3, however, does not rectify the input signal as shows figure 24, where the dashed line (characterizing only the positive half-cycle) represents the case when there is no  $C_{r1}$ . Although the resulting voltage signal is always positive in that case, its amplitude varies between 0 and  $(\max(V_p) - V_D)$ , with the same oscillation frequency of the input signal. Hence, in order to reduce such oscillations (or *ripple*) and, therefore, obtain a higher voltage level, one should add the capacitor  $C_{r1}$  to the circuit. The capacitor charges when the input voltage signal increases toward the maximum value and discharges when the signal decreases. In this sense, if  $C_{r1}$  and  $R_{r1}$  are adjusted accordingly such that the discharging period is longer than one cycle of the input signal, a low ripple occurs and the voltage output should approximate a continuous signal (DC - direct current), as shows the voltage waveform of figure 24 (dash-dotted line).

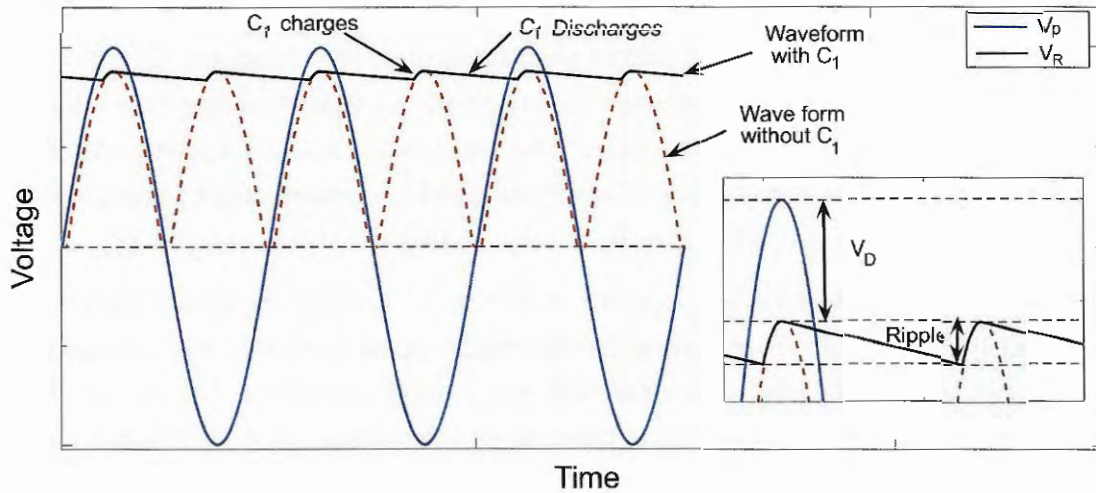


Figure 24 – Voltage waveform (output) of a half-wave rectifier circuit.

The voltage amplitude of the *ripple* is given by

$$V_{ripple} = \frac{2\pi}{\omega R_{r1} C_{r1}} \max(V_p) \quad (4.1)$$

where  $\omega$  is the frequency of the input signal ( $V_p$ ).

In the proposed SSDVa circuit, the intention was not to obtain a low *ripple* level. According to the literature, high values of ripple may be achieved when  $V_{ripple} > 0.1 \max(V_p)$ . Thus, the capacitance  $C_{r1}$  is obtained using the following expression

$$C_{r1} < \frac{20\pi}{\omega R_{r1}} \quad (4.2)$$

and one should note that  $C_{r1}$  depends on the value of  $R_{r1}$ , which has not been determined yet. Hence, assuming the rectifier circuit must not consume a significant power



( $P_{r1}$ ) level from the piezoelectric material and that the amount of power dissipated in  $R_{r1}$  can be approximated by

$$P_{r1} = (\max(V_p) - V_D)^2 / R_{r1}, \quad (4.3)$$

it is possible to conclude that  $P_{r1}$  is low when high values of resistance are employed, such as  $R_{r1} = 10 \text{ M}\Omega$ .

The rectified voltage (with high *ripple* level) is transferred, then, to the base of transistor Q1, which is set to operate in the Emitter-Follower (or Common Collector) configuration (figure 23). This means the voltage across the transistor's emitter follows the same behavior of its base, regardless a minor reduction of the amplitude depending on the voltage drop of the emitter-base junction of the component used (the voltage drop usually varies between 0,3 V and 0,7 V). Given such condition, the transistor Q1 allows that most part of the current flowing through its terminals is transferred from the emitter to the collector (more than 99% in most cases) and, as consequence, a low current level flows through the base. Hence, the positive (control) voltage  $V_{s2}$  is transferred by the transistor's (Q1) base while the current related to  $V_{s2}$  is supplied by the voltage source  $V_{dd}$ .

It is important to highlight that the equations 4.1 and 4.2 are valid while the input voltage signal is constant or increases. As the input signal decreases, the voltage across  $C_{r1}$  drops exponentially and, so occurs with the voltage across the base of Q1. Hence, the control action performed by  $V_{s2}$  is reduced and decreases until  $V_{s2}$  reaches the new input voltage level. In case the input voltage ceases, the control action decreases until it is null. The components D4,  $C_{r2}$ ,  $R_{r2}$  and Q2 operate within the negative half-cycle of the harmonic signal in a similar fashion as occurs with R3,  $C_{r1}$ ,  $R_{r1}$  and Q1, since the rectifier circuit is symmetric (figure 23). The control voltage  $V_{s1}$  is then transferred through the base of Q2, and the current corresponding to  $V_{s1}$  is obtained from the voltage source  $V_{ss}$ .

In this sense, it is possible to notice the adaptive characteristics of the proposed circuit as it is able to adjust the voltage level required to complement the voltage inversion (typical of standard SSDV technique) according to the excitation level of the electromechanical structure. Figure 25 shows the voltage waveform across the electrodes of the piezoelectric element after the action of the proposed SSDVa circuit, where  $V_{neg}$  is the negative voltage at the end of a switching operation that has occurred at the time instant related to the maximum amplitude of the piezoelectric voltage ( $V_{pmax}$ ) and  $V_{pos}$  is the positive voltage after switching at a minimum value ( $V_{pmin}$ ).

As previously discussed, the control voltage ( $V_s$ ) is applied during the processing performed by the control circuit in order to increase (artificially) the inversion factor ( $\gamma$ ). Hence, the resulting voltage at the end of each switching action (related to  $S_{w1}$  and  $S_{w2}$ )

might be written as

$$V_{neg} = -(V_{pmax} + V_{s2}) \gamma_i - V_{s2} = -\gamma_f V_{pmax} \quad (4.4)$$

$$V_{pos} = (V_{s1} - V_{pmin}) \gamma_i + V_{s1} = -\gamma_f V_{pmin}. \quad (4.5)$$

Here  $\gamma_i$  is the initial inversion factor (equivalent to  $\gamma$  related to the SSDI circuit, i.e., without the application of any control voltage) and  $\gamma_f$  is the final inversion factor resulting from the non-linear management occurred in the SSDVa case. After rearranging equations 4.4 and 4.5, it is possible to calculate the amplitude of the control voltage as

$$V_{s2} = -V_{pmax} \frac{\gamma_f - \gamma_i}{1 + \gamma_i} \quad (4.6)$$

$$V_{s1} = -V_{pmin} \frac{\gamma_f - \gamma_i}{1 + \gamma_i} \quad (4.7)$$

$$V_s = -\max(V_p) \operatorname{sgn}(V_p) \frac{\gamma_f - \gamma_i}{1 + \gamma_i} \quad (4.8)$$

where  $\operatorname{sgn}(V_p)$  is the sign function of  $V_p$ .

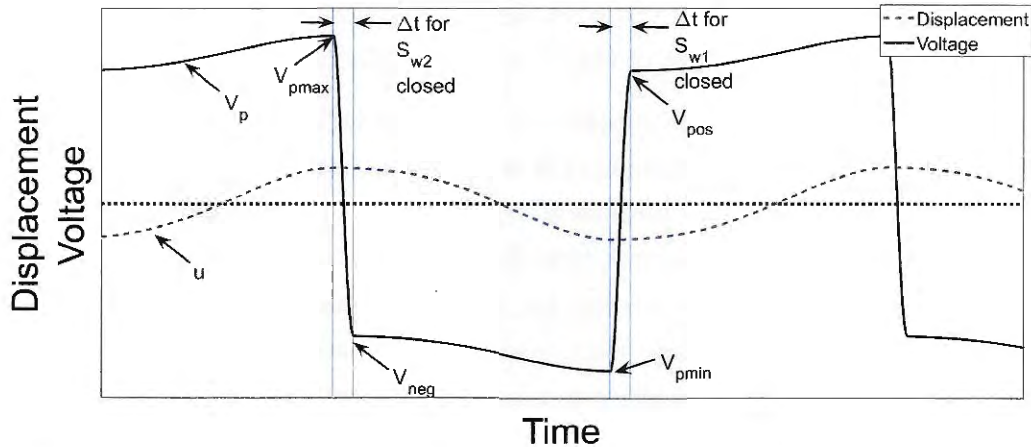


Figure 25 – Typical waveform of resulting voltage signal after the processing of SSDVa circuit.

Nevertheless, after performing different tests with this version of the SSDVa circuit it was clear that the application point of the control voltage was not suitable (before the inductor, as shows figure 23) because the voltage inversion was exclusively caused by the external voltage sources instead of being a consequence of the switching actions. To avoid such problem but still keep the adaptive characteristic of the circuit a few changes were performed in that topology and a second version was developed. Figure 26 shows the 2<sup>nd</sup> version of the SSDVa circuit, which basically can be divided into four sub-circuits: a standard SSDI circuit developed by Richard, Guyomar and Lefeuvre (2007), a differentiator circuit, a symmetric voltage rectifier<sup>3</sup> and a symmetric switching circuit.

<sup>3</sup> The term symmetric is employed to express that the same type of rectification occurs for the positive

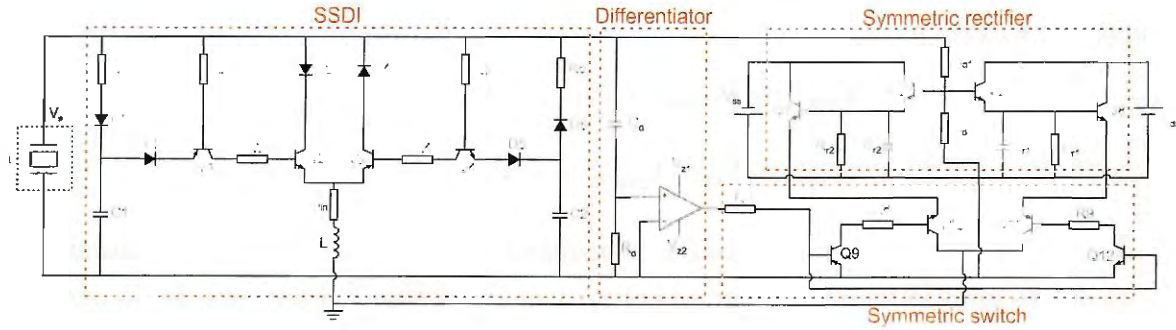


Figure 26 – Schematics representing the 2<sup>nd</sup> version of the SSDVa circuit.

In this circuit, to obtain the voltage  $V_s$ , the process starts from the amplitude reduction of  $V_p$ , using a voltage divider composed of  $R_{d1}$  and  $R_{d2}$ . The reduced voltage is transmitted to the (symmetric) half-wave rectifier that consists of transistors Q5, Q6, Q7 and Q8, capacitors  $C_{r1}$  and  $C_{r2}$ , resistors  $R_{r1}$  and  $R_{r2}$ . The elements Q6,  $C_{r1}$  and  $R_{r2}$  operate as the conventional half-wave rectifier, where the NPN transistor Q6 performs, here, the same function of a diode since it allows current flow only during the positive half-cycle. In an analogous way, the components Q5 (PNP transistor),  $C_{r2}$  and  $R_{r2}$  operate during the negative half-cycle. In terms of *ripple* level, the rectification process has the same characteristics and requisites of the 1<sup>st</sup> version of the SSDVa circuit.

Moreover, since the current supplied by the piezoelectric element is not enough to properly power the circuit, this version still requires the use of external voltage sources ( $V_{ss}$  and  $V_{dd}$ ) that share with the piezoelements the function of supplying current to the circuit (i.e., part of the electric current that flows into this version of SSDVa circuit - in special, the switching sub-circuit - is provided by the external sources). In a self-sufficient case, on the other hand, the voltage sources would be replaced by piezoelectric elements exclusively set as power supply to activate the switches and generate the control voltage. Besides, it is important to notice that both rectified voltages ( $V_{r1}$  and  $V_{r2}$ ) are proportional to the maximum and minimum values of  $V_p$ , since the operation of transistors Q6 and Q5 (Emitter-Follower configuration) occurs during the positive and negative half-cycle of  $V_p$ , respectively. Therefore, if the (external) mechanical excitation of the electromechanical system increases,  $V_p$  increases and, consequently,  $V_{r1}$  and  $V_{r2}$  as well. In contrast, if the excitation decreases,  $V_p$  is reduced and the amplitudes of  $V_{r1}$  and  $V_{r2}$  decrease exponentially according to the time constant  $\tau = RC$  of the rectifier circuit, due to the presence of the capacitors  $C_{r1}$  and  $C_{r2}$  (the same way it would occur in the previous version of the SSDVa circuit).

After the rectification process, the voltages  $V_{r1}$  and  $V_{r2}$  must be transferred synchronously with the switching actions and for this purpose, the derivative and switching

---

and negative half-cycle, resulting in two distinct signals. Hence, one must not confuse such circuit with a full-wave bridge rectifier.

circuits are used. The capacitor  $C_d$  and the resistor  $R_d$  are responsible for differentiating the voltage signal  $V_p$  and the resulting differentiated signal ( $V_d$ ), which is used as reference for the switching operation, may be represented by the following equation

$$V_d = \frac{j\omega C_d R_d}{1 + j\omega C_d R_d} V_p \quad (4.9)$$

where  $j$  is the imaginary unit. Since  $\omega C_d R_d \ll 1$  (since  $C_d$  is a very low value, reaching the order of  $10^{-9}$  F), the equation (4.9) may be simplified to

$$V_d = C_d R_d \dot{V}_p \quad (4.10)$$

and the voltage signal  $V_d$  is transferred to the positive input port of the operational amplifier (OpAmp1), which in turn, generates a squared voltage signal  $V_o$  (with the same polarity of  $V_d$ ) that commands the ON/OFF switch either activating the transistors Q9 and Q10 (positive half-cycle) or the transistors Q12 e Q11 (negative half-cycle). Hence, the voltage across the collector of Q11 (i.e.,  $V_{s1}$ ) has, approximately, the same amplitude of  $V_{r1}$  as well as Q12 delivers the control voltage  $V_{s2}$ , with the amplitude of  $V_{r2}$ , approximately.

Regarding the circuit shown in figure 26, the control voltage  $V_s$  (combination of  $V_{s1}$  and  $V_{s2}$ ) can be written as

$$V_s = \frac{R_{d2}}{R_{d1} + R_{d2}} \max(V_p) \operatorname{sgn}(V_d) \quad (4.11)$$

where the expression  $\operatorname{sgn}(V_d) = -\operatorname{sgn}(V_p)$  is valid during the whole switching action. So, rearranging  $V_s$  accordingly

$$V_s = -\frac{R_{d2}}{R_{d1} + R_{d2}} \max(V_p) \operatorname{sgn}(V_{pi}) \quad (4.12)$$

and setting equation (4.8) equal to equation (4.12) it is possible to express  $V_s$  in terms of the initial and final inversion factor

$$V_s = -\frac{R_{d2}}{R_{d1} + R_{d2}} \max(V_p) \operatorname{sgn}(V_p) = -\max(V_p) \operatorname{sgn}(V_p) \frac{\gamma_f - \gamma_i}{1 + \gamma_i} \quad (4.13)$$

and

$$\frac{R_{d2}}{R_{d1} + R_{d2}} = \frac{\gamma_f - \gamma_i}{1 + \gamma_i} \quad (4.14)$$

Several values of  $R_{d1}$  and  $R_{d2}$  satisfy equation (4.14). However, in order to keep low power consumption in these resistors, as well as in  $R_{r1}$  and  $R_{r2}$ , one should select higher resistances that range from  $10^6 \Omega$  to  $10^7 \Omega$ , for example. The components  $C_d$  and  $R_d$ , of the derivative sub-circuit, also admit several values that make the following expression,

$\omega C_d R_d \ll 1$ , valid. In this case, it is appropriate that the capacitor impedance ( $Z_{C_d} = \frac{1}{j\omega C_d}$ ) be as higher as possible since the circuit should consume low power from the piezoelectric material. Thus,  $C_d$  should have values around the order of magnitude of  $10^{-8}\text{F}$  to  $10^{-9}\text{F}$ , approximately (besides, the  $RC$  derivative circuit work properly if the time constant of the circuit is lower than the period of the input voltage). The resistors  $R_7$  to  $R_9$  must have high values (same order of magnitude as  $R_{r1}$  and  $R_{r2}$ ) such that are still capable of transferring the control current  $I_s$  from the collector to the emitter of both transistors Q10 e Q11. As these transistors are in saturation mode, the current flowing through their bases must satisfy the following expression

$$I_{b2}\beta_2 > I_c \quad (4.15)$$

where  $\beta_2$  is a non-dimensional parameter given by the manufacturer of the component (usually is greater than 100) and  $I_{b2}$  is the current flowing through the base of Q10 and Q11. The transistors Q9 e Q12 have, approximately, the same amount of current flowing through their collectors, respectively, ( $I_{c1} = I_{b2}$ ). Therefore, the following relation is valid

$$\beta_1 I_{b1} = I_{c1} \quad (4.16)$$

$$I_{b1} = \frac{V_o - 0.7}{R7} = \frac{I_{c1}}{\beta_1} > \frac{I_c}{\beta_1\beta_2} \quad (4.17)$$

$$R7 < \frac{(V_o - 0.7)\beta_1\beta_2}{I_c}, \quad (4.18)$$

where  $I_{b1}$  is the current that flows through the base of Q9 and Q12. Taking as reference, for example, an common voltage level at the output of OpAmp1,  $V_o = 5\text{V}$ ,  $\beta_1 = \beta_2 = 100$  e  $\max I_s = 43\text{mA}$ , the resistors R7 to R9 admit the following values

$$R7 < \frac{4.3 \times 10^4}{4.3 \times 10^{-2}} = 10^6 \Omega \quad (4.19)$$

$$R8 = R9 < 10^5 \Omega. \quad (4.20)$$

Once the values of each component have been defined, one should have by the end of this process a SSDVa circuit capable of complementing, in adaptive way, the voltage inversion of the standard SSDI circuit.

#### 4.3.2 Stiffness control circuit - SSSC technique

The circuit developed for the SSSC technique operate in a similar fashion as the SSDVa circuit. The difference in each case is basically the instant at which the switching action occurs. In the SSSC case, the switching occurs when the structural displacement is zero (instead of occurring at points of maximum and minimum displacements, in

consonance with the SSD techniques), which alters the stiffness of the system. The stiffness variation results from an adjustment between the phase of the voltage generated by the piezoelectric material ( $V_p$ ) and the structural displacement ( $\mathbf{u}$ ) of the electromechanical structure. If there is a phase matching condition, the resulting effect is an increase of stiffness, denominated hardening effect. On the other hand, if the phase difference is  $180^\circ$ , the resulting equivalent stiffness is reduced, phenomenon that is called softening effect. Figure 27 shows the waveform of each phenomenon.

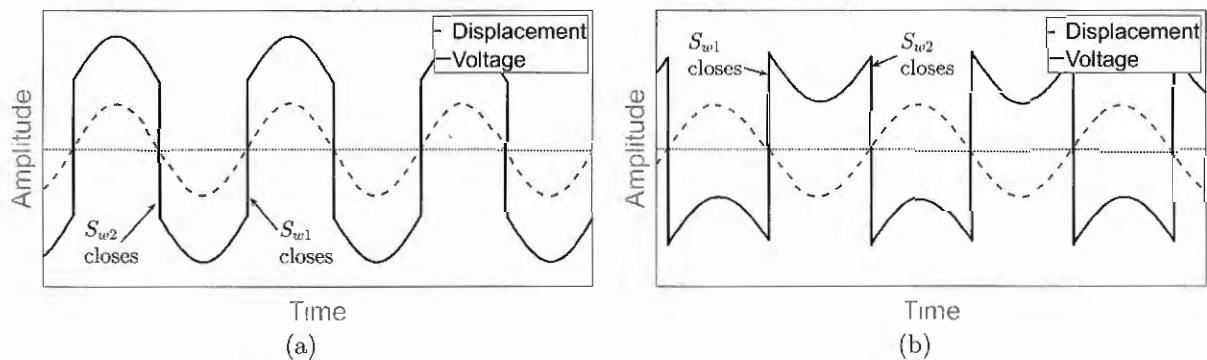


Figure 27 – Voltage and displacement waveforms of the piezoelectric element resulting from the SSSC technique: (a) SSSC-H (hardening) and (b) SSSC-S (softening) cases.

In terms of circuit, it is possible to obtain the hardening or softening effect according to the activation of the switches  $S_{w1}$  and  $S_{w2}$ . If the switch  $S_{w1}$  activates while the slope of the displacement is positive after zero-crossing occurs (and  $S_{w2}$  activates while the slope of the displacement is negative after zero-crossing) the hardening effect occurs. Conversely, in case the switch  $S_{w1}$  activates while the displacement decreases after zero-crossing (and  $S_{w2}$  activates while the displacement increases after zero-crossing), the softening effect is obtained.

Likewise in the SSDVa case, one must consider a control voltage  $V_s$  to increase the inversion factor of the circuit and, as consequence, increase the stiffness variation effect. A different aspect of this circuit is that it requires at least two piezoelectric elements to operate properly and each one should exclusively account for either the switching action or generating the control voltage. Hence, due to the use of different piezoelements for both tasks it is essential to evaluate the phase of both voltage signals and adjust the circuit, if required, in order to guarantee the switching actions occur at instants of zero structural displacement. The resulting equivalent stiffness ( $\bar{K}_{eq}$ ) and the new resonance frequency ( $\omega_{eq}$ ) of the system obtained during the operation of the control circuit were presented in chapter 2 (equations 2.6 and 2.7).

The semi-active circuit employed in this work for vibration control purpose is presented in figure 28. The control circuit, which is capable of producing damping (SSDVa)

or stiffness (SSSC) control, can be divided into the following sub-circuits:

- **Zero/extrema detector:** composed of the resistor  $R_z$ , Zener diodes  $D_{z1}$  and  $D_{z2}$  and the operational amplifier OpAmp1;
- **Symmetric voltage regulator:** composed of transistors  $Q1$ ,  $Q2$ ,  $Q5$  and  $Q6$ ; capacitors  $C_{d1} \dots C_{d2n}$ ,  $C_{s1} \dots C_{s2n}$  and  $C_{r1}$ ,  $C_{r2}$ ; diodes  $D_{d1} \dots D_{d2n}$  and  $D_{s1} \dots D_{s2n}$ ; and resistors  $R_{p1}$ ,  $R_{p2}$ ,  $R_{p3}$  and  $R_{p4}$ ;
- **Filter:** its composition depends on the type of filter employed and also the topology implemented;
- **Symmetric switch:** composed of  $Q7$ ,  $R2$ ,  $Q8$  and  $D1$ , for the positive half-cycle ( $S_{w1}$ ), and  $Q10$ ,  $R3$ ,  $Q9$ ,  $D2$ , for the negative half-cycle ( $S_{w2}$ );
- **OpAmp symmetric supply:** composed of  $D_{z3}$ ,  $D_{z4}$ ,  $R_{r1}$ ,  $R_{r2}$ ;  $Q3$  and  $Q4$ .

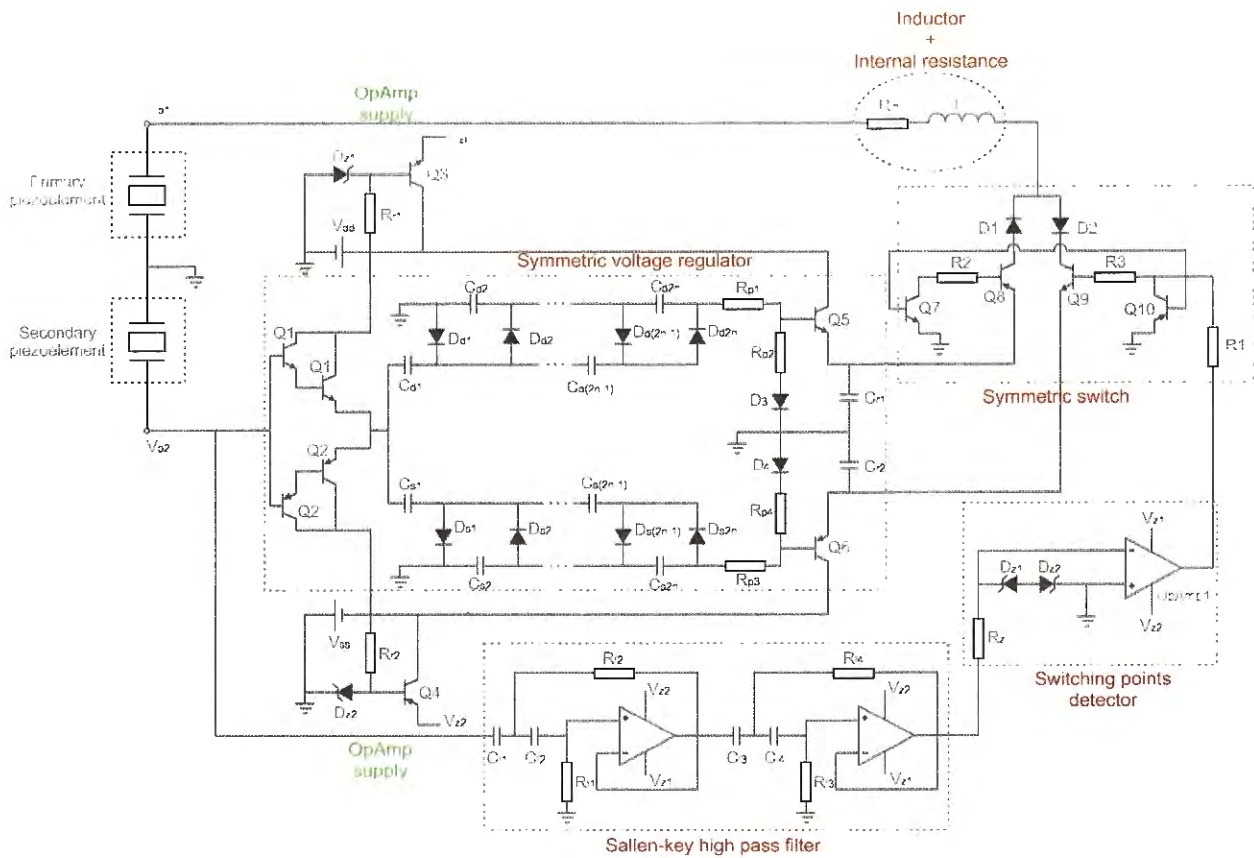


Figure 28 – Schematics of the proposed circuit for damping or stiffness control.

In this circuit, the primary piezoelectric set (referenced using the sub-index 1) and secondary piezoelectric set (referenced using the sub-index 2) produce the voltage signals  $V_{p1}$  and  $V_{p2}$ , respectively. The primary set is connected (intermittently) to the inductance  $L$  and accounts for the control operation while the secondary set provides (as

long as the switch is active) the additional voltage required to improve (artificially) the inversion coefficient. Since the secondary set is part of the controlled structure, the extra voltage supplied has adaptive characteristics, as long as this set remains in open circuit condition. Therefore, variations in the amplitude of the structural motion (displacement) are proportionally reflected in variations of the voltage signal

$$V_{p2} = -\frac{\theta_2^t \mathbf{u}}{C_{p2}}, \quad (4.21)$$

where  $\theta_2^t$  is the electromechanical coupling of the secondary set.

The Secondary set is simultaneously connected to two branches of the circuit, one including a voltage regulator and the other a filter connected in series to a zero/extrema detector. The voltage regulator sub-circuit is a symmetric (positive/negative) multi-stage voltage multiplier that includes  $n$  blocks (each containing two diodes and two capacitors) connected in series. Each block corresponds to one phase of amplification and rectification of the AC voltage signal  $V_{p2}$ , which results in a higher rectified voltage level compared to a single-stage rectifier. Hence, during the positive half-cycle the process occurs through the components  $C_{d1} \cdots C_{d2n}$  and  $D_{d1} \cdots D_{d2n}$ , as for the negative half-cycle through  $C_{s1} \cdots C_{s2n}$  and  $D_{s1} \cdots D_{s2n}$ . The resultant voltage, described as

$$V_r = \pm (n + 1) \frac{\theta_2^t (\mathbf{u}_{\max})}{C_{p2}}, \quad (4.22)$$

is transferred to a voltage divider (resistors  $R_{p1}$ ,  $R_{p2}$  and diode D3) in order to better adjust the amplitude level before transmitting the voltage to the transistors Q5 and Q6, which are in the emitter-follower configuration. In that mode, the voltage across the emitter ( $V_s$ ) is a copy of the base voltage (with its amplitude decreased by the voltage drop across the base-emitter junction,  $V_{BE}$ ) and may be, approximately, written as

$$V_s = \pm (n + 1) \frac{\theta_2^t (\mathbf{u}_{\max})}{C_{p2}} \frac{R_{p2}}{R_{p1} + R_{p2}} = \pm \beta \frac{\theta_2^t \mathbf{u}_{\max}}{C_p} \text{sgn}(\mathbf{u}_{(t-\tau)}) \quad (4.23)$$

$$\beta = (n + 1) \frac{R_{p2}}{R_{p1} + R_{p2}}, \quad (4.24)$$

where  $\beta$  is defined as the gain of the controller circuit and  $\mathbf{u}_{(t-\tau)}$  is the structural displacement at the  $\tau$  instant right before the displacement reaches zero. The instant  $\tau$  should be as small as possible (close to zero) and, in practical applications, it is required to determine if the displacement is increasing or decreasing after it reaches zero.

At the same time, the voltage produced by the secondary set is transferred to the filter in order to activate the switches only at the target frequency or bandwidth selected (i.e., vibration spectrum that should be attenuated). The type of filter employed depends on the desired application and for the pitch link case it could be a band-pass filter if a



single frequency is targeted or a high-pass filter if a broader bandwidth is targeted. Here, a two stage analog filter implemented using the Sallen-Key topology was selected to execute this task and the selection of each component depends on the filter characteristics. The voltage signal processed by the filter is transferred to the zero/extrema detector that is the sub-circuit responsible for defining the proper moments of the switching operations, either using the damping or stiffness control technique. In this sense, the function of OpAmp1 is to generate a square wave ( $V_o$ ) in order to activate the switching sub-circuit.

Regarding the input port of OpAmp1, the only restriction for SSDVa case is that both the primary and secondary piezoelectric sets must be in phase. On the other hand, for the SSSC case, the input port used in OpAmp1, positive or negative, will define whether softening or hardening effects occur, as presents table (3). In addition, it is important to mention that since the SSSC technique is the default configuration of the control circuit, the component OpAmp1 is set as zero crossing detector. Hence, changing its configuration to the SSDVa approach requires a  $90^\circ$  phase shifting (delay or forward) of the square wave produced. In the current configuration of the control circuit this modification is performed by including an  $RC$  derivative circuit in parallel to the input port of OpAmp1. The results of this operation are further discussed in section 5.1.3.

Table 3 – Configuration relative to the input port of OpAmp1 to obtain hardening or softening effects.

Effect	Operational conditions		
	Phase between $V_{p1}$ and $V_{p2}$	OpAmp1 Input	
		Positive	Negative
Softening	0	$V_1$	0
	$180^\circ$	0	$V_1$
Hardening	0	0	$V_1$
	$180^\circ$	$V_1$	0

After activating the operational amplifier, the square voltage output ( $V_o$ ) is transmitted to the transistors Q7 and Q8 during the positive half-cycle to briefly activate the switch and provide  $V_s$  to the resonant circuit formed between the piezoelectric primary set and the inductor  $L$ . In a similar fashion, during the negative half-cycle the transistors Q10 and Q9 are activated to transfer the  $-V_s$  voltage to the resonant circuit. The switching sub-circuit does not require high current ( $I_o$ ) levels to operate and, therefore,  $R1$  might be set to values around the order of magnitude of  $10^6$  M $\Omega$  (as consequence,  $I_o$  will have  $10^{-6}$  A order of magnitude). In addition, the resistor  $R_z$  should take values that guarantee an open circuit condition for the secondary set while the reverse voltage of the Zener diodes  $D_{z1}$  and  $D_{z2}$  depend on the operational amplifier requirements (usually, it ranges from 5 V to 10 V in order to avoid overload or saturation issues).

Finally, it is worthwhile noting that the voltage supplied to the component OpAmp1

( $V_{z1}$  and  $V_{z2}$ ) was exclusively provided by the secondary piezoelectric set but the required electrical current was complemented by an external power supply. Therefore, the circuit was not self-sufficient yet and further investigations that should be carried out in this sense are discussed in chapter 6. Furthermore, it is important to mention that differently from the circuit discussed in the previous sections (that use the switch circuit proposed by Richard, Guyomar and Lefeuvre (2007)), the switch circuit topology presented in this section is an original contribution of the author in a collaboration with the research group which he is part of.

#### 4.4 Final Remarks

This chapter presented the concept of a new pitch link proposed for vibration control and energy harvesting purposes. The new device, designated by Smart Piezoelectric Pitch Link (SaPPL), would be capable of mitigating the vibratory load transferred from the rotating frame of a helicopter to the fuselage (fixed frame) as well as provide a low power energy source in the rotating frame. A prototype of the device was developed to perform vibratory benchtop test as well as whirl tower rotating experiments in order to investigate its behavior in such conditions. The structure was designed such that its dimensions were feasible for installing it in the whirl tower test facility of Carleton University. The control circuit developed accounts for both damping and stiffness switching control techniques. However, an important aspect of the proposed device is that it does not rely exclusively on such circuit to work properly. In fact, the SaPPL device versatility regarding the circuitry is one of its main advantages since different control techniques could be employed by simply replacing the control circuit.



## 5 EXPERIMENTAL RESULTS

This chapter reports the experimental bench top tests performed to investigate the behavior of the SaPPL device when connected to the developed semi-active circuits (SSDVa and SSSC) as well as describes and discusses the performance of the system in whirl tower tests. The corresponding results are shown to illustrate the ability of the proposed system to reduce the vibration amplitude at a specific frequency or bandwidth and are separated in two basic parts: the first contains the preliminary tests of a bimorph electromechanical beam and an enlarged version of the SaPPL's elementary structure, which were both employed to develop the control circuits as well as to characterize the working principle of the elementary structure; whereas the second part shows the experiments carried out with the prototype of the SaPPL device, which includes vibratory benchtop tests and whirl tower rotating tests. Part of these tests were performed at Carleton University, Canada, where different configurations of the SaPPL's core structure were tested in setups that should mimic the loading experienced by pitch links, as will be discussed in this chapter. The whirl tower facility comprehends a reduced scale one-bladed rotor hub that was manufactured to facilitate the installation of pitch link prototypes and, therefore, enables to investigate the performance of different pitch links in terms of vibration reduction in conditions that simulate the hover flight of helicopters.

### 5.1 Preliminary tests performed during the development of the control circuits

The tests reported in this section refer to the development of the nonlinear shunt circuits to attenuate the load transferred through the SaPPL device. First, the experiments were performed with an electromechanically coupled beam-like structure. Later, the experimental investigation performed with an enlarged prototype of SaPPL's elementary structure is discussed, whereas both cases account for the connection of the control circuits. Understanding the behavior of the electromechanical system (composed of the elementary structure and control circuit) was useful to define strategies for the experimental tests with the complete version of the SaPPL device (benchtop and whirl tower).

#### 5.1.1 Case A - Bimorph beam connected to the 1<sup>st</sup> version of the SSDVa circuit

The first tests were carried out with an electromechanically coupled structure composed of two *QP10N* piezoelectric elements (manufactured by *Midé Technology*) bonded to the lower and upper face of an aluminum beam-like substrate having the following dimensions: 120.3 mm × 27.75 mm × 1.0 mm. The cantilever was subjected to harmonic base excitation and only the upper piezoelement was connected to the nonlinear shunt circuit (the other remained in open circuit condition).

The excitation due to an electromagnetic mini-shaker (model 4810, manufactured by *Brüel & Kjaer*) was driven by a *SIEMENS SCADAS* signal generator and a power amplifier (model 2706, manufactured by *Brüel & Kjaer*). The base acceleration was monitored using a low mass ICP accelerometer (manufactured by *PCB Piezotronics Inc.*), the tip velocity of the beam was measured using a laser Doppler vibrometer (model *Polytec PDV-100*) and the control circuit was monitored by measuring the voltage at specific points of the circuit such as the voltage produced by the piezoelement ( $V_p$ ) and the control voltage ( $V_s$ ). The data acquisition was performed using the SCADAS system, depicted in figure 29a along with the equipment setup employed in the tests, and a two-channel DC power source supplied the current/voltage required by the SSDVa circuit that is implemented in a breadboard (the circuit schematics is depicted in figure 23).

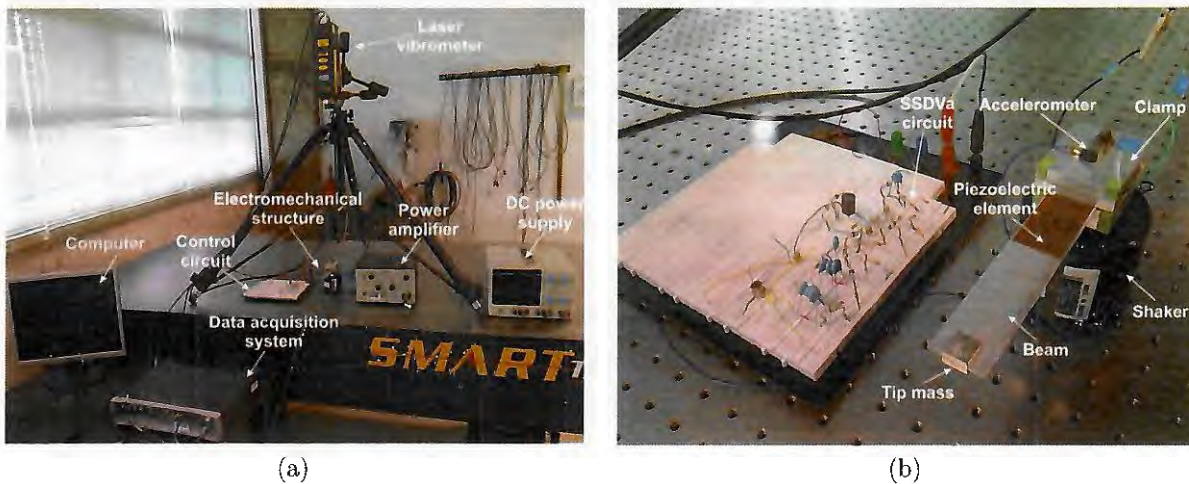


Figure 29 – Equipment setup used during the experimental tests: (a) general view and (b) detailed view of the electromechanical beam and control circuit.

The experimental tests were carried out to estimate the Frequency Response Function (FRF) of the electromechanical structure (tip velocity over base acceleration), first in open-circuit condition in order to determine the structural natural frequency and consequently define the inductance that should be used in the nonlinear shunt circuits, and later considering the effect of the SSDVa circuit to assess its performance regarding the vibration reduction. The open-circuit condition FRF (electrodes of the piezoelectric element connected to a load resistance of  $1M \Omega$ ) was the reference case.

The FRFs were calculated using the  $H_1$  estimator, with the base acceleration (input) and beam tip velocity (output) signals, considering a sample rate of 1600 samples/s, 8193 samples and 30 averages. The result (figure 30a) indicates the natural frequency is, approximately, 35.9 Hz for the open circuit condition and confirms that the SSDVa circuit outperforms the SSDS and SSDI, as reported in the literature. Figure 30b compares the voltage waveform of the piezoelectric elements for the SSDI and SSDVa cases when

the excitation frequency was tuned to the open-circuit natural frequency. Here, one may observe that the voltage obtained from the SSDVa circuit exceeds the voltage achieved with the SSDI technique, which, therefore, results in higher energy dissipation for the first case, as observed in figure 30a. In addition, it is important to note the presence of the peaks in the amplitude of  $V_s$ , which proves the switching action indeed occurred and also indicates the control voltages ( $V_{s1}$  and  $V_{s2}$ ) are delivered at the proper time instant. However, as described in section 4.3.1, there were some issues related to this version of the SSDVa circuit (figure 23) and it was eventually replaced by a new enhanced version (figure 26). The results of the new configuration are discussed next for the experimental tests performed with the enlarged elementary structure of the SaPPL device.

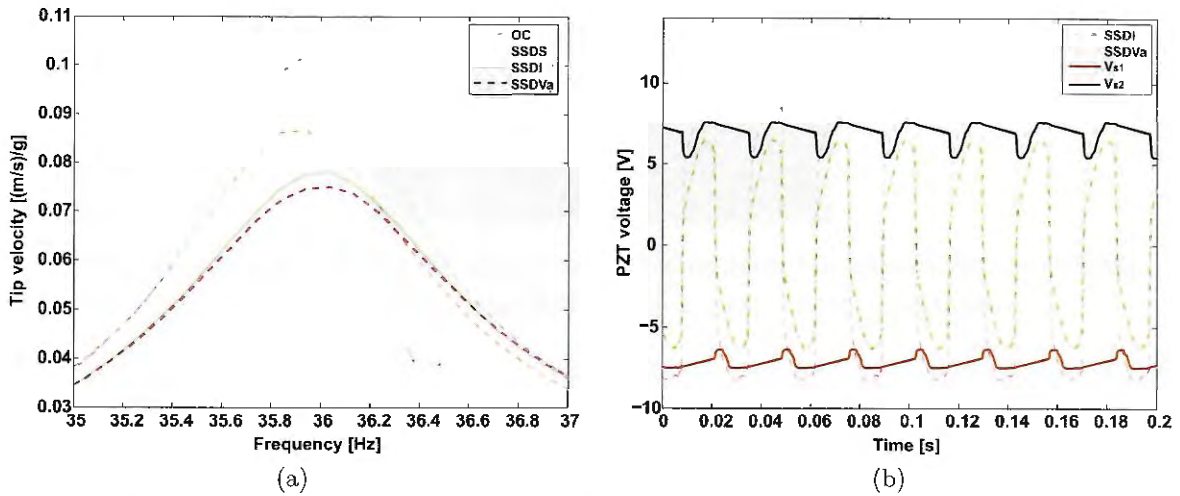


Figure 30 – (a) Effect of the control circuits on the first resonance frequency of the electromechanical beam subjected to clamped-free boundary condition and (b) comparison between the typical waveform signal (time series) for the SSDI and SSDVa cases.

### 5.1.2 Case B - SaPPL's elementary structure connected to the 2<sup>nd</sup> version of the SSDVa circuit

In this case, besides investigating the performance of the 2<sup>nd</sup> version of the SSDVa circuit (shown in figure 26), a few tests were also carried out in order to characterize the behavior of the elementary structure. As shown in figure 31, during these tests the excitation force was produced by an electrodynamic shaker (model K2007E01, manufactured by *The Modal Shop, Inc.*) that included an integrated power amplifier. The force was applied to the external surface of the lower metal cap while the upper metal cap was simply supported against a rigid plate (non-moving frame of the setup). The same *SIEMENS SCADAS* system used in *Case A* was responsible for generating the excitation signal and performing the data acquisition. Two ICP force sensors model 208C02 and 208C01 (both manufactured by *PCB Piezotronics*) monitored, each, the excitation force (input) delivered

by the shaker and the reaction force at the rigid plate while the voltages of the semi-active circuit were directly monitored using the SCADAS data acquisition system.

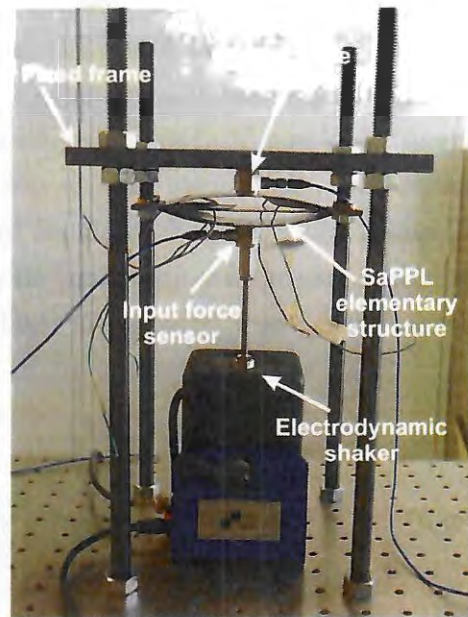


Figure 31 – Experimental setup employed in the tests of SaPPL's elementary structure considering the 2<sup>nd</sup> version of the SSDVa circuit.

For this configuration (structure-circuit) the elementary structure included three piezoelements (MFC1, MFC2 and MFC3) and, therefore, it was composed of an unimorph central plate. Hence, only the piezoelement MFC3 (attached to the central plate) was connected to the SSDVa circuit since the low voltage amplitudes produced by MFC1 and MFC2 would result in a lower performance of the control system. This amplitude difference can be observed in figure 32a, which was obtained after exciting the electromechanical structure with a sinusoidal sweep (known as chirp in the technical literature), considering a frequency bandwidth of 0 to 300 Hz. In addition, the chirp excitation test allowed to estimate the mechanical FRF (excitation force over reaction force) of the system and to verify the performance of the circuit in terms of vibration attenuation. Figure 32 shows the mechanical and electrical response signals that resulted from the chirp test, comparing the cases where the elementary structure was in open circuit condition as well as connected to the SSDI and SSDVa circuits, with the inductance adjusted to the 1<sup>st</sup> resonance frequency.

As described previously, it is important to characterize the phase difference between the voltage signal of each MFC element, specially if the employed control circuit requires two piezoelectric elements to work properly (as it would be in a self-powered case, for example). Figure 32b shows the phase difference between the voltage signals of MFC1 and MFC3 (assuming the latter as reference signal), where it is possible to observe that both signals were, approximately, 180° out of phase for the whole spectrum analyzed, except

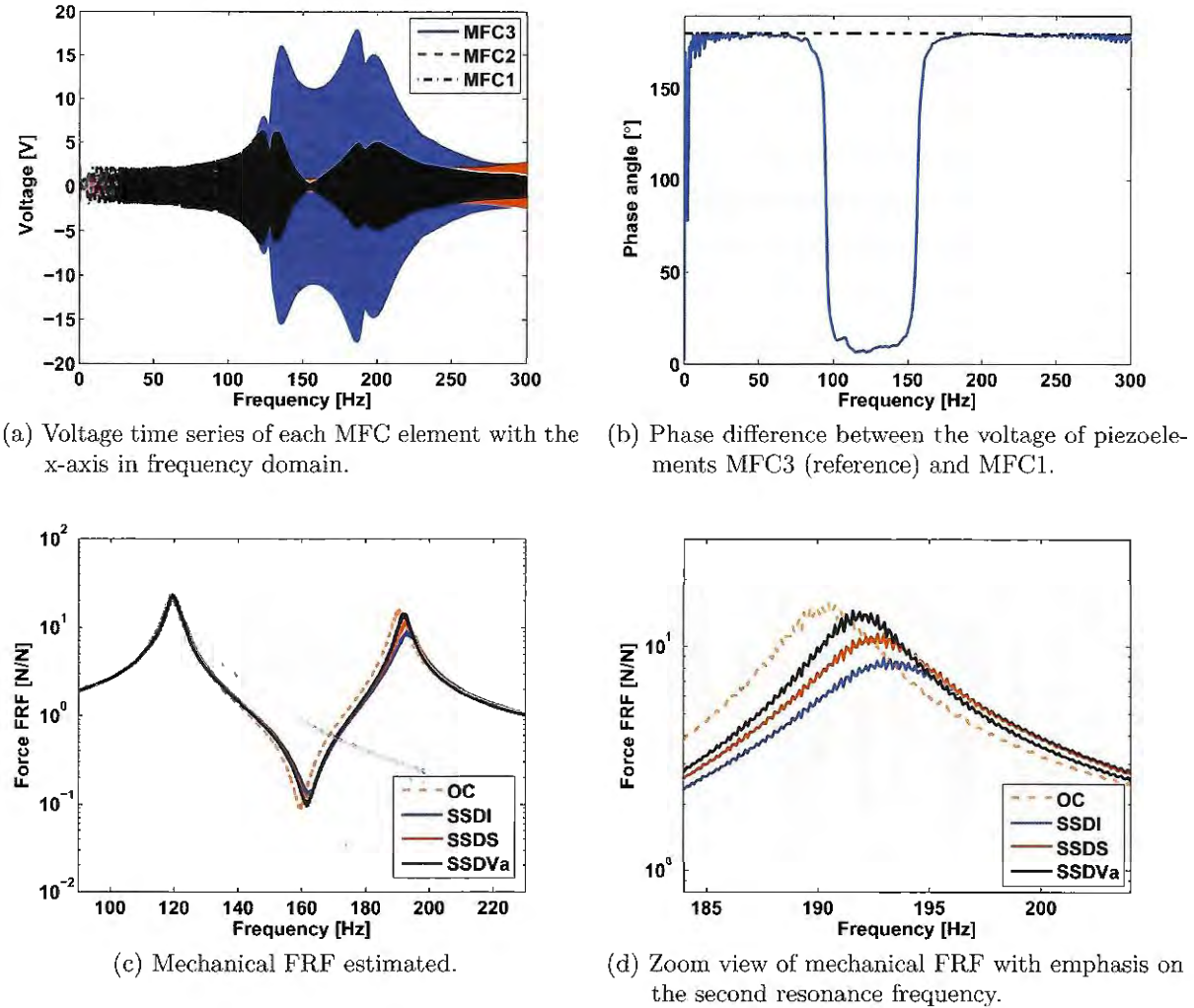


Figure 32 – Response of SaPPL’s elementary structure (enlarged version) under chirp excitation considering the open circuit condition and also the SSDVa and SSDI circuits.

for the bandwidth between 110 Hz and 140 Hz, where the phase difference is closer to zero (approximately  $6^\circ$  at 116 Hz). That is, for the first mode shape (which corresponds to 119.5 Hz) both MFC1 and MFC3 are close to the in-phase condition whereas for the second mode shape (which corresponds to 190.5 Hz) they approximate to the case where phase opposition occurs.

Figure 32c depicts the mechanical FRF estimated for the frequency bandwidth (from 0 to 300 Hz) that includes two resonance frequencies of the structure. As discussed in chapter 4, the mode shapes corresponding to these frequencies refer to the bending motion ( $1^{st}$  and  $4^{th}$  mode shapes of figure 19) since the elementary structure is excited in a region where only such type of movement occurs. Besides, by comparing the results one shall note that the circuits SSDS, SSDI and SSDVa did not influence the first resonance peak of the mechanical FRF since the resulting curves are almost overlapped with the curved



obtained for the open circuit condition (probably because of the low voltage amplitudes achieved around that frequency, as shown in figure 32a). On the other hand, attenuation is observed at the second resonance peak (as reported in the literature) for every case, except for the SSDVa circuit. The bad performance of this circuit could be explained by the fact that the switching did not occurred accordingly. By analyzing figure 33a, it is possible to observe the presence of high frequency oscillations<sup>1</sup>, which indicates the switch was closed for a longer period than it should. Such behavior of SSDI and SSDV circuits (also reported in the literature) might occur when the inversion factor is high (sometimes, greater than 1), causing instability issues in the control circuit, mainly when the switch is activated.

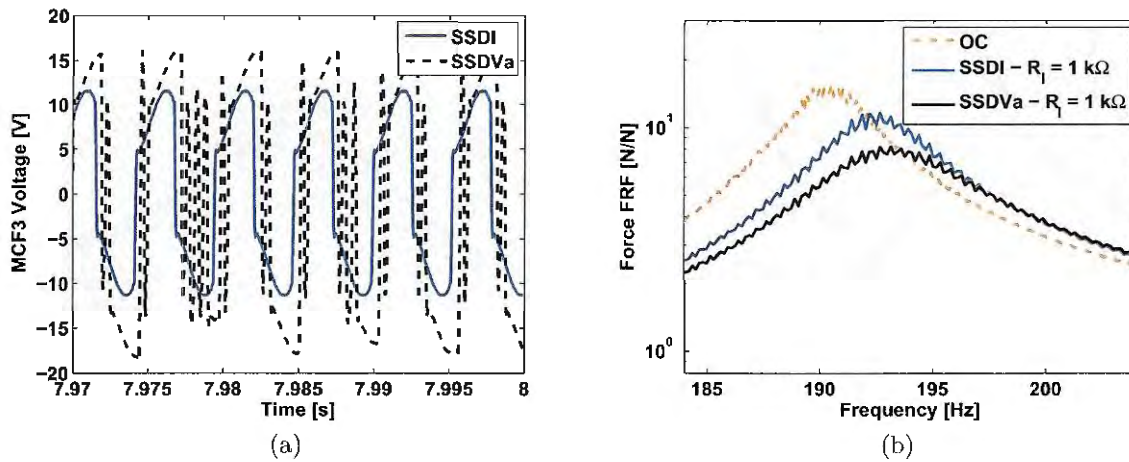


Figure 33 – (a) Voltage time series for SSDVa and SSDI circuits illustrating the switching problem and (b) mechanical FRF obtained from the tests carried out for a lower inversion factor.

A new test was performed, then, by including a  $1\text{k}\Omega$  resistor in series with the inductor of SSDVa and SSDI circuit in order to verify if the bad switching actions were, indeed, degrading the SSDVa performance. This intentional change caused a reduction of the inversion factor in both circuits and allowed comparing them in, approximately, the same condition. Figure 33b shows the mechanical FRF for this test and confirms that the SSDVa circuit outperforms the SSDI. At the resonance peak, the amplitude reduced, approximately, 60% for the SSDVa case and 46% for the SSDI, when compared to the open circuit condition. Therefore, if properly adjusted, the proposed SSDVa circuit should provide better vibration reduction.

<sup>1</sup> Such characteristic arises due to the RLC resonant circuit resulting from the connection of the inductor with the piezoelement since the electrical oscillation frequency is much higher than the mechanical one.

### 5.1.3 Case C - SaPPL's elementary structure connected to the SSSC circuit

The experimental tests of this case were carried out following the same procedure of *Case B* (figure 31) and the only difference was related to the control circuit connected to the piezoelements. During the tests, the electromechanical structure was subjected to a chirp excitation force for a frequency bandwidth ranging from 0 to 300 Hz, while the SSSC circuit processed the electrical signal produced by the piezoelectric elements in order to modify the equivalent structural stiffness. Here, the open circuit condition was also the reference case.

In this version of the SSSC circuit (figure 28), changing between the hardening and softening effects results from the proper management of the operational amplifier included in the circuit, as previously discussed in section 4.3.2. Hence, for the circuit to operate properly and the zeros detector to be correctly set, the phase between the voltage produced by the sensor piezoelement (secondary) and the voltage produced by the piezoelement related to the control action (primary) should be close to  $0^\circ$  or  $180^\circ$ . Ideally, both elements, primary and secondary, should be co-localized. However, the working mechanism of the SaPPL is not restrict to this relative location of piezoelectric materials such that it is also possible for the device to work properly if other location setup is employed, as long as the phase difference remains closer to the values mentioned (variations up to  $\pm 10^\circ$ , approximately, are still acceptable).

During the first tests with this experimental setup the elementary (electromechanical) structure of the SaPPL included three MFC elements, likewise described in section 5.1.2. In that case, neither combination of piezoelements would provide a pair of co-localized elements. Hence, the MFC elements did not have a suitable phase for a proper operation of the circuit at the frequency bandwidth analyzed and, therefore, the voltage signal produced by the secondary MFC element required a phase adjustment (forwarding or delaying it). For this version of the SSSC circuit, such adjustment was achieved by connecting a capacitor (in series or parallel) to the input port of the operational amplifier. A few tests were carried out and two values of capacitance were selected in order to investigate the influence of the phase between both the primary and secondary elements on the performance of the control circuit. Both hardening and softening effects were considered in the analyzes and the main results obtained are shown in figures 34 and 35.

Figure 34a shows the mechanical FRF of the system, which was estimated using the excitation force (input signal) and the reaction force (output) at the rigid support. The FRF exhibits two resonance peaks and indicates that both stiffness phenomena occurred for most cases analyzed since the resonance frequency shifted from the open circuit condition. Two distinct stiffness phenomena occurred for different resonance frequencies (given the same configuration of the control circuit) due to the fact that the hardening/softening configuration, in this context, depends on the phase between the voltage produced by the

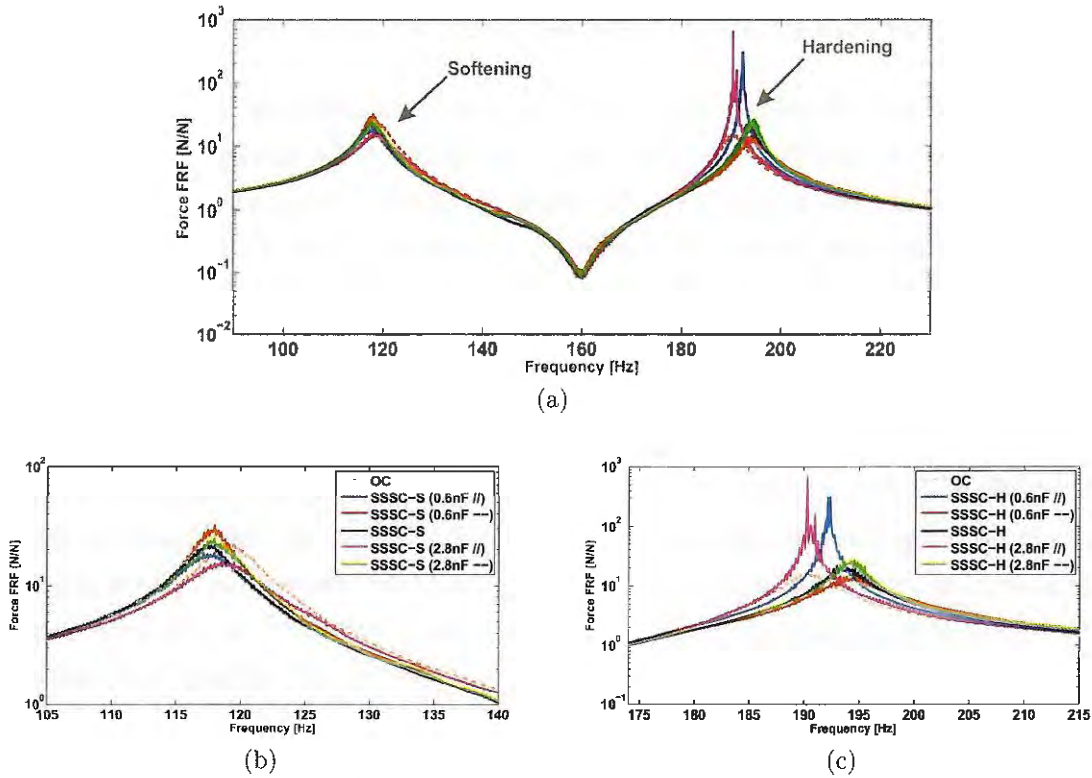


Figure 34 – (a) Mechanical FRF after connecting the capacitors (in series "--" and parallel "//") to adjust the phase, with a detailed view for (b) the **softening** effect at the 1<sup>st</sup> resonance frequency and (c) for the **hardening** effect at the 2<sup>nd</sup> resonance frequency.

primary and secondary MFC elements, and since the phase eventually varies according to the structural mode shape (and its respective resonance frequency). In fact, one may recall from figure 32b that the phase between the primary and secondary elements is close to  $0^\circ$  at the the first resonance (relative to 119 Hz, in open circuit condition), whereas for the second one (relative to 190 Hz, in open circuit condition) the phase difference is  $180^\circ$ , approximately. In other words, by keeping the same switching configuration for the control circuit, if the softening effect occurs at the first resonance frequency, the structure would experience the hardening effect at the second resonance frequency, and vice-versa. This situation proves that identifying the phase difference between the primary and secondary piezoelements is essential to have a proper operation of the SaPPL device.

Furthermore, the mechanical FRF also shows that the control circuit had a greater effect on the first resonance peak than the effect observed on the second one. Figure 34b evidences that a similar reduction occurred for every case (1.3%, approximately) except for the case where the 2.8 nF capacitor was connected in parallel. Besides, when compared to the open circuit condition, the SSSC circuit adjusted for softening at the first resonance frequency caused an amplitude reduction of approximately 32.6%. Figure 34c, on the other hand, evidences the hardening effect occurring at the second resonance peak since the peak

shifts to the right (compared to the open circuit resonance at 190.3 Hz), which indicates the circuit induced an increase on the structural stiffness. In this case, the SSSC circuit exhibited the best performance when the selected 0.6 nF capacitor was connected in series, which increased about 2.1% the resonance frequency and reduced approximately 58.2% the amplitude at the second (open circuit) resonance.

Nevertheless, it is important to mention that the control action of these techniques might affect the amplitude of other frequencies in a negative fashion. When the 0.6 nF capacitor was connected in parallel, for example, there was a significant reduction of the amplitude at 119.0 Hz but no changes occurred at 190.3 Hz. In fact, it is possible to observe that although the SSSC controller was active during this test (the frequency shift of the resonance peak indicates that), there was a significant increase on the FRF amplitude at the resonance frequency of the case '*SSSC-H* (0, 6 nF //)'- such effect was also evident in the result obtained from the test with the 2.8 nF capacitor connected in parallel, as shows figure 34c). It is possible that the phase change induced by the 2.8 nF capacitor may have degraded the circuit's performance.

In a similar fashion, when configuring the control circuit for the hardening effect at the first resonance frequency (as consequence, the softening effect occurred at the second one) it is also possible to notice from figure 35 that the performance of the SSSC circuit at the first resonance is lower than the second one. In this setup, the SSSC circuit produced an increase of approximately 1.4% at the first resonance frequency (compared to open circuit frequency, 119.0 Hz) for the cases where the 0.6 nF and 2.8 nF capacitors were connected in series. Furthermore, the best performance occurred when the 0.6 nF capacitor (series connection) was employed, reducing the vibration amplitude in about 36.5% (at 119.0 Hz). For the frequency of 190.3 Hz, it is clear that the best performance, in terms of vibration reduction, occurred when the 0.6 nF capacitor was connected in parallel (figure 35c) when the reduction was about 84%.

It is relevant to highlight, however, that among the analyzed cases for the SSSC circuit, a significant attenuation of the vibration amplitude was observed simultaneously to the stiffness variation effect (increase or decrease). Such behavior was not reported in the literature for this class of control technique. At that time, it was assumed this behavior had occurred due to the combination of damping and stiffness effects (probably due to switch delays), since the fundamental difference between the circuits responsible for such effects, SSDVa and SSSC, is the instant at which the switching action occurs (either maximum, minimum or null displacements). Therefore, by interfering on the phase of the voltage signal produced by the secondary piezoelement (sensor), it is possible that the SSSC circuit actuated combining both effects of energy dissipation and stiffness variation. This assumption was investigated during the research internship performed at the Rotorcraft Research Laboratory of Carleton University, Canada, as will be discussed next.

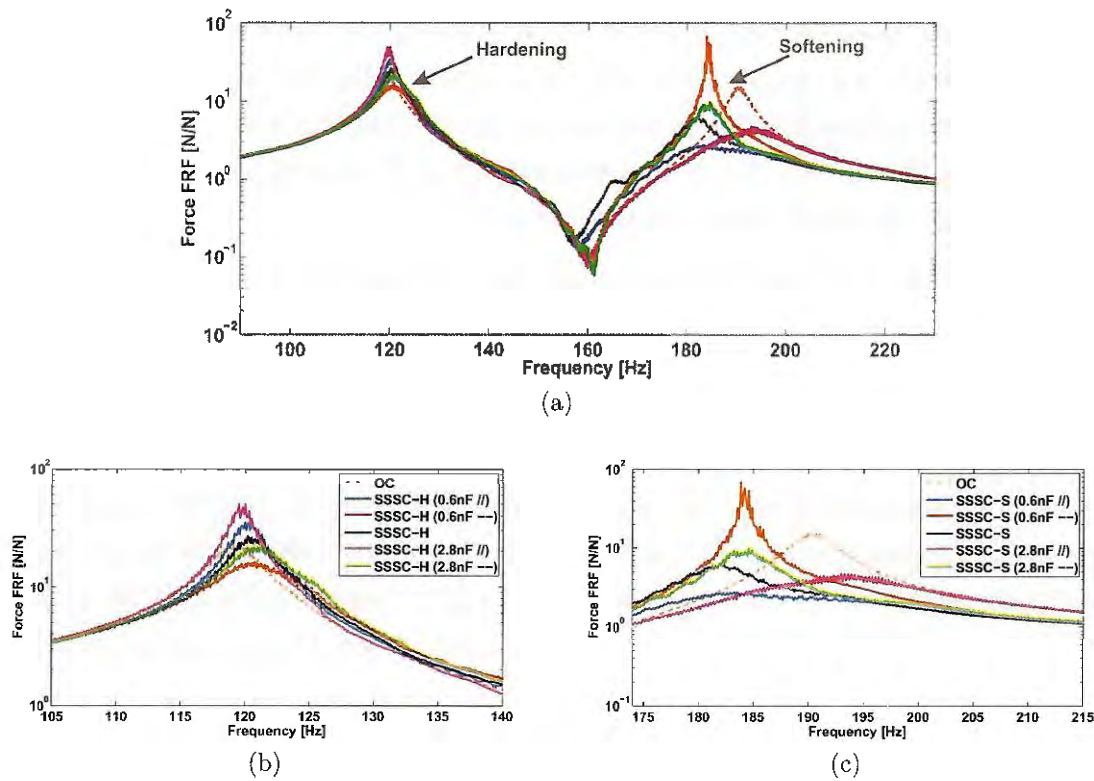


Figure 35 – (a) Mechanical FRF after connecting the capacitors (in series "--" and parallel "//") to adjust the phase, with a detailed view for (b) the **hardening** effect at the 1<sup>st</sup> resonance frequency and (c) for the **softening** effect at the 2<sup>nd</sup> resonance frequency.

Figure 36 shows the benchtop setup used in Canada, which was also used by the Rotorcraft Research Group during the development of the APL device. This experimental setup was selected in order to represent (in benchtop tests) the motion that a pitch link is subjected when connected to a helicopter blade or even during the whirl tower tests. In the benchtop tests, an electromagnetic shaker (model BK-4808) was used to excite the elementary structure with the forcing signal generated by a LMS SCADAS III data acquisition system. A closed-loop<sup>2</sup> test was implemented to guarantee a similar excitation level acting on the structure for all circuits tested and the excitation signal was monitored by an ICP low mass accelerometer placed on the shaker table.

The shaker table motion was transmitted to the elementary structure by a rigid bar (figure 36a) that is pinned to a fixture base. The motion transmitted to the structure was, approximately, half of the motion observed at the shaker coupling point. A force transducer placed between the elementary structure and the fixed base (figure 36b) was employed to measure the structural response (output) and, therefore, was used to assess the performance of each controller circuit. In addition, two 1-channel DC power supplies

<sup>2</sup> Designation used to describe a controlled excitation system, where the excitation signal is compared to a reference value and corrected if any deviation (from the reference value) occurs.

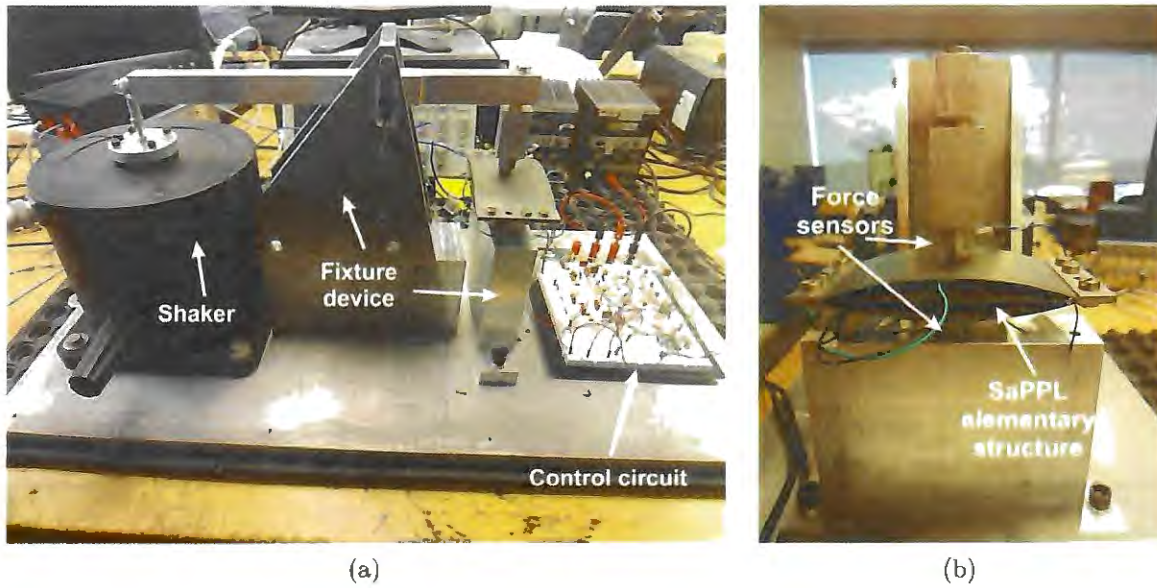


Figure 36 – Experimental setup used in the benchtop tests performed at Carleton University.

were connected in series to provide the electrical current required by the switching circuits (implemented in a breadboard, as shows figure 36a). The connection between both DC power supplies was required because the controller circuits worked with AC signals and, therefore, require a positive and negative DC current to work properly. Moreover, that version of the control circuit depended on external power supplies to operate properly. Finally, the electrodes of each MFC were connected to the breadboard circuit using screw terminal blocks. The negative electrodes were connected to the circuit's reference (ground) connection and the positive electrodes were each connected to specific points of the circuits, as already described for other tests. Table 4 shows the components used in the control circuit (its schematic is presented in figure 28). It is important to mention here that a fourth MFC element (MFC4) was attached to the central plate of the enlarged elementary structure at the opposite face where the MFC3 was attached. Hence, for these tests, the electromechanical structure comprised a bimorph central plate that included a pair of co-localized MFC elements.

During the benchtop tests a closed-loop stepped-sine excitation was considered for a frequency bandwidth ranging from 25 Hz to 220 Hz and the amplitude (input) was set to an acceleration level of 0.7g, approximately, for the whole bandwidth tested (which was selected to include the fundamental resonant frequency of the SaPPL's elementary structure). In addition, the input signal (stepped-sine) was incremented of 0.5 Hz every 10 seconds in order to ensure steady state condition. The softening (SSSC-S), hardening (SSSC-H) variations of SSSC circuit and the SSDI approach were tested, as well as the open and short-circuit conditions. Table 5 summarizes the piezoelectric elements connected to

Table 4 – Components of the SSSC control circuit.

Components	Symbol (Schematics)	Model	Characteristics	Value
Transistors	Q2, Q4, Q6, Q8, Q10	MPSA92	BJT - PNP	-
	Q1, Q3, Q5, Q7, Q9	KPS42	BJT - NPN	-
Diodes	D1 – D4, D <sub>d1</sub> – D <sub>d4</sub> , D <sub>s1</sub> – D <sub>s4</sub>	1N4004	Standard Recovery Rectifiers	-
	D <sub>z1</sub> – D <sub>z2</sub>	1N5231	Small Signal Zener Diodes	5.1 V
	D <sub>z3</sub> – D <sub>z4</sub>	NTE 5068A	Small Signal Zener Diodes	4.3 V
Operational Amplifier	OpAmp1	LM358P	-	-
Resistors	R1-R2	-		1 k $\Omega$
	R3 – R4	-		1 M $\Omega$
	R5 – R6	-		10 M $\Omega$
	R7	-	Standard	1 M $\Omega$
	R8 – R9	-		10 k $\Omega$
	R10	-		1 M $\Omega$
Inductor	L	-	Choke	120 mH
Capacitor	C <sub>dn</sub> , C <sub>sn</sub> , C <sub>r1</sub> , C <sub>r2</sub>	-	Polyester	224 nF

the circuits along the tests. MFC elements not connected to the control circuits were kept in open circuit condition.

Table 5 – Piezoelectric elements of the enlarged elementary structure used in each circuit tested during the benchtop tests conducted at Carleton University.

Boundary condition / Control circuit	Piezoelectric element			
	MFC1	MFC2	MFC3	MFC4
Open Circuit (OC)	X	X	X	X
Short Circuit (SC)	X	X	X	X
SSDI			X	
SSSC			X	X

An important aspect that should be noticed is the possibility to employ the circuit depicted in figure 28 as an enhanced piezoelectric shunt damping device (*Synchronized Switch Damping*, SSD, technique), since the fundamental difference between the stiffness and damping control techniques is a  $\pm 90^\circ$  phase shift in the switching operation (as previously discussed in this chapter). Regarding the presented SSSC circuit, this phase shift can be achieved by adding a capacitor ( $C_{ph}$ ) in parallel to the positive input port of the zero detector (figure 28), where the chosen capacitance depends on the phase shift to be introduced,  $C_{ph} = tg(\phi_{add})/(\omega_{n1}R)$ . The phase between MFC3 and MFC4 signals in open circuit condition (figure 37a) is  $\phi_{34} \cong 177^\circ$ . Hence, increasing  $\phi_{34}$  to  $270^\circ$  (or  $-90^\circ$ ) would require an extra phase of  $93^\circ$ . A capacitance  $C_{ph} = 6.8\text{nF}$  was tested, providing an additional phase shift of  $81^\circ$  and a resulting phase of  $\phi_{34} = 258^\circ$  between the voltage signals of MFC3 and MFC4. Figure 37b shows the voltage signals of both MFC elements and confirms that SSSC circuit actually behaves as SSDVa controller (i.e., switching operations occurring at maximum/minimum displacement<sup>3</sup>).

<sup>3</sup> It is important to remember that voltage and displacement are in phase for open circuit condition. Therefore, maximum/minimum voltage also implies maximum/minimum displacement.

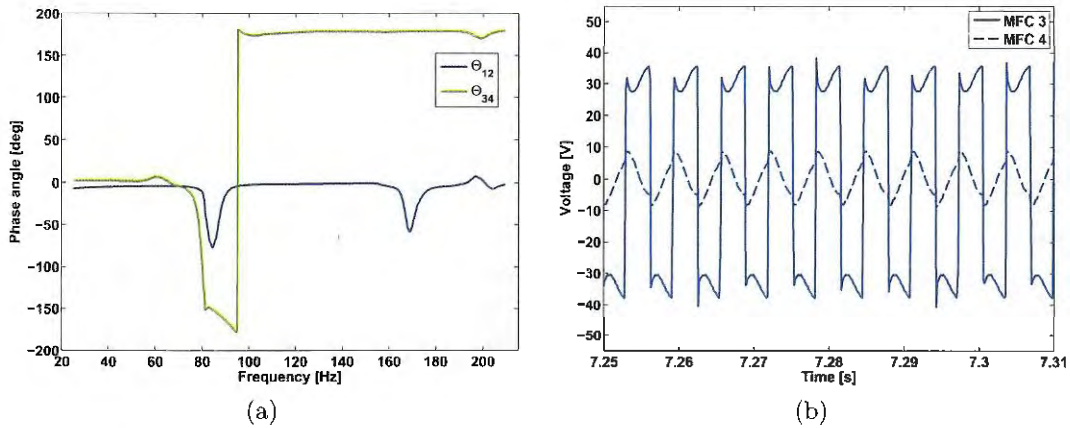


Figure 37 – (a) Phase angle between the MFC piezoelements for open circuit condition and (b) voltage waveform of MFC3 and MFC4 when the SSDVa control circuit is connected.

Figure 38a shows the frequency response of the output force measured during the benchtop tests (figure 36) when different electrical circuits were considered. In all semi-active circuits the inductor was tuned to the open-circuit resonance (target frequency) of the elementary structure. The results show that the SSSC-S case presents enhanced vibration attenuation around the first resonance if compared to the SSSC-H and SSDI control circuits. In addition, the combination of the SSSC-H and SSSC-S branches would result in larger vibration attenuation than the SSDI case. It can also be observed that changes in the resonant frequency is not so evident for the hardening approach as it is for the softening case. This could be addressed to the structural stiffness being relatively high in open circuit condition such that the controlling action of the SSSC-H circuit has no greater influence when attempting to make the structure stiffer. In addition, one should also notice by analyzing the results in figure 38a that the SSDVa case leads to the largest attenuation among the cases verified in the experiments. In fact, since the controllers are acting around the structure's resonance frequency, the damping controlled techniques (SSDI and SSDVa) indeed should be more effective than stiffness controlled ones (SSSC-S and SSSC-H).

In order to verify whether the SSSC techniques would result in a better performance for a lower target frequency, an 2H inductance was selected (assuming a target frequency around 30Hz), according to the capacitance of MFC3 ( $C_{p3} \approx 15\text{nF}$ ). However, no further influence was observed on the output force (figure 38b), although the SSSC controller was able to increase the MFC3 voltage level (figure 38c), indicating the circuit was active in that bandwidth.

Another important aspect that was investigated concerns the circuitry power supply. As mentioned previously, the presented semi-active circuits required an external power supply to work properly since the electrical current provided by the piezoelectric elements



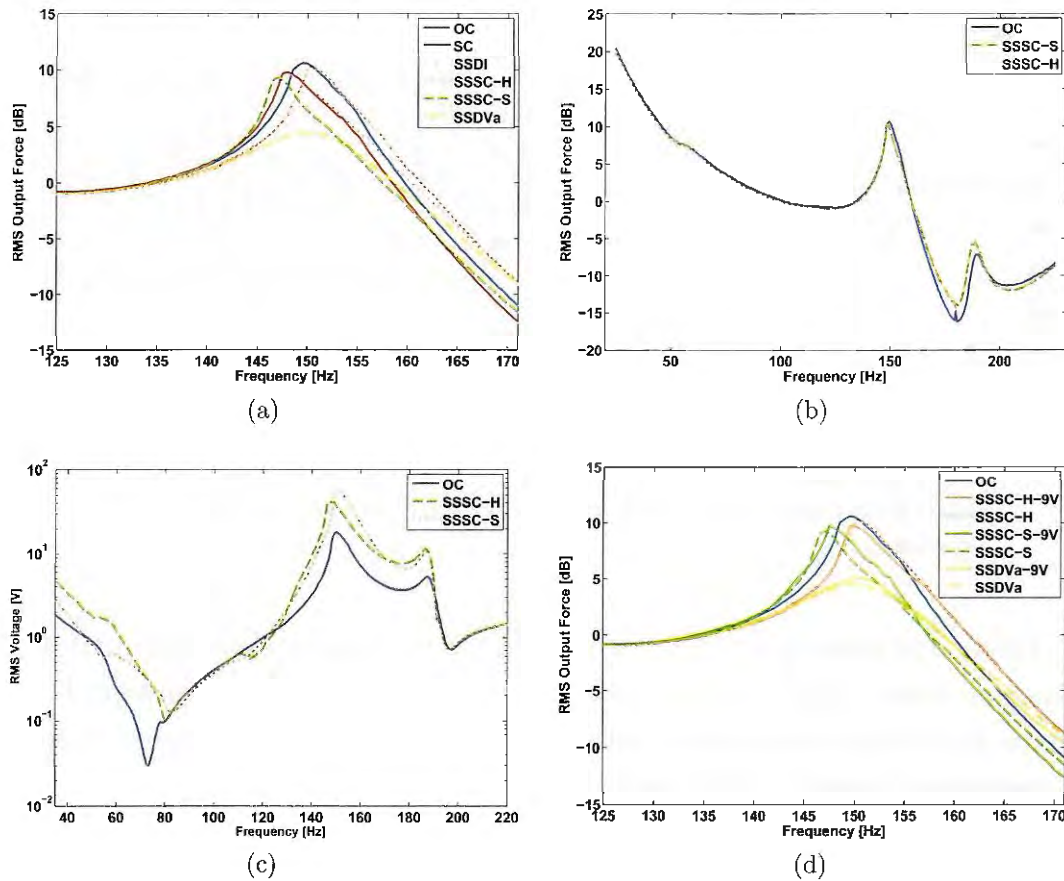


Figure 38 – (a) Effect of all controller circuits on the elementary structure when the inductor was set to attenuate vibrations of the first structural resonance frequency; (b) the effect of SSSC technique for hardening (SSSC-H) and softening (SSSC-S) cases tuned to attenuate a lower bandwidth (around 30 Hz); (c) Voltage frequency response of MFC3 (primary piezoelement) for open circuit condition and (d) frequency response of the output force when the voltage level of the external power supply was limited to 9V.

was not enough to activate the circuit. Therefore, it would be interesting if the circuit could work with a portable power supply like a 9V alkaline battery, for example. The electrical current supplied by those batteries would be enough to power the circuit as well as their size suitable for applications involving rotary-wing aircrafts.

An experimental test was performed by setting the voltage level of the DC power supply adjusted to 9V. The results (figure 38d) indicated that limiting the voltage to such level would not significantly degrade the performance of the circuits. Nevertheless, it is important to highlight that if the piezoelectric elements of the SaPPL device were able to power the controller circuit there would be no need of using external power supply and, therefore, the voltage limitation would depend only on the capacity of the piezoelectric elements. Reducing the power requirements of the control circuit and/or increasing the available electrical current produced by the piezoelectric elements would contribute to

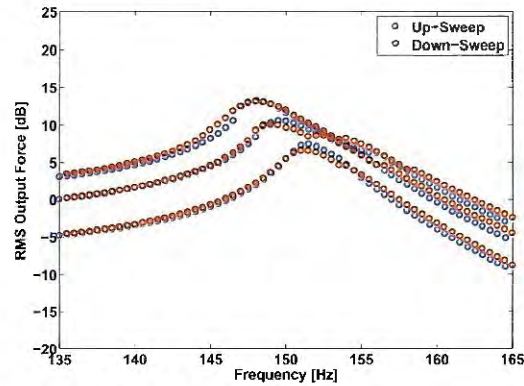


Figure 39 – Mechanical frequency response (output force) of the enlarged elementary structure for different excitation amplitudes.

mitigate (or even eliminate) the dependence on external power. In the latter situation, the available voltage would rely on the capacity of the MFC elements in convert mechanical to electrical energy and, therefore, would not be limited by an external power supply.

Finally, it is also important to note the nonlinear behavior of the system in open- or short-circuit conditions (figure 38a and figure 38d). The softening aspect observed for both electrical boundary conditions is due to the nonlinear behavior of piezoelectric materials that has been reported in the literature (LEADENHAM; ERTURK, 2015). The same softening behavior can be observed when the SSSC circuit is employed (in the hardening and softening cases). Another test was performed to verify the effects of the structure's nonlinear behavior and if additional investigations should be performed. A stepped-sine procedure was implemented for up and down sweeps and three different excitation amplitudes were also considered. The results (figure 39) show evidence of nonlinear behavior but no drastic difference has been pronounced for the up and down sweeps, as it would expect from structures with strong nonlinear characteristics. Nevertheless, no further tests were conducted on this matter.

## 5.2 Benchtop tests of the SaPPL device

The experimental tests reported in this section were performed with the prototype of the Smart Piezoelectric Pitch Link (SaPPL) device using the same benchtop setup presented in figure 36 in order to characterize its electroelastic behavior. The closed-loop procedure previously employed in the tests of the elementary structure (section 5.1.3) was also used to test the SaPPL and, although the same frequency bandwidth was considered, a continuous sinusoidal sweep (*chirp* signal) was applied in this case (considering a 0.25Hz/s frequency rate).

Figure 40 shows the SaPPL installed on the experimental setup. In such case, the bottom rod-end of the device was attached to a "L-shaped" bracket. The bracket (also

used during the APL testing procedure) mimics the connection to the swash plate of a helicopter. Strain gauges mounted on the bracket's internal surface are responsible for monitoring the load and also vibration level. However, a problem in the strain gauge circuitry (Wheatstone's bridge and other circuits required to process and amplify the strain gauges' signal during the benchtop tests) did not allow to measure the load at the bottom bracket (the strain gauge processing circuitry could not be repaired while the bench top tests were carried on in Canada). Therefore, this monitoring process occurred only for the rotational vibratory tests performed the whirl tower testing facility, which is described in the next section. Vibration attenuation measured in the bracket should be understood as reduced vibration transmission from the rotary to the fixed frame of a helicopter.

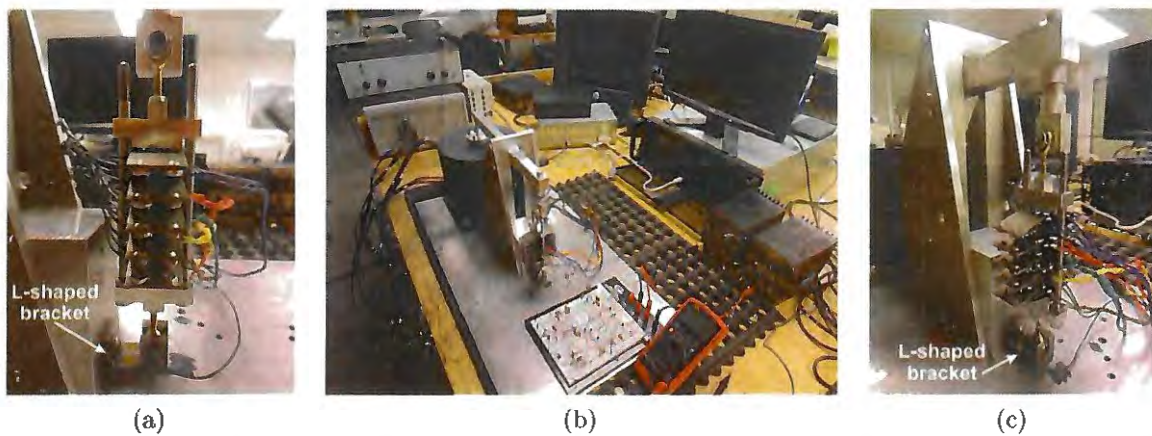


Figure 40 – SaPPL device installed on the benchtop test setup: (a) Front view, (b) general view and (c) side view.

The reduced scale 1-bladed rotor available in the whirl tower facility affected the designing process of a new pitch link in different manners. Maybe, the most significant one was due to the dimension restrictions involved. Therefore, the prototype of the SaPPL device was designed considering smaller piezoelectric elements (MFC) than those used in the enlarged elementary structure and, for that reason, each MFC element of the prototype produced a lower voltage output. However, a few of them could be connected in series to increase the overall available voltage, since the core structure comprehends 20 MFC elements. These connections reduce the number of wiring terminals of the piezoelectric elements, being helpful to properly install the device in the whirl tower facility, in special, due to the limited room available for the wiring and also the limited number of channels for data acquisition (the slip ring of Carleton's whirl tower has 8 channels). In this sense, it was necessary to select which MFC should be electrically associated to compose the piezoelectric sets in order to avoid voltage canceling issues and also guarantee an adequate voltage level was produced to power the control circuit properly.

During the dynamic benchtop tests the electromechanical structure was harmonically excited within a predefined frequency bandwidth in order to select which MFC element should be connected in series and also to choose the primary, secondary and Energy Harvesting (EH) sets. Elements with higher voltage level were grouped to compose the primary and secondary sets, which are the main piezoelectric sets of the device (the EH sets are responsible for auxiliary functions), and each combination was performed such that voltage cancellation issues were mitigated. Figure 41 shows the test results where the term "Unit" specify the elementary structure in the core structure assembly (numbered in ascending order from top to bottom in figure 22) and the MFC elements numbering system follows the same pattern of figure 17a for each elementary structure.

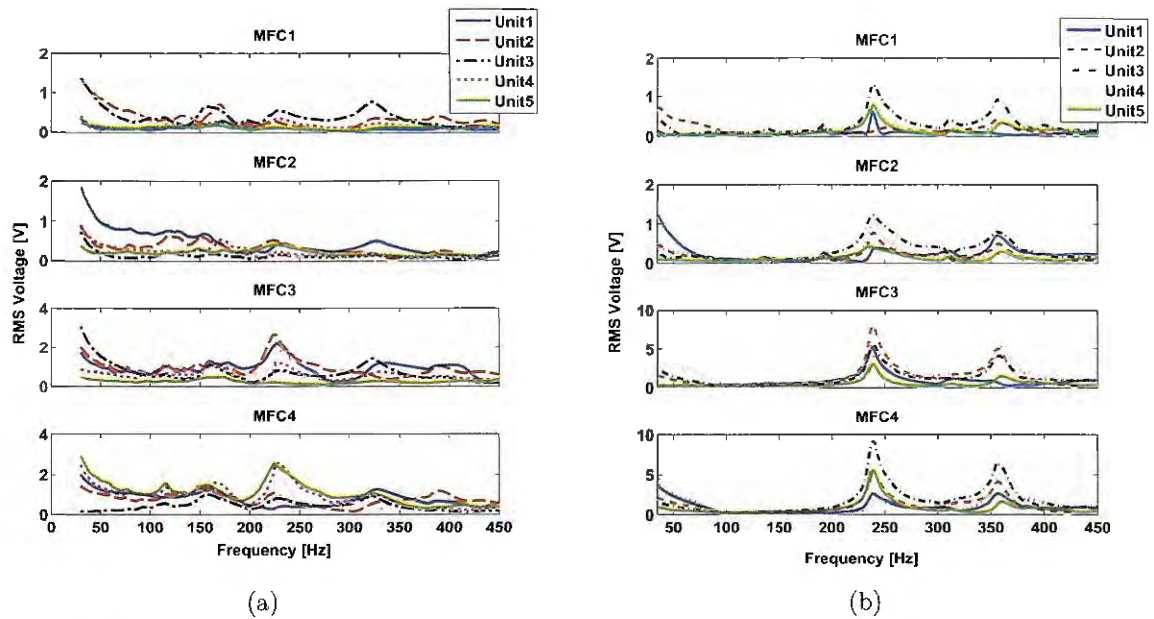


Figure 41 – Voltage frequency response of SaPPL device with (a) aluminum and (b) steel *upper handle*, considering all piezoelectric sets are in open circuit condition.

As described in section 4.2, the first prototype was initially designed with an *upper handle* part manufactured using an aluminum alloy of designation 6061-T6. However, with that configuration the structural fundamental resonance frequency (225 Hz, as depicted in figure 41a) was much higher than the target frequency the SaPPL device should aim during the whirl tower experimental tests. Hence, a low voltage level would be produced by the electromechanical device and, consequently, the circuits would not be activated. In attempt to reduce the natural frequency and, therefore, increase the electrical output of the device for a bandwidth near the target frequency, a heavier *upper handle* was designed and manufactured. In this sense, it was expected the additional mass on the top of the core structure would bring the resonance to a lower frequency. The new material selected was the AISI 1018 carbon steel and the dimensions of both parts were similar, with the steel and aluminum parts weighting 100 g and 25 g, respectively.

The results (figure 41b), however, were not as presumed, since there was no substantial change in the frequency response besides an increase in the voltage amplitude for most MFC elements, especially for MFC3 and MFC4 of all units (one shall notice the resonance peak is more evident for the new configuration). The amplitude variations could be addressed to the fact that an additional mass at the top of the device (the heavier *upper handle*, in this case) would contribute to increase the force acting on the structure but not to considerably modify the resonance frequency of the core structure. Yet, it was reasonable to keep the heavier configuration, considering that higher voltage amplitudes usually improve the performance of the control techniques employed.

Table (6) indicates the MFC elements that were chosen to form the primary (Set 1 and Set 3), secondary (Set 2 and Set 4) and Energy Harvesting (Set *EH1* to Set *EH3*) piezoelectric sets, according to the results presented in figure (41b). The "*ux-y*" codification was used to identify each MFC element of the SaPPL device (figure 22) and the term *ref.* specifies the piezoelement used as reference to calculate the phase difference.

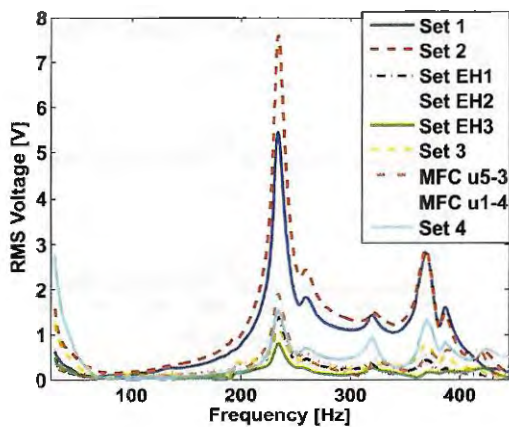


Figure 42 – Voltage frequency response of the SaPPL device with MFC elements connected in series to form the piezoelectric sets.

Table 6 – Phase shift between the MFC elements of the SaPPL device.

Set #	MFC ID	Phase angle		
		30 Hz	100 Hz	$\omega_{n1}$
Set 1	u1-3	75°	14°	2°
	u2-3	0°	-5°	-3°
	u3-3	ref.	ref.	ref.
Set 2	u2-4	2°	-6°	-6°
	u3-4	ref.	ref.	ref.
	u5-4	1°	-17°	3°
Set 3	u3-1	ref.	ref.	ref.
	u3-2	-1°	57°	170°
Set 4	u1-1	ref.	ref.	ref.
	u1-2	163°	98°	180°
Set EH1	u4-2	ref.	ref.	ref.
	u4-4	1°	-42°	-8°
Set EH2	u5-1	ref.	ref.	ref.
	u5-2	-5°	-65°	-5°
Set EH3	u4-1	1°	-53°	10°
	u4-3	ref.	ref.	ref.

The results show the phase shift between the associated piezoelectric elements for three different frequencies (including the first resonance frequency,  $\omega_{n1}$ ) and indicate that most sets would experience a significant voltage cancellation effect (except Set 1 and Set 2) if the structure operates with 100 Hz excitation frequency, for example. In this case, the device would operate with low performance since a low voltage level would be produced. It is important to point out though, that a phase shift in the vicinity of  $\pm 180^\circ$  is also suitable for a proper operation since the piezoelement terminals can be connected to each other using a reverse polarity. In this case, the  $\pm 180^\circ$  phase shift between two MFC elements would become approximately  $0^\circ$  and the voltage cancellation problem would be avoided

whether the device operates at 30 Hz or at  $\omega_{n1}$ . On the other hand, a phase difference presenting a larger deviation from the ideal values could also result in adequate operation with the penalty of deteriorating the overall performance because the combined voltage level would not be maximized<sup>4</sup>.

Figure 42 presents the voltage frequency response of the SaPPL device after connecting the MFC elements in series. It is possible to observe that, for this configuration, Set 1 and Set 2 provide the highest voltage levels (in open circuit condition) at the resonance frequency  $\omega_{n1}$ . At those amplitudes, the circuit would certainly be activated. However, for the whirl tower tests, the target frequency is located in a much lower bandwidth and the voltage amplitudes of Set 1 and Set 2 might be slightly lower in this bandwidth (the lowest frequency shown in figure 42 is 30 Hz due to restrictions of the electrodynamic shaker used in the tests). Besides, even if higher harmonics were aimed in attempt to target frequencies closer to the structural resonance frequency, the voltage levels would not increase significantly since higher harmonics usually involve lower energy transfer compared to lower harmonics. In this sense, a reasonable solution to obtain higher voltage amplitudes at lower frequencies without changing significantly the structural design would be reducing the device's stiffness (consequently, the natural frequency would also be reduced). The modifications performed in attempt to achieve this goal were investigated during the rotational experiments and are described in the following section.

A static loading test was also performed to assess the structural stiffness of the core structure and, therefore, characterize the effect of the input load on the structural displacement. Since the device did not dispose of a displacement sensor when this test was carried out, such information could provide an indirect estimate of the SaPPL's overall displacement during the whirl tower tests, thus preventing overload and/or excessive displacement that could lead to rotor instabilities. A load cell and static press were employed to perform the static test with the SaPPL device and the vertical displacement of the press was monitored by a digital micrometer with  $\pm 0.0001$  m precision. The load cell had a  $\pm 0.1$  lb precision and a maximum capacity of 350 lb. Figure 43 presents the results for a load range of 4.5 N to 111 N (1 lb to 25 lb) and indicates that the maximum displacement for the tested range is approximately  $3.5 \times 10^{-3}$  m. Since the pitch link is the mechanical part that connects the rotating blade to the fixed frame of the rotor, it is believed that a displacement outside this range could cause an unstable aeroelastic behavior of the blade, which could result in a mechanical failure (disassemble) of the SaPPL, therefore, causing a catastrophic incident depending on the rotational speed involved. Besides, according to conversations with researchers of Carleton University's rotorcraft research group, these load values are within the tested range used in the APL

---

<sup>4</sup> By adding two waves of the same frequency, the maximum amplitude condition occurs when the phase difference between both waves is  $0^\circ$ . Such phenomenon is known in the literature as constructive interference.

experiments. Hence, there was no need to exceed those values throughout the whirl tower tests.

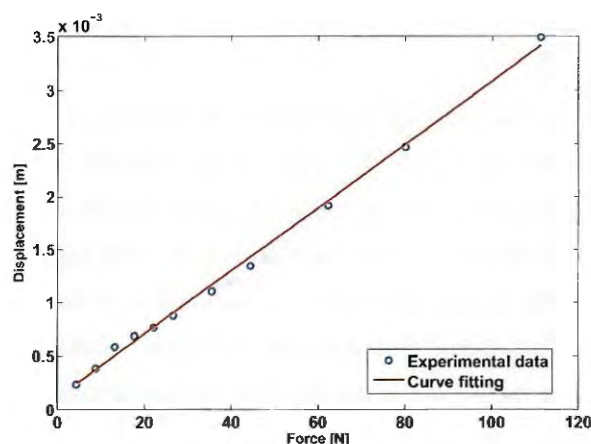


Figure 43 – Result of the static loading test performed with the core structure of the SaPPL device.

### 5.3 Whirl tower tests of the SaPPL device

The rotational tests were performed in a whirl tower facility with the purpose of investigating the performance of the SaPPL device under vibratory loads that simulate, in a laboratory environment, the vibrations experienced by a helicopter in hover flight. The facility (figure 44), located at Carleton University, houses a 60 HP, 575 V, 3 phase, 1800 RPM motor, which is controlled via a variable frequency drive/transformer (VFD). The motor, which is supported by a rigid frame, drives the rotor shaft directly with the use of an elastomeric coupling and the motor's supporting frame was designed to ensure that none of its natural frequencies are included in the operating range of the facility.

The tower was built within a 4.5 m diameter protective enclosure. The protective walls were constructed out of *Armorcore level 3* panels, a bullet resistant glass-fiber based protective panel. The facility includes operator safety features such as automatic motor shut-down in case the test chamber door is opened and emergency shut-down button available at the monitoring/control room (figure 44a). The whirl tower and surrounding area are monitored by live video surveillance to ensure safety of people and the facility integrity during operation. The motor VFD and all required power supplies are located on the exterior of the protective walls.

The facility comprises a custom 1-blade articulated hub manufactured to facilitate the installation of a pitch link prototype (figure 44b) and was designed to house a 1.1 m radius aeroelastically scaled carbon-fiber blade. This blade was designed and manufactured by the Carleton Rotorcraft Research group (FESZTY et al., 2008). An air blower supplies a vertical air stream that excites the blade around its tip and, therefore, excites the

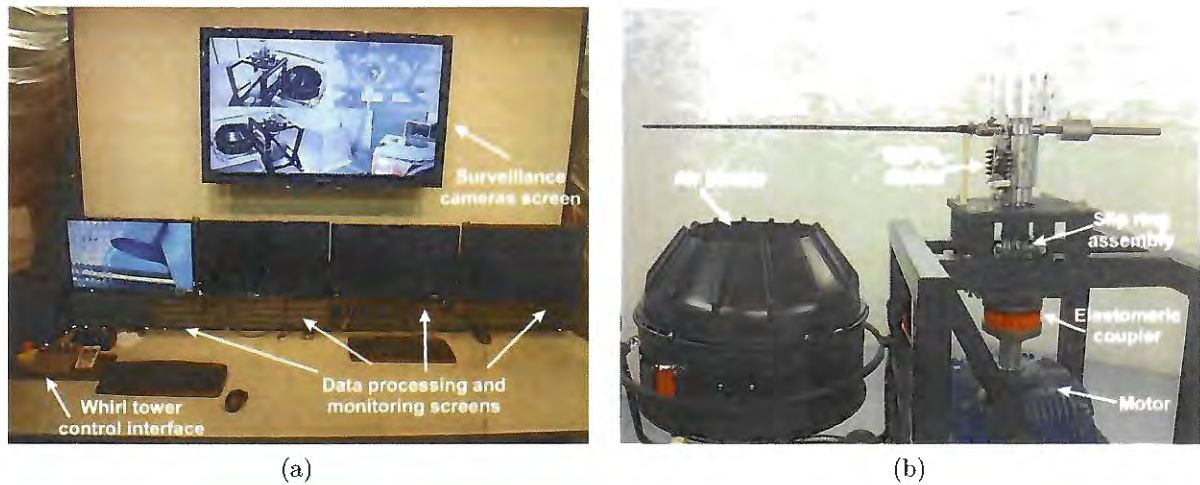


Figure 44 – The whirl tower facility of Carleton University: (a) control room and (b) test chamber.

pitch link, which is connected to the blade root through the pitch horn. The rotor hub houses both a wireless telemetry system as well as an 8 channel slip ring assembly from *Shleifring GmbH*. The wireless system consists of 2 Microstrain V-link nodes, each capable of wirelessly transmitting data from 8 differential and 8 single-ended channels.

During the whirl tower tests, the performance of the SaPPL was assessed by the load measured from the strain gauge sensors located at the "L-shaped" bracket (depicted in figure 45a). The signals obtained from the strain gauges were recorded using the available wireless Microstrain V-link nodes. Therefore, in order to start the rotational experiments it was required to estimate the calibration curve of the strain gauge sensors. For that, six different weights, which had their mass previously measured, were hung on the bracket and the signal produced by the strain gauges was recorded using a Microstrain V-link node. The result (figure 45b) shows a linear curve,  $y = 103.0x + 2026.7$ , that represents the strain gauge behavior for that load range. The linear equation was used to calculate the load acting on the pitch link during the whirl tower tests. It is also worth noting the positive sign of the recorded data, which confirms the strain gauges (located at the upper surface of the bracket) were subjected to tension stresses since the applied load was pulling the bracket downward. In other words, a compressive load applied through the pitch link produces a positive signal in the strain gauge.

In order to have a general overview of the dynamic behavior of the pitch link in terms of the load transmitted to the bracket, a rigid pitch link (figure 45a) was first tested in the facility for seven different rotational speeds that ranged from 100 RPM to 700 RPM. The data recording of each test started with the rotor in stationary condition and ended around 50s later with the rotor spinning at the nominal speed previously selected. The air blower was activated only after the rotor reached the nominal speed and was kept on until



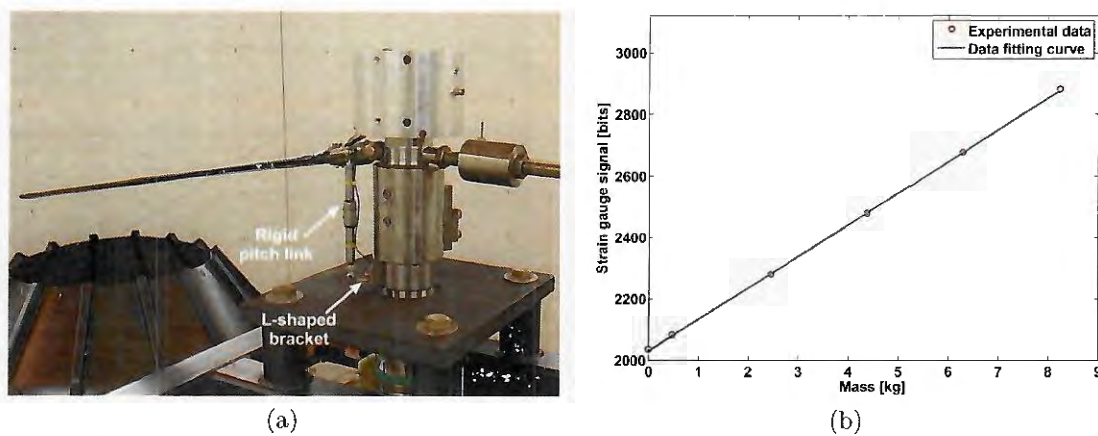


Figure 45 – Perspective view of (a) the rigid pitch link installed in the Whirl Tower facility and (b) the experimental calibration curve of the strain gauge attached on the L-shaped bracket.

the test was completed. For convenience, the pitch angle of the blade (measured at the blade root region at 0RPM) was set to  $1^\circ$  (an arbitrary value that was chosen based on information gathered from the engineers that managed the facility). Since the pitch link loads are a function of both the blade pitch angle and the rotational speed of the system, these parameters should be selected to avoid issues, such as excessive displacement and loading, when testing the SaPPL device in the whirl tower. The load results are presented in figure 46.

The results depicted in figures 46a and 46b indicate the load acting through the pitch link is the combination of a dynamic load and a mean "static" load (of compressive nature) that increases with increasing the rotational speed. According to the literature, most of the vibration transmitted through a conventional pitch link comes from the  $n/rev$  frequency and its harmonics  $pn/rev$ . In this work,  $n = 1$  considering the hub system used in the experimental tests has only one blade. Therefore, the  $1/rev$  frequency for the range of rotational speed employed is: 1.67 Hz (100 RPM), 3.33 Hz (200 RPM), 5.00 Hz (300 RPM), 6.67 Hz (400 RPM), 8.33 Hz (500 RPM), 10.00 Hz (600 RPM) and 11.67 Hz (700 RPM).

In this sense, figure 46c shows the  $1/rev$  frequency has the highest PSD amplitude for 600 and 700 RPM rotational speeds, whereas the  $2/rev$  frequency presented the highest amplitude for tests at 300, 400 and 500 RPM and, ultimately, for the 100 and 200 RPM speeds highest amplitudes occurred for the  $6/rev$  harmonic frequency. The normalized load was calculated considering the maximum amplitude for each rotational speed. Although no further investigation was carried out on that subject, it is believed that such behavior for the 100, 200, 400 and 500 RPM tests occurred due to specific dynamic characteristics of the aerolastic system composed of the rotor hub, blade and pitch link, which arises only when the system is excited at these rotational speeds. In addition, it is appropriate to

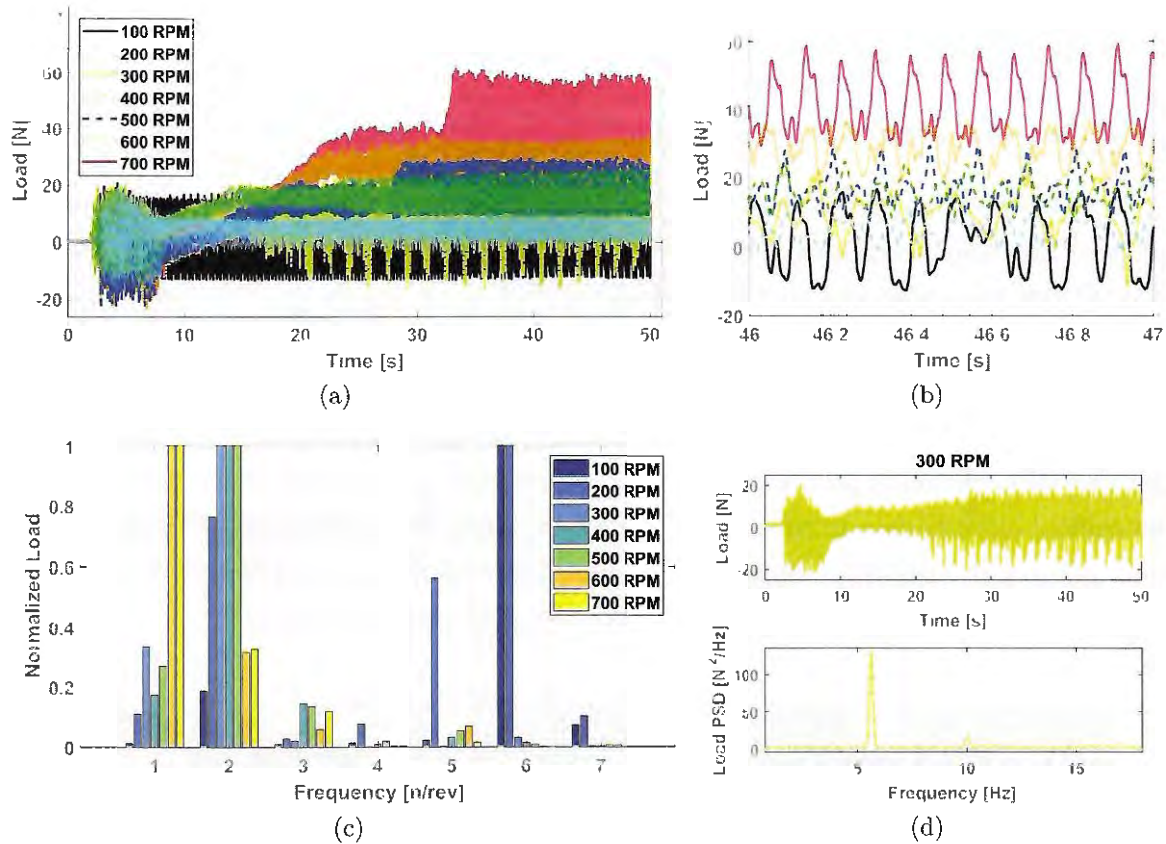


Figure 46 – Load results for the rigid pitch link spinning test showing (a) the whole time history, (b) a zoom view of the time history at nominal speed, (c) the normalized PSD signal and (d) the time and frequency results of 300 RPM.

mention that results similar to those depicted in figure 46, for the 600 RPM test, were also reported in the literature for the APL test at the same rotational speed (NITZSCHE; D'ASSUNCAO; De Marqui Jr., 2015).

Another aspect that should be notice in figure 46a and 46d is the beat phenomenon occurring for the 300 RPM test. Such behavior was not expected and occasionally appeared in some tests carried out for this rotational speed, probably, due to issues related to the re-assembling of the whirl tower in its current location (the facility was first housed in the Canadian *National Research Council* - NRC - and later moved to Carleton University). Thus, the results for 300 RPM were included in the analysis only when the effects of the beat phenomenon were less evident. Besides, one shall notice that  $1/rev$  and  $2/rev$  are the frequencies mostly mentioned along the discussions presented in this section because the first should not be affected by the control circuits and the latter, other than the  $1/rev$  (in a few cases), is the harmonic frequency with the highest amplitude. Thus, the effort was concentrated on attenuating the  $2/rev$  frequency even if this action increased the amplitudes on other higher harmonics (which are relatively less energetic than the  $2/rev$ , as indicates figure 46c). The remainder of this chapter presents the experimental tests

performed with the SaPPL device for different rotational speeds and control circuits with and without filtering capabilities.

### 5.3.1 1<sup>st</sup> series of tests: no target frequency/bandwidth defined

The whirl tower tests performed with the Smart Piezoelectric Pitch Link (figure 47) followed the same procedure of the experiments executed for the rigid pitch link, except that for this time both the load and voltage signals were monitored. The voltage signals generated by the piezoelectric sets/elements were transmitted to the controller circuits through the 8 channel slip ring since there were restrictions from the V-link input channels regarding the maximum voltage level accepted (3 V was the maximum input level accepted and the MFC elements produce higher voltage amplitudes, specially when connected to the control circuits that implement the switching techniques). The voltage signals were then monitored with an oscilloscope and recorded with a Siemens-LMS SCADAS data acquisition system, both located on the exterior of the protective walls.

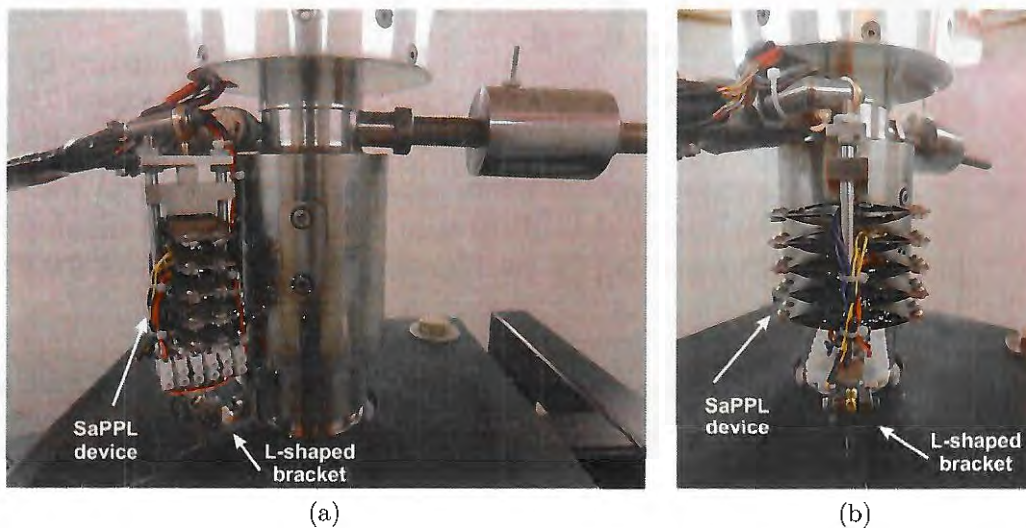


Figure 47 – Prototype of the SaPPL device installed in the whirl tower facility: (a) perspective view and (b) side view.

The initial tests occurred with all MFC sets/elements in open circuit condition and at the following rotational speeds: 300, 400, 500, 600, 700 RPM; with the blade pitch angle also set to 1 degree at the root of the blade. The load results for these cases are presented in figure 48 and indicate, as expected, the same static + dynamic loading behavior trend obtained with the rigid pitch link. However, here the increment of the static loading between each spinning ratio is more evident because the lower stiffness of the smart pitch link (compared to the rigid pitch link). Anyhow, the whirl tower experiments were proposed to investigate the performance of the SaPPL device regarding the operation of the control circuit in terms of vibration reduction. The reference condition, in this case,

was the SaPPL the piezoelectric elements/sets in the open-circuit condition. Figure 48c shows the auto Power Spectral Density (PSD) of the load signals in order to verify which frequencies have higher contribution to the overall vibratory load transmitted through the SaPPL. Here, the same behavior occurred for 300, 600 and 700 RPM test, where the  $1/rev$  frequency presented higher PSD amplitudes than the other higher harmonic frequencies, suggesting this dynamic behavior is indeed related to an intrinsic characteristic of the aeroelastic system.

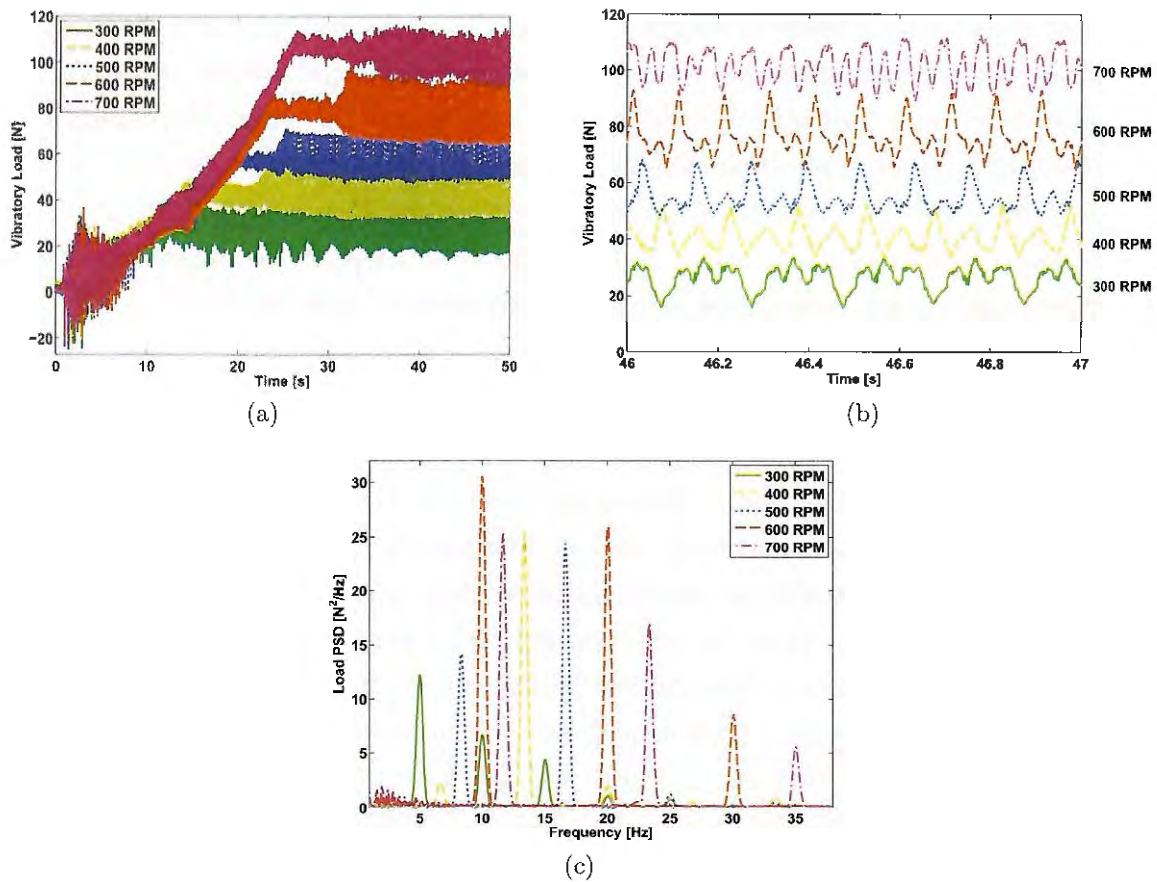


Figure 48 – Vibratory load acting on the SaPPL device for different rotational speeds: a) whole time history, (b) zoom of time history at nominal speed and (c) the auto PSD of the load signal.

Figure 49 depicts the steady state voltage time history and the auto PSD of all MFC sets in open-circuit condition, which were used to verify whether the piezoelectric sets provided enough voltage to overcome the circuit's threshold voltage. The results show that higher amplitudes were measured at different frequency bandwidths depending on the MFC set and rotational speed tested. It can also be noticed from the time history plots that Set 4 and Set *EH2* presented the highest voltage levels, with the highest contribution of those sets occurring within a bandwidth around the structure's natural frequency ( $\omega_{n1} = 237$  Hz). This confirms that tuning the structural resonance frequency to

the target frequency would be the ideal configuration to achieve high voltage amplitudes and improve the system performance.

On the other hand, despite the lower voltage amplitudes obtained, Set 1, Set 3 and MFC element u1-4 responded better in a lower frequency bandwidth: from 100 to 200 Hz for all of them and around 30 Hz for element u1-4 only. For this configuration, which might be also referenced as *stiff* configuration, all MFC sets/elements that were analyzed did not produce a voltage level high enough to activate the controller circuit. However, the *SaPPL-stiff* configuration could work properly in case the controller circuit was designed to activate with a lower threshold voltage. Considering that the MFC elements produce low current levels (the order of magnitude is  $10^{-3}$  Ampere), such modification could involve removing the current limiting resistors that are used to protect other components like transistors and operational amplifiers, for example. Such components cause a voltage drop and, therefore, reduce the voltage transferred to those components. In addition, there is the possibility of replacing the operational amplifier by another model with lower current/voltage requirements. These alternatives are detailed in section 6.1.

In attempt to reduce the structural stiffness and, consequently, the device's natural frequency, the midplate of the first (top) elementary structure was removed (i.e., u1-3 and u1-4 were removed and, consequently, Set 1 was disabled). Concerning the integrity of the whirl tower facility, the tests with this new configuration, denominated "semi-flexible"<sup>5</sup> (*SaPPL-SF1*) due to its lower stiffness, were performed only for 300 and 400 RPM since an increase in the rotational speed over this limit could cause higher displacements than those previously experienced by the stiffer configuration when tested at 700 RPM. It is important to point out that neither the hub system nor the SaPPL device disposed of a displacement sensor to check the pitch displacement at the blade root region. Therefore, for safety reasons, the *SaPPL-SF1* configuration was only tested for the lower spinning ratios. Besides, from all rotational speed tested, the device in its stiffer configuration generated higher voltage levels for 300 and 400 RPM, being reasonable to execute the tests at these lower rotations. Figure 50 shows the steady state voltage time history for the remainder piezoelectric sets that presented the highest voltage amplitudes and also indicates the voltage level generated was insufficient to activate the circuit (the threshold voltage to activate the circuit is 3 V, approximately). Yet, all voltage auto PSDs of the sets/elements tested show a peak at approximately 180 Hz, suggesting the structure's natural frequency might have been reduced to a bandwidth around this value.

Another "semi-flexible" configuration (*SaPPL-SF2*) was tested to investigate the effect of reducing even more the overall stiffness. In this case, the midplates from elementary structures 1, 3 and 5 were removed (i.e., u1-3, u1-4, u3-3, u3-4, u5-3 and u5-4). The tests

<sup>5</sup> The term "semi-flexible" was used because the flexible configuration, in this occasion, would consider the removal of midplates from all elementary structures.

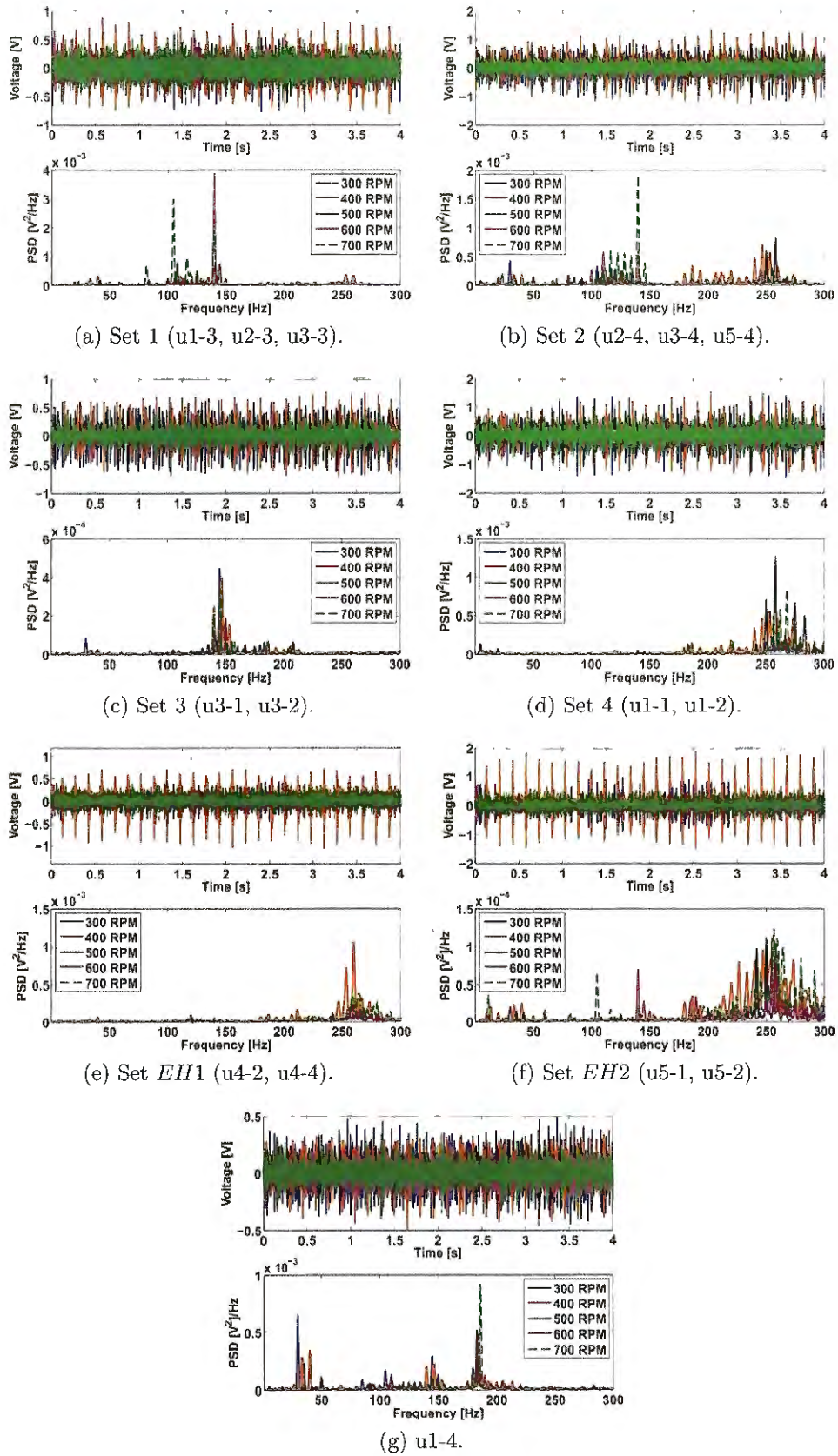


Figure 49 – Voltage time history and the respective auto PSD of *SaPPL-stiff* for all MFC sets in open circuit.

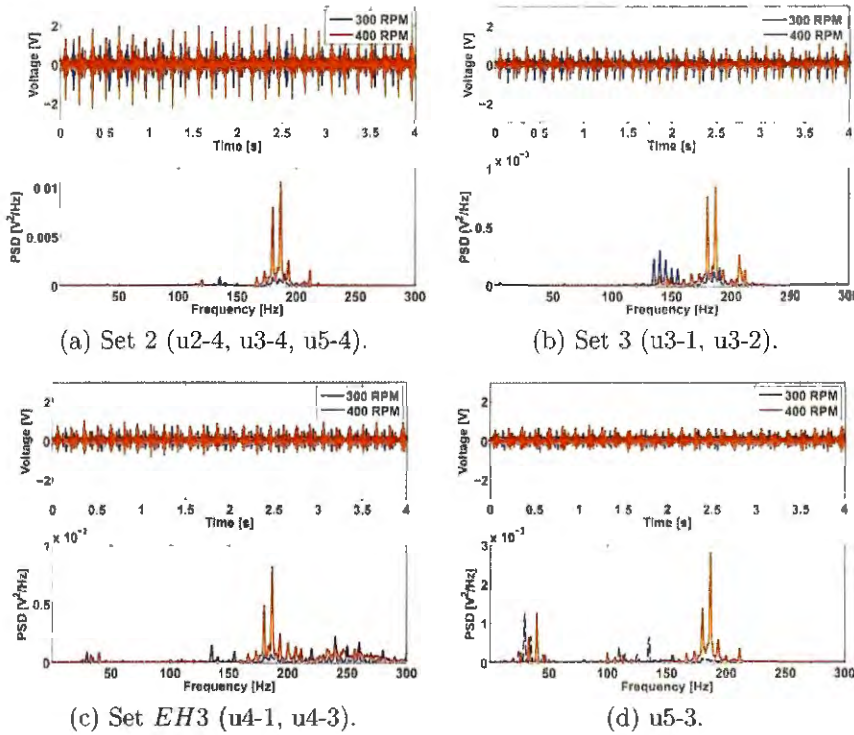


Figure 50 – Voltage time history and the respective auto PSD of *SaPPL-SF1* for all MFC sets in open circuit.

were performed only for 100, 200 and 300 RPM due to the same safety issues described before. Figure 51 shows the voltage measurements in open circuit condition and their respective auto PSD.

It is possible to observe that the voltage level obtained with Set 3 was relatively higher when compared to the voltage generated by any other set of configuration *SF2* and, therefore, would provide enough voltage to the controller circuit operate properly. Besides, all PSDs presented in figure 51 show better contribution at a bandwidth below 100 Hz (region of the spectrum that includes the  $n/rev$  frequency and its harmonics). In this sense, it was reasonable to select Set 3, Set *EH3* and Set *EH1*, respectively, as the *primary*, *secondary* and *energy harvesting* sets of the control system. A simple full-wave bridge rectifier with a  $10\mu\text{F}$  capacitor was used as EH circuit just to illustrate the working principle of the whole system. Figure 52 presents the auto Power Spectral Density of the load acting on the *SaPPL-SF2* device, comparing the performance of the controller circuits (SSDVa and SSSC) with the open-circuit case (baseline condition) for 100, 200 and 300 RPM. The auto PSDs presented in figure 52 show the effect of the SaPPL (connected to different switching circuits) on the dynamic load measured at the "L-shaped" bracket.

The results allow to conclude that the SaPPL combined to a proper switch control technique can reduce the vibration transmitted from the rotor to the fixed frame of the system. For 100 RPM, the SSDVa case resulted in significant attenuation at the first 5

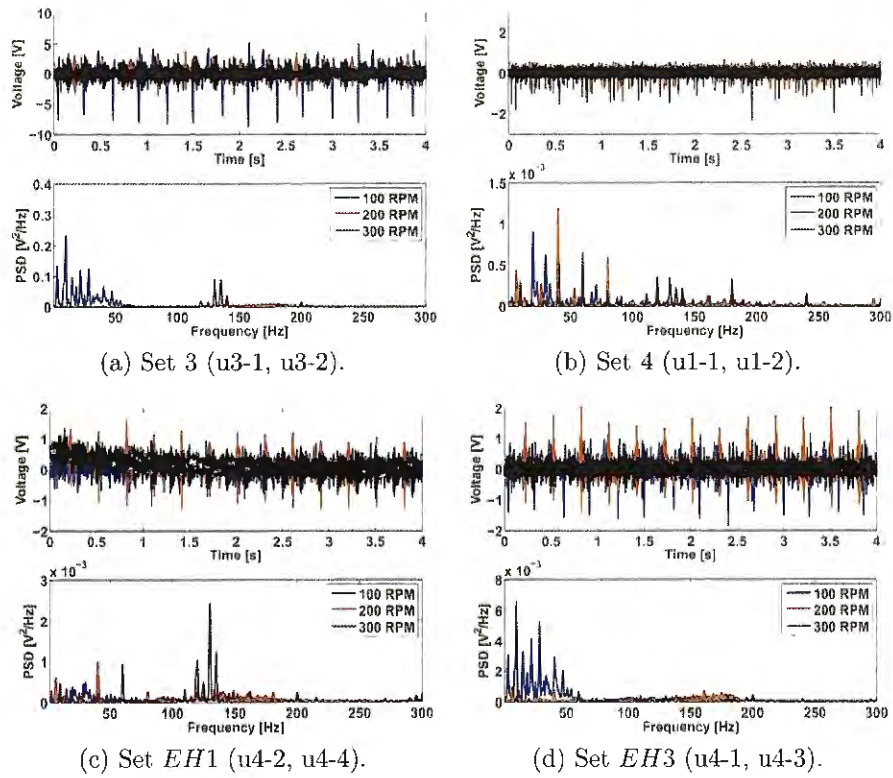


Figure 51 – Voltage time history and the respective auto PSD of *SaPPL-SF2* for all MFC sets in open circuit.

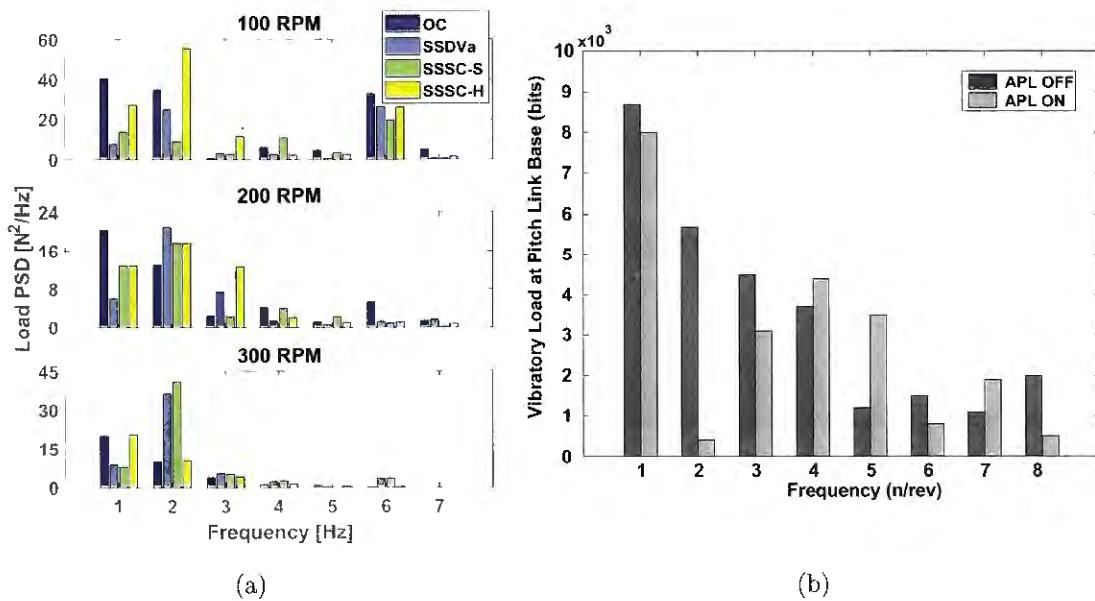


Figure 52 – (a) Effect of controller circuits on the SaPPL load spectrum (auto PSD) for the spinning rates tested and (b) the APL results for 600 RPM reported by Nitzsche, D’Assuncao and De Marqui Jr. (2015).

peaks, for example. Likewise, it is also worthwhile noting the performance of the SSSC-S case, which provided even larger attenuation for the second peak. However, it is important



to observe that, at this stage, no target frequency/bandwidth was defined. Therefore, the effects (attenuation or excitation) of the switching techniques on the  $n/rev$  frequency, as well as on its higher harmonics, were expected.

Furthermore, one might conclude that the overall performance of SSSC-S circuit for  $1/rev$  and  $2/rev$  frequencies was better than the SSDVa since the softening technique could attenuate both frequencies to approximately the same level whereas the damping technique was not so effective at the higher harmonic. However, changing the behavior of the system at the  $1/rev$  frequency is not recommended for helicopter applications because the vibration control system must not interfere with the rotor cyclic control. This problem might be overcome by tuning the controller circuit to target a specific frequency or bandwidth (in this case, frequencies above the  $2/rev$  harmonic should be attenuated) instead of letting the circuit active for the whole spectrum. One of the possible alternatives to attenuate only a specific target frequency or bandwidth involves filtering the reference voltage signal such that the switching circuit activates only at for the desired frequencies. This approach was investigated in this project and the achieved results are described in the next section.

Another interesting aspect to be observed is the excitation of some higher harmonics for all control cases. A similar behavior was experienced by the APL device according to the results (figure 52b) recently reported in the literature (NITZSCHE; D'ASSUNCAO; De Marqui Jr., 2015). In such case, the second harmonic ( $2n/rev$ ) was set as the target frequency. One should also notice that the worst performance of the SSSC-H case when compared to the SSDVa and SSSC-S.

Figure 53 shows the voltage time history of the primary set (Set 3) for 100 RPM and emphasizes the switching moments performed by the control circuits. It is possible to observe from figure 53 that a high frequency oscillation occurred for the SSSC-S case (and for SSSC-H case, in a mild fashion), which indicates that a switching operation was indeed performed<sup>6</sup> but the control circuit remained active longer than it should (a proper switch operation lasts half period of the mechanical oscillations). Besides, the SSSC-H curve shows traces of the hardening (first peak of figure 53e) and softening (last peak of figure 53e) techniques that might have affected the circuit's performance. Both behaviors could have been originated because the control techniques were not adjusted to operate with multi-harmonic excitation. Therefore, the switch operation probably occurred within a bandwidth where the phase shift between the primary and secondary sets change from  $0^\circ$  to  $\pm 180^\circ$ . Once again, this problem could be solved if the control circuit was set to perform the switch operation only at specific frequencies. Figure 54 shows the voltage time history for the secondary and EH sets, where the latter indicates a voltage level of 2 V

<sup>6</sup> The resonant RLC circuit that results from the switching operation oscillates from 10 to 50 times faster than the mechanical system

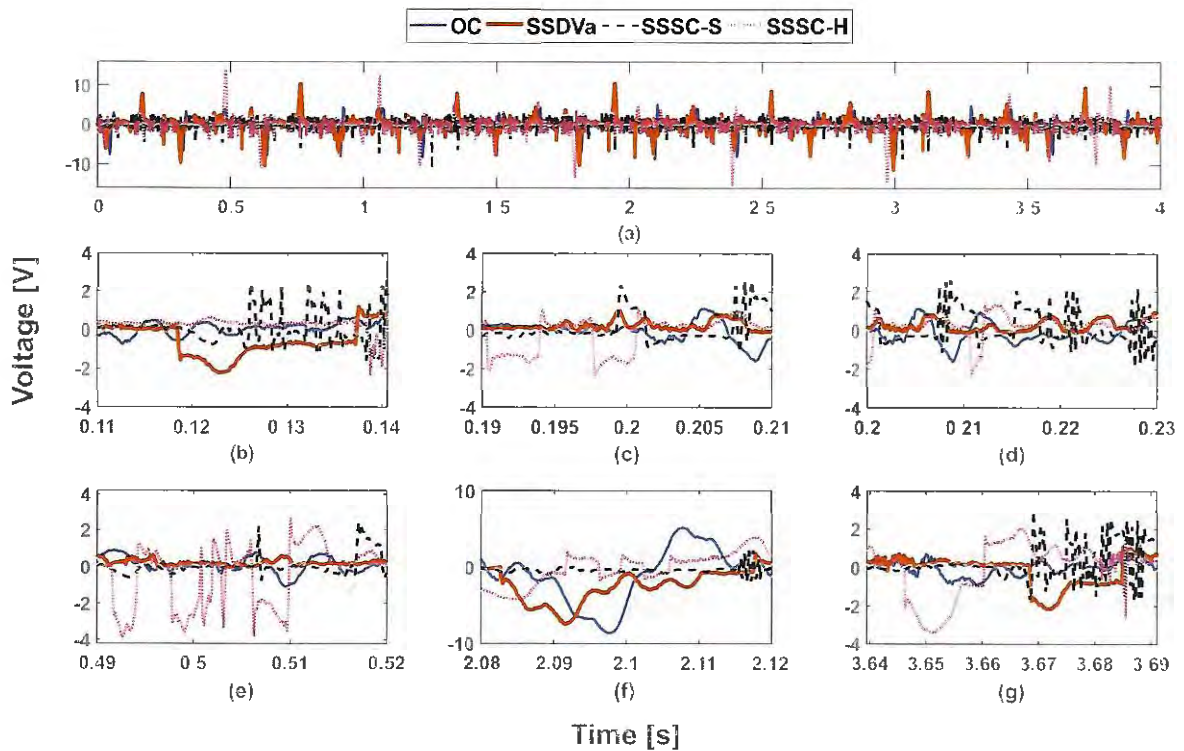


Figure 53 – Voltage time history of the primary set (Set 3), with emphasis at the switching moments, comparing the control circuits and open circuit condition for 100 RPM rotation speed.

across the capacitor of the regular full-wave bridge rectifier and a high level of ripple after the rectification that was probably caused due to the multi-harmonic characteristics of the AC input signal (regular rectifiers are designed to work with sinusoidal input signals only and multi-harmonic signals may degrade the rectifier performance).

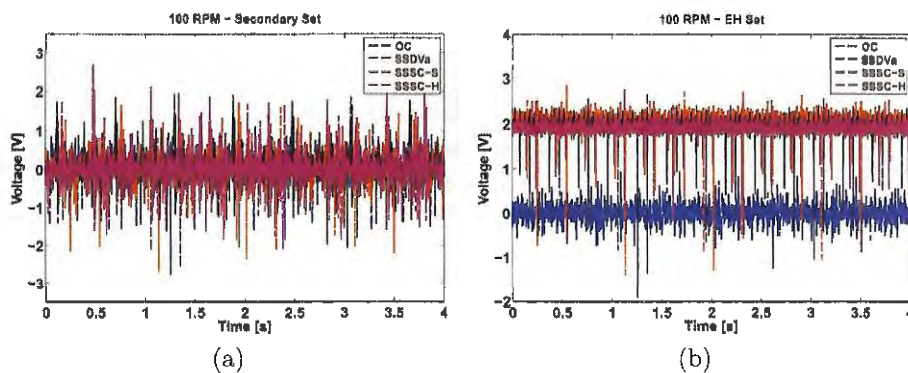


Figure 54 – Voltage time history of the (a) Secondary Set (Set *EH3*) and (b) EH Set (Set *EH1*), comparing the effects of the control circuits with the open circuit condition for 100 RPM spinning test.

5.3.2 2<sup>nd</sup> series of tests: control circuit with filtering capabilities

The tests discussed in this section were carried out to verify the performance of the SaPPL-SF2 after adjusting some characteristics of the device’s structure and circuit (described in the previous section). First, new piezoelements were chosen to compose the piezoelectric sets since the former selection criterion did not account for amplitude and phase analysis in a frequency bandwidth below 30 Hz, where the most significant control effects are expected. The new sets were grouped considering the elements that presented a similar phase difference along the analyzed bandwidth (4 – 45 Hz), with the ones that achieved the highest amplitudes being prioritized to form, in the following order, the primary (#1), secondary (#2) and energy harvesting (EH#1 and EH#2) sets, as depicted in figure 55. The MFC u1-2, for example, comprises the primary set because it produced the highest voltage amplitude and for that reason it was considered as reference to calculate the phase curve shown in figure 55a.

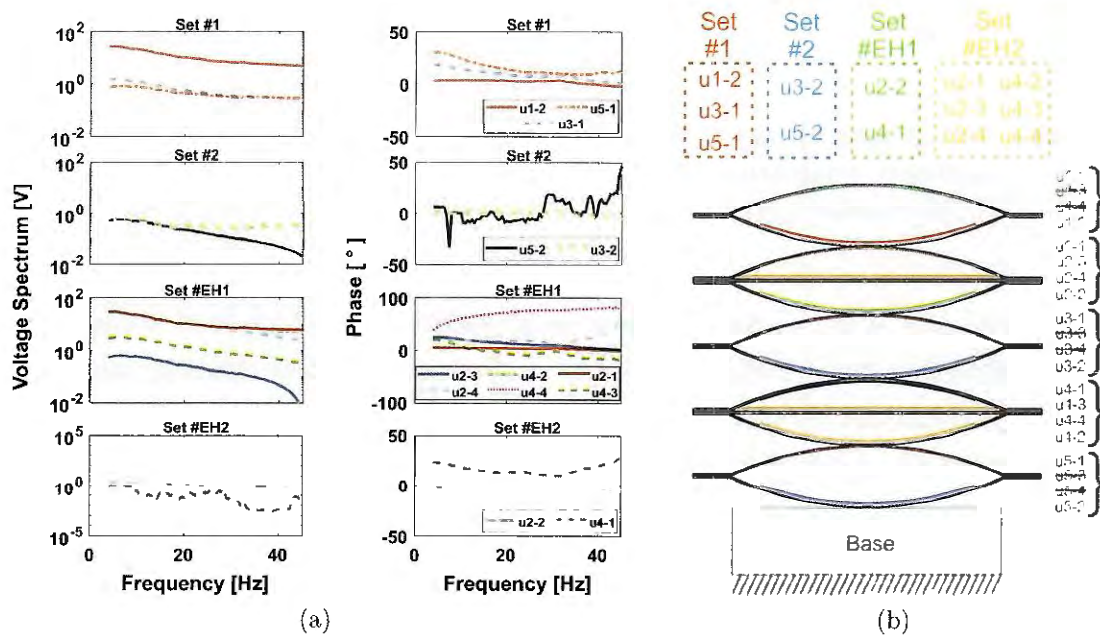


Figure 55 – (a) Magnitude and phase response of the MFC elements that compose (b) the new configuration of piezoelectric sets (u1-2 is the reference element to calculate the phase signal).

1

In addition, a non-contact Hall Effect sensor (model AD22151, manufactured by Analog Devices), here employed as displacement sensor, was attached to the device (figure 56) with the purpose of monitoring the overall displacement experienced by the upper handle part. This type of sensors provides a voltage signal proportional to the magnetic field to which is exposed, usually generated by a magnet. Thus, the closer the sensor gets to a magnet, the higher is the sensed magnetic field and, consequently, is the voltage generated. A relationship between voltage and displacement can then be established to

measure the position or displacement of a certain component. Here, an Alnico VIII magnet (model 101MG8, manufactured by Honey Well) was responsible to generate the magnetic field. However, due to noise issues that occurred during the transmission of the sensor output signal the displacement could not be monitored.

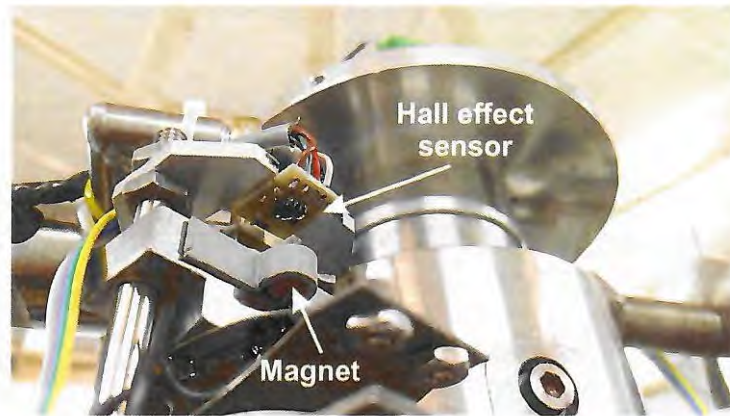


Figure 56 – (a) General view of SaPPL installed in the whirl tower with (b) emphasis in the hall effect sensor.

Another modification performed is related to the control circuit of the SaPPL device. As previously described, the nonlinear control technique employed in the first series of tests was not developed to operate under broadband vibration spectra, such as the load spectra experienced by the device in the whirl tower testing facility. In addition to a performance reduction, the pitch link device could substantially interfere with the helicopter control done at the  $1/rev$  frequency. Therefore, modifying the system to include the ability to select target frequencies could enhance the general performance (in terms of vibration attenuation and helicopter operation). In this sense, the circuit was modified to filter the voltage signal produced by the secondary piezoelectric set before transferring it to the switching sub-circuit. This way, the switching actions would only occur at the specific frequency or bandwidth previously selected and, therefore, should address the issues aforementioned.

A high pass analog filter was designed and implemented using the Sallen-key topology such that only the fundamental frequency ( $1/rev$ , for this rotor hub configuration) was included in the stop-band region. That is, the filter was specifically designed for each spinning ratio, in a way that the switching actions occurred only for the higher harmonics. Figure 57b shows the magnitude and phase responses of the analog filters, where the vertical lines indicate the pass-band frequency of each case analyzed (3, 6 and 10 Hz relative to 100, 200 and 300/350 RPM, respectively). As a common practice in the technical literature, here, the pass-band region comprehends the frequency bandwidth for which the magnitude of the filter response is greater than  $-3$  dB. In addition, it is important to point out that the filter implemented for the whirl tower tests were constructed using the

available passive electrical components that provides an approximation to the exact values obtained from the designing equations discussed in chapter 4. Therefore, the parameters of the filter implemented for the experimental tests presented a small deviation from the design parameters due to the intrinsic tolerance of each component that usually ranges from 5% to 20%, depending on the employed component.

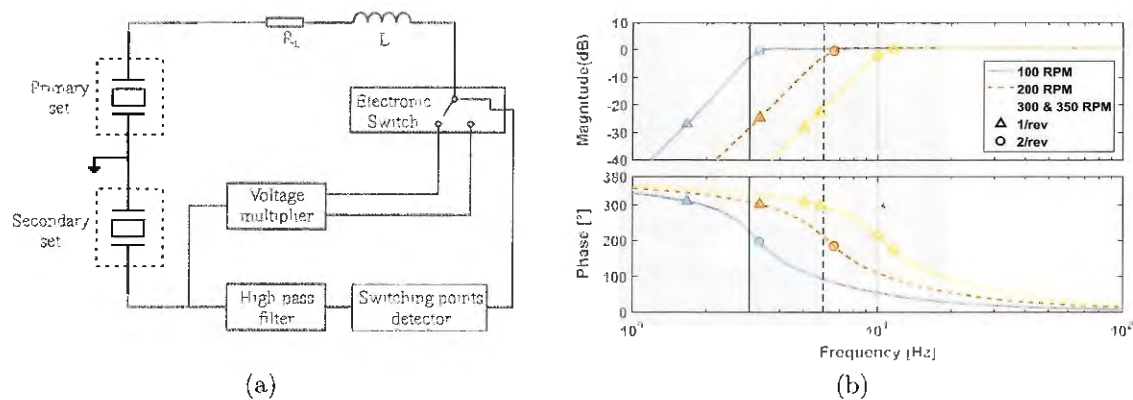


Figure 57 – (a) Block diagram of the new control circuit and (b) magnitude and phase response of the high pass analog filters designed.

The experimental tests were carried out following a procedure similar to that described in section 5.3.1, in particular with regard to the setup employed (equipment, load and voltage measurement, etc.) and the range of angular speed tested, which comprised 100 RPM, 200 RPM, 300 RPM and additionally, for this series of tests, 350 RPM. The performance of the SaPPL device was, likewise, assessed through the load estimated from the strain gauges located at the "L-shaped" bracket.

In this series of experiments the reference case (piezoelectric material in open-circuit condition) was always measured on the beginning of each test with each control circuit configuration. Here, three tests were carried out for the same condition (i.e., a combination of rotation speed and type of circuit) and every test was executed according to the following procedure: the test recording started ( $t = 0s$ ) with the rotor system in stationary condition and the piezoelectric sets of the SaPPL device connected to the data acquisition system<sup>7</sup>, i.e., the control circuit was not active; the rotor hub started spinning right after the recording command was executed and the air blower was activated 15 seconds after the recording started, being the circuit in the OFF condition (open circuit or reference condition) for 60s, approximately; afterwards the control circuit was connected to the piezoelectric sets and kept on until the test was concluded. For the analysis purposes, it was assumed the open circuit condition started at  $t = 24s$  and ended at  $t = 59s$ . The time frame of 35 seconds was considered for both electrical conditions (with the switching circuit on and off) avoiding the transition periods during the connection of the circuit,

<sup>7</sup> The impedance of the input channel ranges approximately from 10 M $\Omega$  to 20 M $\Omega$ .

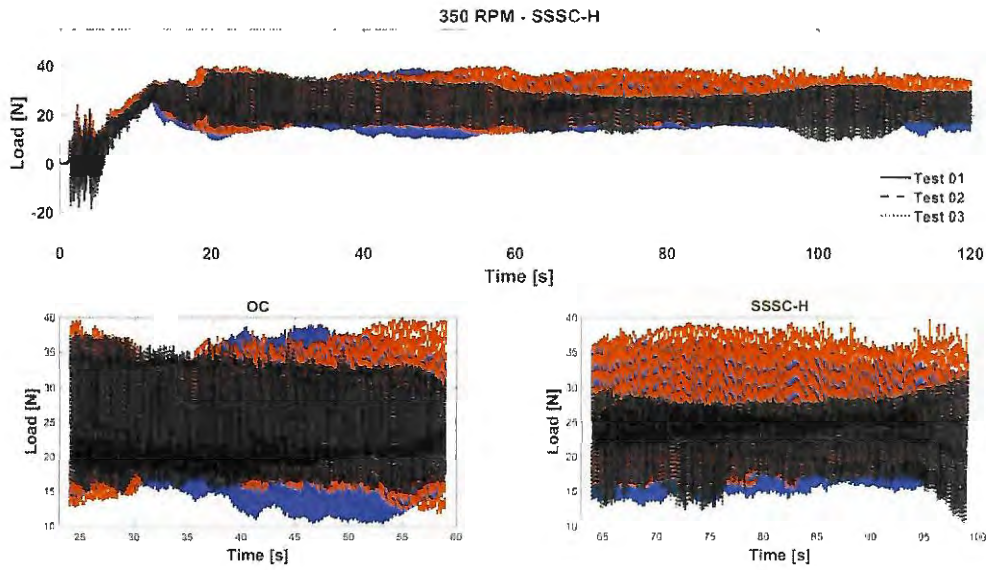


Figure 58 – Load time history of all tests performed with the SSSC-H circuit (without the analog filter) for the 350 RPM spinning test.

since it was manually connected to the piezoelectric sets using jumper wires. Figure 58 shows three time series of the load data recorded for the SSSC-S test at 100 RPM and illustrates the time window used to estimate the PSD signals during the analysis.

Because all time series depicted in figure 58 were obtained for the same angular speed and circuit (although in different tests), it was expected that the recorded data behaved in a similar fashion. However, the difference between the results of "Test 03" and the two other tests is very evident, being clear that distinct amplitude fluctuations occurred. There may be different reasons for the insufficient repeatability during the experiments such as the uncertainty involved in setting the same initial condition to all tests since the blade was manually positioned by the operator. Anyhow, those conditions could not be controlled during the tests and for this reason the present dissertation does not include any discussion on this matter. Other investigations should be carried out in order to better understand this behavior and other variables should also be monitored, as it is suggested in the following chapter.

In attempt to perform an adequate comparison for every test setup, the reference case of the analysis presented in this section is related to the  $1/rev$  frequency, for each rotation speed and with the piezoelectric sets in open circuit condition. Thus, a normalized load,

$$F_{norm} = \frac{F_{n/rev}^{ON}}{F_{1/rev}^{OFF}}, \quad (5.1)$$

was calculated to compare the performance of the SaPPL in all cases discussed, where  $F_{n/rev}^{ON}$  is the amplitude of the auto PSD of the force signal (measured at the bracket)

relative to the  $n$ th harmonic frequency analyzed when the control circuit was active and  $F_{1/rev}^{OFF}$  is the amplitude of the auto PSD of the force at the fundamental harmonic frequency with no control action. Hence, the comparison between the results obtained from both ON and OFF conditions of the control circuit occurred considering the data recorded in the same test, unlike the tests discussed in section 5.3.1, which compared results obtained from different spinning tests.

Due to the new piezoelectric sets selected to form the SF2 configuration in this series of tests, first, it was necessary to assess the performance of the SaPPL device without the filtering ability of the control circuits. Figure 59 shows the normalized load for all three tests performed in each condition (speed + circuit) except for the 300 RPM case, which exhibited the beat phenomenon that was already reported. For that spinning ratio, only the curves with minor evidence of such phenomenon were presented.

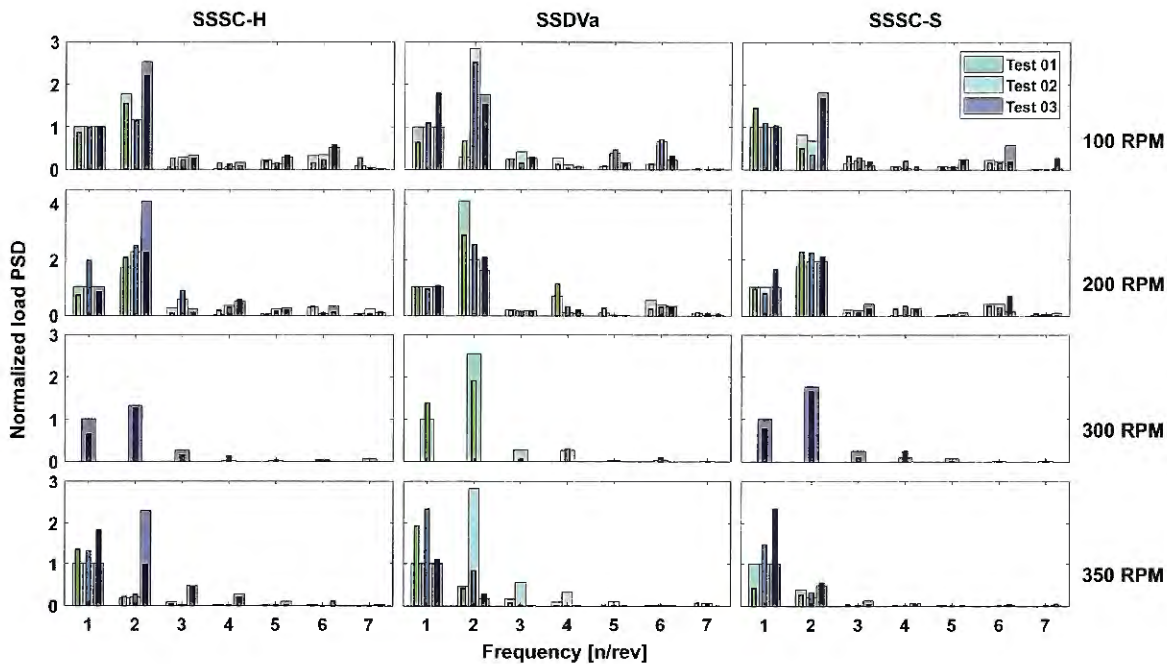


Figure 59 – Normalized load comparing the performance of the SaPPL device without the filtering ability (the wider bars represent the OFF circuit condition and the narrower bars represent the ON condition).

The results (figure 59) indicate that, for most cases analyzed, there were at least two tests presenting consistent amplitude levels and most of them showed amplitude variations in the  $1/rev$  frequency comparing the ON and OFF circuit conditions. Besides, one should notice that even for the tests where there was an effect (increase or decrease) on the amplitude of the first harmonic, the control circuits were able to provide lower amplitudes at the  $2/rev$  (as well as at other higher harmonics, in some cases) frequency compared to the condition where the circuit was off, which indicates the control circuit had a positive influence on the load transferred through the pitch link. Figure 60 displays

the auto PSD of voltage output with circuit OFF and circuit ON conditions (for each control circuit) and different speeds. Voltage output is always larger for the switching cases than the open-circuit condition.

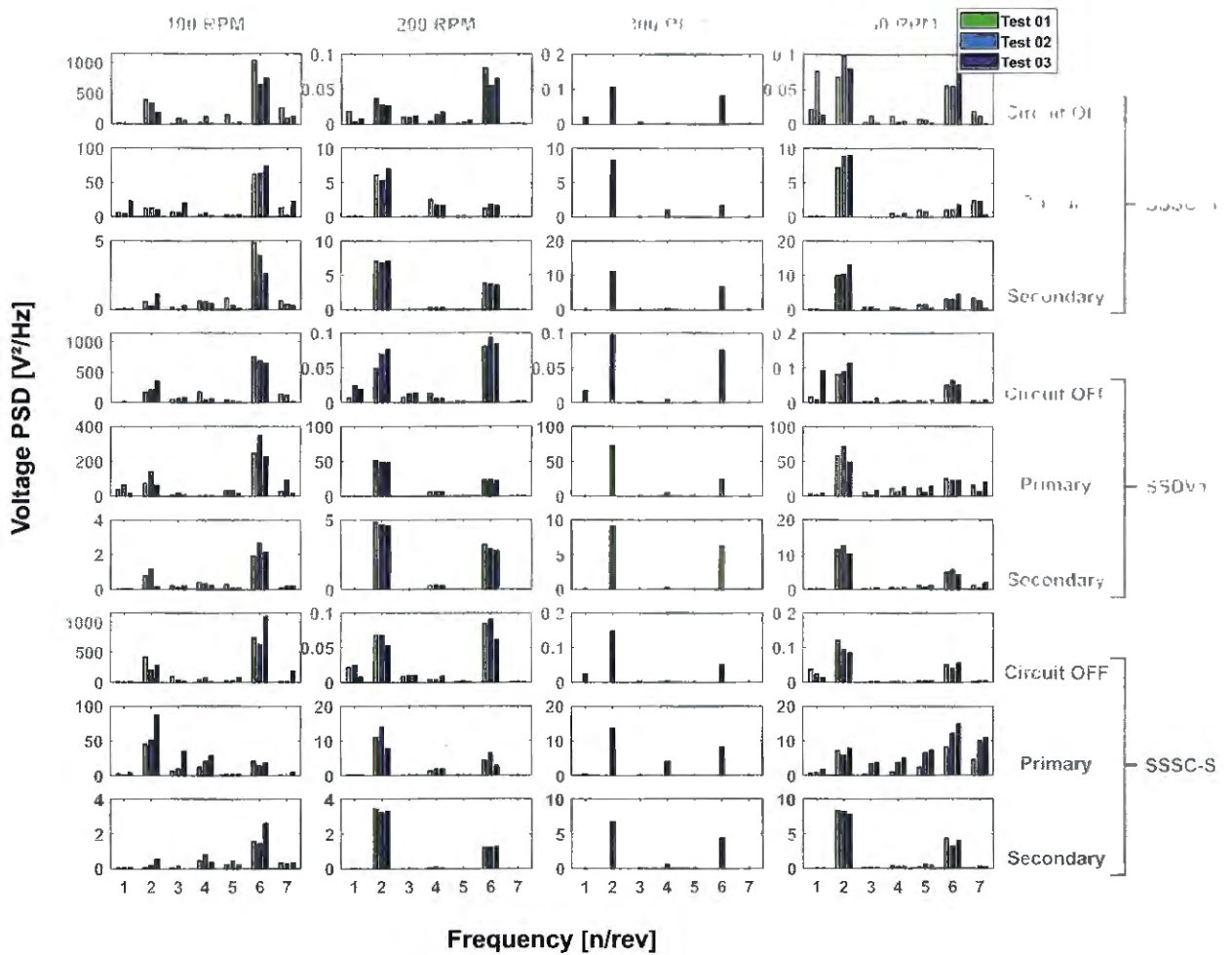


Figure 60 – Voltage PSD of the signal generated by the primary and secondary sets without the filtering ability.

Figure 61 shows the normalized load of all control circuits, considering the tests that exhibited an adequate performance with respect of the circuit’s ability in filtering the  $1/rev$  frequency. One should note in figure 61 that the first harmonic remained unchanged for most control cases and speeds (except for 350 RPM). Even in cases where the first harmonic was excited, it is possible to observe that the effect (excitation) on this first harmonic is in general lower than that observed in figure 59 (without filter). Moreover, vibration attenuation of the second harmonic is also observed for different techniques and speeds, although excitation is also observed in some cases (lower than the case without filter).

Figure 62 shows the voltage PSD of the primary and secondary sets and indicates the analog filter did work properly in every case because there was no evidence of any



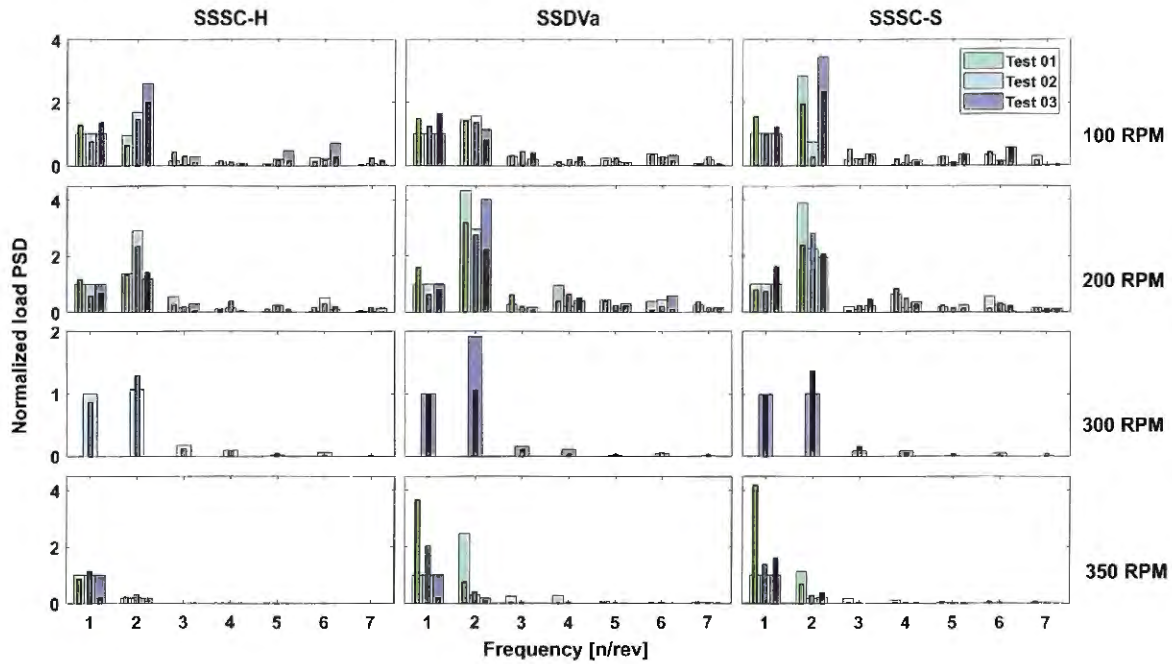


Figure 61 – Normalized load comparing the performance of the SaPPL device influenced by the filtering process (the wider bars represent the OFF circuit condition and the narrower bars represent the ON condition).

significant peak at the  $1/rev$  frequency, for both sets in all cases. In fact, this might also suggest that the changes observed in the fundamental harmonic were not directly caused by the control circuit but perhaps were consequence of the switching actions on other harmonics that modified the behavior of the whole aeroelastic system. It is interesting to note, however, that the voltage amplitudes of the  $1/rev$  frequency for the non-filtering cases is already low, compared to the  $2/rev$  (or even the  $6/rev$  with the circuit OFF).

#### 5.4 Final Remarks

This chapter presented the experimental tests carried out during the development of the SaPPL device. Benchmark vibratory tests were performed to investigate the static and dynamic behavior of the electromechanical structure of the SaPPL device. Whirl tower experiments were carried out for different rotational speeds and the ability of the device in reduce the vibration transmitted through its body was assessed for the SSDVa and SSSC control techniques. An analog high-pass filter was included in the topology of the control circuit in attempt to avoid affecting the fundamental harmonic ( $1/rev$ ), when the control was activated, for every spinning ratio tested and, therefore, attenuate vibrations only of higher harmonics. The tests demonstrated the ability of the Smart Piezoelectric Pitch Link device in attenuate, for an specific rotational speed, the vibration transmitted from the rotating frame to the fixed frame of the system.

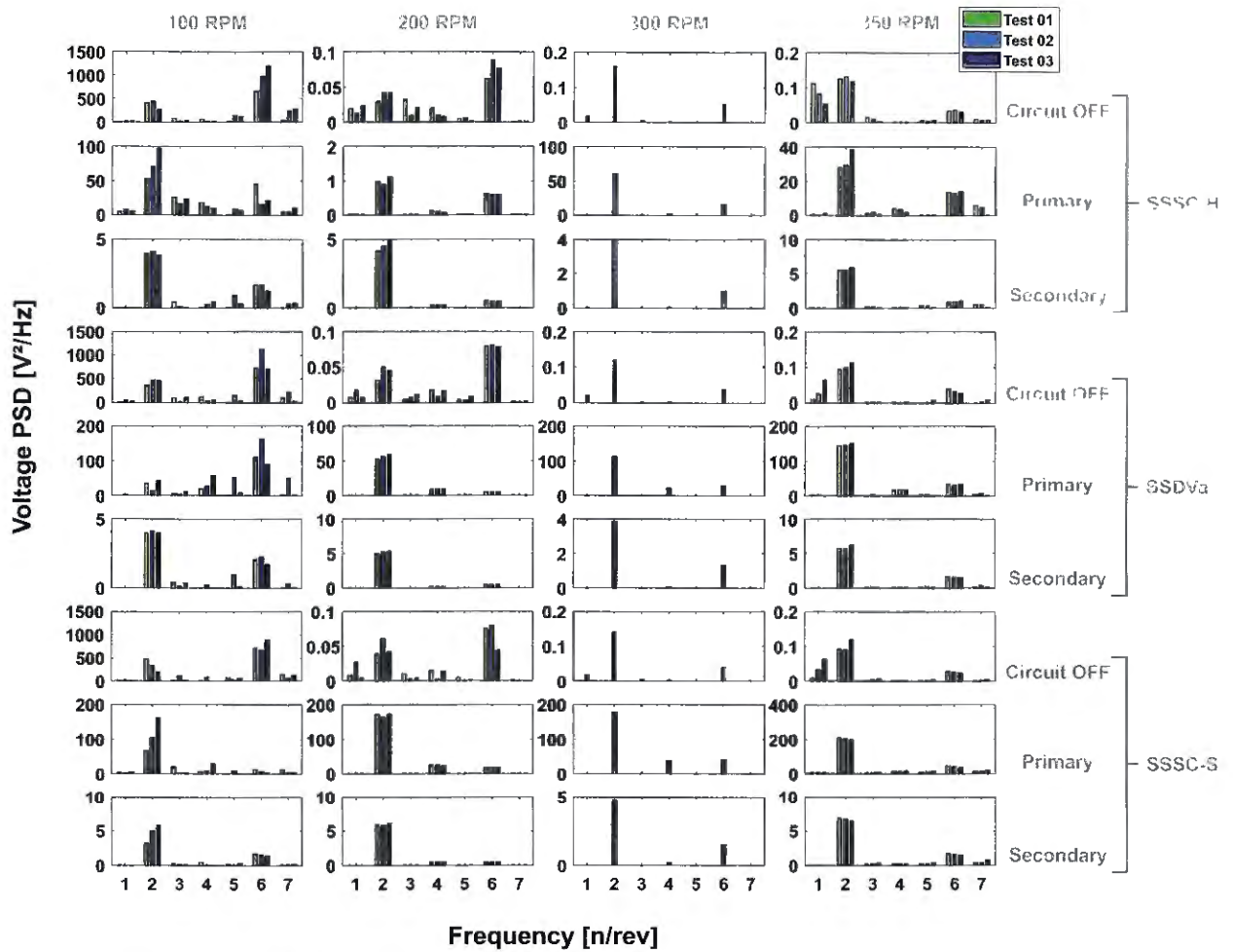


Figure 62 – Voltage PSD of the signal generated by the primary and secondary sets influenced by the filtering process.



## 6 FINAL REMARKS

This dissertation described the development of activities carried out during the PhD research, which the main objective was to develop the concept of a Smart Piezoelectric Pitch Link (SaPPL) that could attenuate the vibrations transmitted to the fixed frame of helicopters. The topics discussed include a literature review, which focused on piezoelectric-based vibration control systems, and a procedure to model an electromechanical piezoelectric structure connected to a control circuit in order to represent and simulate a system that is capable of performing vibration reduction and/or energy harvesting. Such procedure was verified against a bimorph electromechanical beam and the achieved results were satisfactory. However, the simulations with the SaPPL device were not carried out as planned and the research project remained essentially experimental.

A prototype of the elementary structure (enlarged version) of the SaPPL was designed using the software ABAQUS and experimentally tested in benchtop setups for different control circuits. This investigation was very important to characterize the behavior of the device's elementary structure when it was connected to the control circuits. The results indicated how to proceed with the selection of the primary and secondary sets of the device and also confirmed the better performance of the SSDVa controller circuit when operating around the structural resonance frequency.

The first complete prototype of the SaPPL device was designed, manufactured and experimentally tested in benchtop setup and whirl tower facility to explore the device's capability of reducing vibrations considering different non-linear switching circuits (SSDVa and SSSC). The current design of the SaPPL was developed, mainly, with concern for its dimensions and structural integrity, since the installation of a pitch link in the whirl tower hub system was very restricted in terms of space and mass. The first, limits the device's overall size and, consequently, its capacity of housing piezoelectric elements able to convert a greater amount of (mechanical to electrical) energy. The latter, influences the hub balancing and also changes the effect of the centrifugal load acting on the device, which is higher as the mass increases. From the vibration perspective, these restrictions come with a trade-off regarding the resonance frequencies because the smaller the elementary structure the higher is the natural frequency. Therefore, it is more difficult to tune the SaPPL resonance frequency with the frequency targeted for the vibration reduction (which is usually less than 50 Hz). In spite of that fact, the device exhibited good performance in the frequency bandwidth below 50 Hz, in special, due to the combination of piezoelectric elements in the complete version of the SaPPL.

The stacked configuration of the core structure allowed to connect several MFC elements to form the controlling sets (primary and secondary), which were selected as result

of the benchtop tests performed with the SaPPL device. Furthermore, these tests were also useful to define the load range for testing the device in the whirl tower facility since the flexible core structure could experience displacement levels that could compromise the facility integrity. The SaPPL device was experimentally tested in the whirl tower facility regarding different spinning ratios and control circuits. Three structural configurations were tested (**stiff**, **SF1** and **SF2**) in attempt to achieve voltage levels required to activate the control circuits, which were adjusted to stiffness and damping switching techniques.

Two series of whirl tower tests were carried out, one with no limitations regarding the control action of the switching techniques and another including an analog high-pass filter in the circuit's topology in attempt to avoid affecting the fundamental harmonic ( $1/rev$ ) for every spinning ratio tested and, therefore, attenuate vibrations only of higher harmonics. The results indicated that when the circuit was active, the vibration amplitudes at higher harmonic frequencies (specially at  $2/rev$ ) were lower than the amplitudes without control action for most part of the cases analyzed. However, since the conventional SSSC and SSDVa control circuits were not designed to operate with multi-harmonic signals, there were a few issues related to the switching operations that could have compromised the overall performance of the system. Despite the issues occurred during the experiments, the results demonstrated the ability of the smart pitch link device in attenuate, for an specific rotational speed, the vibration transmitted from the rotating frame to the fixed frame of the system.

It is also important to mention that the current version of the control circuit is not self-sufficient and, thus, can not be exclusively powered by the piezoelectric sets. The possibility of reducing the power requirement of the electronic components and use a rechargeable battery as power supply should be better investigated in attempt to overcome that problem. Likewise, a series of modifications of both the structure and circuit must occur so that a newer version of the SaPPL device can be developed. The following section discuss the future perspectives for the Smart Piezoelectric Pitch Link device, suggesting several aspects that could be further investigated.

## 6.1 Future work

Based on the matter discussed in this dissertation, this section describes the main aspects and recommendations for further investigations on the line of research here presented.

- Investigate how the number of elementary structures and piezoelectric elements affects the overall performance of the device. It is important to determine whether the SaPPL device could work with a reduced number of elementary structures and piezoelectric elements without considerably reducing its performance. Such tests could

help to select alternatives for adjusting the structural stiffness and, consequently, produce higher electrical response for low target frequencies or bandwidth;

- Investigate the effect of pre-compressing the core structure and how this modification affects the performance of the device. As it could be noticed from the preliminary results, the load acting through the SaPPL device is strongly influenced by the rotational speed. Hence, understanding the effect of pre-compressing the core structure is essential to select which operational condition would result in a better performance of the SaPPL device for vibration attenuation;
- Modify the control circuit to reduce its power requirements and test the possibility of using a portable battery as power supply. Such task would approximate the SaPPL device of a self-sufficient condition, since a portable power supply might be placed in the vicinity of the core structure, inside the SaPPL structural housing;
- Verify the use of digital filter instead of the analog implementation. Such improvement could increase the versatility of the device in terms of filtering ability. In this sense, different types of filter could be implemented in a single micro-controller chip and activated accordingly, whereas the filter parameters could be adjusted with tighter tolerances, giving more control during the designing process;
- Verify the performance of the SaPPL device regarding different control techniques. Linear resonant circuits, for example, could be tuned to target different frequencies since the device disposes of several piezoelectric elements. In addition, the recent development of digital shunt circuits introduces the possibility of employing compact electronic circuits with self-tuning characteristics that could be robust to variations of the rotational speed, for example;
- Develop a new design for the device considering aspects such as compactness, fail-safe characteristics, aerodynamics, etc. and also include sensors to monitor the integrity and electromechanical behavior of the core structure.
- Explore the energy harvesting capacity of the SaPPL by testing different EH circuits;
- Investigate the possibility of employing the SaPPL device as a vibration isolator.



## REFERENCES

- AASHTO. **Standard Test Methods for Tension Testing of Metallic Materials**. 2013. 1–27 p.
- ABAQUS. **Documentation**. Pawtucket: Hibbitt, Karlsson & Sorensen. [S.l.], 2010.
- ALLIK, H.; HUGHES, T. J. R. Finite element method for piezoelectric vibration. **International Journal for Numerical Methods in Engineering**, v. 2, n. 2, p. 151–157, apr 1970. ISSN 0029-5981.
- ANUSONTI-INTHRA, P.; GANDHI, F. **Helicopter Vibration Reduction through Cyclic Variations in Rotor Blade Root Stiffness**. 2000. 153–166 p.
- \_\_\_\_\_. Optimal control of helicopter vibration through cyclic variations in blade root. **Smart Materials and Structures**, v. 10, n. 1, p. 86–95, 2001. ISSN 0964-1726.
- ARNOLD, U.; STRECKER, G. Certification. Ground and Flight Testing of an Experimental IBC System for the CH-53G Helicopter. In: **In Proc. of the 58th Annual Forum of the American Helicopter Society**. [S.l.: s.n.], 2002. p. 58(Part I): 297–308.
- ARNOLD, U. T. P.; FUERST, D. In-flight tuning system for the CH-53G Helicopter. In: **AHS 67th International Annual Forum**. Virginia Beach, VA: [s.n.], 2015.
- AUSTRUY, J. **Rotor Hub Vibration and Blade Loads Reduction , and Energy Harvesting Via Embedded Radial Oscillator**. 2011. 195 p. Tese (PhD Dissertation) — The Pennsylvania State University, 2011.
- BADEL, a.; LAGACHE, M.; GUYOMAR, D.; LEFEUVRE, E.; RICHARD, C. Finite Element and Simple Lumped Modeling for Flexural Nonlinear Semi-passive Damping. **Journal of Intelligent Material Systems and Structures**, v. 18, n. 7, p. 727–742, feb 2007. ISSN 1045-389X.
- BADEL, a.; SEBALD, G.; GUYOMAR, D.; LALLART, M.; LEFEUVRE, E.; RICHARD, C.; QIU, J. Piezoelectric vibration control by synchronized switching on adaptive voltage sources: Towards wideband semi-active damping. **The Journal of the Acoustical Society of America**, v. 119, n. 5, p. 2815, 2006. ISSN 00014966.
- BARRET, R. **Intelligent rotor blade and structures using directionally attached piezoelectric crystals**. 1990. Tese (MS Thesis) — University of Maryland, 1990.
- BATHE, K. **Finite Element Procedures in Engineering Analysis**. [S.l.]: Prentice-Hall, 1982.
- BEEBY, S. P.; TUDOR, M. J.; WHITE, N. M. Energy harvesting vibration sources for microsystems applications. **Measurement Science and Technology**, v. 17, n. 12, p. R175–R195, dec 2006. ISSN 0957-0233.
- BHATTI, M. A. **Fundamental Finite Element Analysis and Applications: With Mathematica and Matlab Computations**. Hoboken, New Jersey, EUA: John Wiley & Sons, Inc., 2005.



- CESNIK, C. E. S.; SHIN, S. On the modeling of integrally actuated helicopter blades. **International Journal of Solids and Structures**, v. 38, n. 10-13, p. 1765–1789, 2001. ISSN 00207683.
- CHEN, S.-N.; WANG, G.-J.; CHIEN, M.-C. Analytical modeling of piezoelectric vibration-induced micro power generator. **Mechatronics**, v. 16, n. 7, p. 379–387, sep 2006. ISSN 09574158.
- CHEN, Y.-Y.; VASIC, D.; COSTA, F.; LEE, C.-K.; WU, W.-J. Self-powered semi-passive piezoelectric structural damping based on zero-velocity crossing detection. **Smart Materials and Structures**, v. 22, n. 2, p. 025029, feb 2013. ISSN 0964-1726.
- CHOPRA, I. **Smart structures technology: innovations and applications to rotorcraft systems**. [S.l.], 1992.
- CLARK, W. W. State-switched piezoelectric systems for vibration control. **Collection of Technical Papers - AIAA/ASME/ASCE/AHS/ASC Structures, Structural Dynamics and Materials Conference**, v. 4, n. c, p. 2623–2629, 1999. ISSN 02734508.
- \_\_\_\_\_. Vibration Control with State-Switched Piezoelectric Materials. **Journal of Intelligent Material Systems and Structures**, v. 11, n. 4, p. 263–271, apr 2000. ISSN 1045389X.
- CORR, L. R.; CLARK, W. W. Comparison of low-frequency piezoelectric switching shunt techniques for structural damping. **Smart Materials and Structures**, v. 11, n. 3, p. 370–376, 2002. ISSN 09641726.
- CRAWLEY, E. F.; De Luis, J. Use of piezoelectric actuators as elements of intelligent structures. **AIAA Journal**, v. 25, n. 10, p. 1373–1385, 1987. ISSN 0001-1452.
- CRAWLEY, E. F.; LAZARUS, K. B. Induced strain actuation of isotropic and anisotropic plates. **AIAA Journal**, v. 29, n. 6, p. 944–951, 1991. ISSN 0001-1452.
- CREDE, C. E.; CAVANAUGH, R. D. **Feasibility Study of an Active Vibration Isolator for a Helicopter Rotor**. [S.l.], 1958.
- D'ASSUNCAO, D.; De Marqui Jr., C. Applied self-powered semi-passive control for a 2-degree-of-freedom aeroelastic typical section using shunted piezoelectric materials. **Journal of Intelligent Material Systems and Structures**, v. 26, n. 4, p. 373–385, mar 2015. ISSN 1045-389X.
- DAVIS, C. L.; LESIEUTRE, G. A. An actively tuned solid-state vibration absorber using capacitive shunting of piezoelectric stiffness. **Journal of Sound and Vibration**, v. 232, n. 3, p. 601–617, may 2000. ISSN 0022460X.
- De Marqui Jr., C.; ERTURK, A.; INMAN, D. J. An electromechanical finite element model for piezoelectric energy harvester plates. **Journal of Sound and Vibration**, Elsevier, v. 327, n. 1-2, p. 9–25, oct 2009. ISSN 0022460X.
- DELL'ISOLA, F.; MAURINI, C.; PORFIRI, M. Passive damping of beam vibrations through distributed electric networks and piezoelectric transducers: prototype design and experimental validation. **Smart**, v. 13, n. 2, p. 299–308, 2004. ISSN 0964-1726.

- DELPERO, T.; Di Lillo, L.; BERGAMINI, A.; ERMANNI, P. Piezoelectric Vibration Damping Using Autonomous Synchronized Switching on Inductance. In: **ASME 2011 Conference on Smart Materials, Adaptive Structures and Intelligent Systems, Volume 2**. [S.l.]: ASME, 2011. p. 427–433. ISBN 978-0-7918-5472-3.
- DOGAN, A.; UCHINO, K.; NEWNHAM, R. Composite piezoelectric transducer with truncated conical endcaps "cymbal". **IEEE Transactions on Ultrasonics, Ferroelectrics and Frequency Control**, v. 44, n. 3, p. 597–605, may 1997. ISSN 0885-3010.
- DOMKE, B. "Bo105M PAH-1," Photograph. 1988. Disponível em: <<http://www.b-domke.de/AviationImages/Rotorhead/0416.html>>.
- DONG, X.-J.; MENG, G.; PENG, J.-C. Vibration control of piezoelectric smart structures based on system identification technique: Numerical simulation and experimental study. **Journal of Sound and Vibration**, v. 297, n. 3-5, p. 680–693, nov 2006. ISSN 0022460X.
- DOSCH, J. J.; INMAN, D. J.; GARCIA, E. A Self-Sensing Piezoelectric Actuator for Collocated Control. **Journal of Intelligent Material Systems and Structures**, v. 3, n. 1, p. 166–185, 1992. ISSN 1045-389X.
- DUCARNE, J.; THOMAS, O.; DEÛ, J. F. Structural Vibration Reduction by Switch Shunting of Piezoelectric Elements: Modeling and Optimization. **Journal of Intelligent Material Systems and Structures**, v. 21, n. 8, p. 797–816, may 2010. ISSN 1045-389X.
- DÜRR, J. Integration of piezoceramic actuators in fiber-reinforced structures for aerospace applications. In: **Smart Structures and Materials: Industrial and Commercial Applications of Smart Structures Technologies**. [S.l.: s.n.], 1998. v. 3326, n. 81, p. 81–92. ISBN 4971168524.
- EDBERG, D.; BICOS, A.; FULLER, C.; TRACY, J.; FECHTER, J. **Theoretical and Experimental Studies of a Truss Incorporating Active Members**. 1992. 333–347 p.
- EDBERG, D. L.; BICOS, A. S. Design and development of passive damping concepts in advanced composite large space structures. In: **36th International SAMPE Symposium and Exhibition**. San Diego, CA, USA: [s.n.], 1991. p. 1–12.
- ELLISON, J. **Investigation of Active Materials As Driving Elements In A Hydraulic-Hybrid Actuator**. 2004. 118 p. Tese (Doutorado) — University of Maryland, 2004.
- ELVIN, N. G.; ELVIN, a. a. A General Equivalent Circuit Model for Piezoelectric Generators. **Journal of Intelligent Material Systems and Structures**, v. 20, n. 1, p. 3–9, may 2008. ISSN 1045-389X.
- ERTURK, a.; INMAN, D. J. An experimentally validated bimorph cantilever model for piezoelectric energy harvesting from base excitations. **Smart Materials and Structures**, v. 18, n. 2, p. 025009, feb 2009. ISSN 0964-1726.
- ERTURK, A.; INMAN, D. J. **PIEZOELECTRIC ENERGY HARVESTING**. [S.l.]: John Wiley & Sons, Ltd, 2011. 402 p. ISBN 9780470682548.

- ERTURK, a.; TARAZAGA, P. a.; FARMER, J. R.; INMAN, D. J. Effect of Strain Nodes and Electrode Configuration on Piezoelectric Energy Harvesting From Cantilevered Beams. **Journal of Vibration and Acoustics**, v. 131, n. 1, p. 011010, 2009. ISSN 07393717.
- FABUNMI, J. A. **Control of helicopter rotor-blade aerodynamics**. [S.l.], 1991.
- FENN, R. C. **Integrated actuation system for individual control of helicopter rotor blades**. [S.l.], 1992.
- FESZTY, D.; NITZSCHE, F. Review of Active Rotor Control Research in Canada. **International Journal of Aeronautical and Space Sciences**, v. 12, n. 2, p. 93–114, jun 2011. ISSN 2093-274X.
- FESZTY, D.; NITZSCHE, F.; KHOMUTOV, K.; LYNCH, B.; MANDER, A.; ULKER, F. Design and Instrumentation of the SHARCS Scaled Rotor with Three Independent Control Systems. In: **American Helicopter Society 64th International Annual Forum**. [S.l.: s.n.], 2008. p. 631–648.
- FLEMING, A. J.; MOHEIMANI, S. O. R. Adaptive piezoelectric shunt damping. **Smart Materials and Structures**, v. 12, n. 1, p. 36–48, 2003. ISSN 0964-1726.
- FORWARD, R. L. Electronic damping of vibrations in optical structures. **Applied Optics**, v. 18, n. 5, p. 690, mar 1979. ISSN 0003-6935.
- FREUDENBERGER, J.; GÖLLNER, J.; HEILMAIER, M.; MOOK, G.; SAAGE, H.; SRIVASTAVA, V.; WENDT, U. Materials Science and Engineering. In: GROTE, K.-H.; ANTONSSON, E. K. (Ed.). **Springer Handbook of Mechanical Engineering**. 1. ed. [S.l.]: Springer-Verlag Berlin Heidelberg, 2009. cap. 3, p. 1580.
- FRIEDMANN, P. P. On-Blade Control of Rotor Vibration, Noise, and Performance: Just Around the Corner? The 33rd Alexander Nikolsky Honorary Lecture. **Journal of the American Helicopter Society**, v. 59, n. 4, p. 1–37, 2014. ISSN 21616027.
- FRIEDMANN, P. P.; MILLOTT, T. A. Vibration reduction in rotorcraft using active control - A comparison of various approaches. **Journal of Guidance, Control, and Dynamics**, v. 18, n. 4, p. 664–673, 1995. ISSN 0731-5090. Disponível em: <<http://arc.aiaa.org/doi/10.2514/3.21445>>.
- FUERST, D.; ARNOLD, U. T.; GRAHAM, D. In-flight tuning: Wind tunnel test results and flight test preparation. In: **67th American Helicopter Society International Annual Forum**. Virginia Beach, VA, USA: [s.n.], 2011. p. 617–628.
- GIURGIUTIU, V. Review of Smart-Materials Actuation Solutions for Aeroelastic and Vibration Control. **Journal of Intelligent Material Systems and Structures**, v. 11, n. 7, p. 525–544, jul 2000. ISSN 1045389X. Disponível em: <<http://jim.sagepub.com/cgi/doi/10.1106/HYTV-NC7R-BCMM-W3CH>>.
- GUO, N.; CAWLEY, P.; HITCHINGS, D. The finite element analysis of the vibration characteristics of piezoelectric discs. **Journal of Sound and Vibration**, v. 159, n. 1, p. 115–138, nov 1992. ISSN 0022460X.
- GUYOMAR, D.; LALLART, M.; MONNIER, T. Stiffness Tuning Using a Low-Cost Semiactive Nonlinear Technique. **IEEE/ASME Transactions on Mechatronics**, v. 13, n. 5, p. 604–607, oct 2008. ISSN 1083-4435.

- GUYOMAR, D.; RICHARD, C.; GEHIN, C.; AUDIGIER, D. Low consumption damping of planar structures. In: **ISAF 2000. Proceedings of the 2000 12th IEEE International Symposium on Applications of Ferroelectrics (IEEE Cat. No.00CH37076)**. [S.l.]: IEEE, 2000. v. 2, p. 761–764. ISBN 0-7803-5940-2.
- GUYOMAR, D.; RICHARD, C.; MOHAMMADI, S. Damping Behavior of Semi-passive Vibration Control using Shunted Piezoelectric Materials. **Journal of Intelligent Material Systems and Structures**, v. 19, n. 8, p. 977–985, oct 2007. ISSN 1045-389X.
- \_\_\_\_\_. Semi-passive random vibration control based on statistics. **Journal of Sound and Vibration**, v. 307, n. 3-5, p. 818–833, nov 2007. ISSN 0022460X.
- HAGOOD, N.; Von Flotow, A. Damping of structural vibrations with piezoelectric materials and passive electrical networks. **Journal of Sound and Vibration**, v. 146, p. 243–268. 1991.
- HAGOOD, N. W.; CHUNG, W. H.; Von Flotow, A. Modelling of Piezoelectric Actuator Dynamics for Active Structural Control. **Journal of Intelligent Material Systems and Structures**, v. 1, n. 3, p. 327–354, 1990. ISSN 1045-389X.
- HAN, D.; RAHN, C. D.; SMITH, E. C. Higher harmonic pitch link loads reduction using fluidlastic isolators. **Proceedings of the Institution of Mechanical Engineers, Part G: Journal of Aerospace Engineering**, v. 228, n. 3, p. 455–469, 2014. ISSN 0954-4100.
- HANAGUD, S.; BABU, G. L. N. Smart Structures in the Control of Airframe Vibrations. **Journal of the American Helicopter Society**, v. 39, n. 2, p. 69, 1994. ISSN 00028711.
- HEEG, J. **Analytical and Experimental Investigation of Flutter Suppression by Piezoelectric Actuation**. [S.l.], 1993.
- HOLLKAMP, J. J. Multimodal Passive Vibration Suppression with Piezoelectric Materials and Resonant Shunts. **Journal of Intelligent Material Systems and Structures**, v. 5, n. 1, p. 49–57, jan 1994. ISSN 1045-389X.
- Hongli Ji; Jinhao Qiu; BADEL, A.; Yuansheng Chen; Kongjun Zhu. **Semi-active Vibration Control of a Composite Beam by Adaptive Synchronized Switching on Voltage Sources Based on LMS Algorithm**. 2009. 939–947 p.
- HOPKINS, M. A.; HENDERSON, D. A.; MOSES, R. W.; RYALL, T. G.; ZIMCIK, D. G.; Spangler, Jr., R. L. Active vibration-suppression systems applied to twin-tail buffeting. In: **Smart Structures and Materials: Industrial and Commercial Applications of Smart Structures Technologies**. San Diego, CA: [s.n.], 1998. p. 27–33.
- IEEE. **IEEE Standard on Piezoelectricity**. NY, 1987.
- JACKLIN, S. A.; BLAAS, A.; SWANSON, S. M.; TEVES, D. Second Test of a Helicopter Individual Blade Control System in the NASA Ames 40- by 80-Foot Wind Tunnel. In: **American Helicopter Society 2nd International Aeromechanics Specialists' Conference**. Bridgeport, CT: [s.n.], 1995. p. 9–26. Disponível em: <[http://halfdome.arc.nasa.gov/publications/files/Jacklin{\\\_}1995.>](http://halfdome.arc.nasa.gov/publications/files/Jacklin{\_}1995.>)

JACKLIN, S. A.; BLAAS, A.; TEVES, D.; KUBE, R. Reduction of Helicopter BVI Noise, Vibration, and Power Consumption through Individual Blade Control. In: **American Helicopter Society 51st Annual Forum Proceedings**. Fort Worth, TX: [s.n.], 1995. p. 9–11.

JACKLIN, S. a.; HABER, A.; SIMONE, G. D.; NORMAN, T. R.; KITAPLIOGLU, C.; SHINODA, P. Full-Scale Wind Tunnel Test of an Individual Blade Control System for a UH-60 Helicopter. **AHS International, 58th Annual Forum Proceedings**, p. 1103–1114, 2002.

JI, H.; Jinhao Qiu; BADEL, A.; ZHU, K. **Semi-active Vibration Control of a Composite Beam using an Adaptive SSDV Approach**. 2009. 401–412 p.

JI, H.; QIU, J.; ZHU, K.; CHEN, Y.; BADEL, A. Multi-modal vibration control using a synchronized switch based on a displacement switching threshold. **Smart Materials and Structures**, v. 18, n. 3, p. 035016, mar 2009. ISSN 0964-1726.

JI, H.; QIU, J.; ZHU, K.; BADEL, A. Two-mode vibration control of a beam using nonlinear synchronized switching damping based on the maximization of converted energy. **Journal of Sound and Vibration**, v. 329, n. 14, p. 2751–2767, 2010. ISSN 0022460X.

JOHN, S.; WERELEY, N. M.; SIROHI, J. Development of a Piezohydraulic Active Pitch Link for a Swashplateless Helicopter Rotor. **Journal of Aircraft**, v. 46, n. 1, p. 328–331, 2009. ISSN 0021-8669. Disponível em: <<http://arc.aiaa.org/doi/10.2514/1.36661>>.

KESSLER, C. Active rotor control for helicopters: Individual blade control and swashplateless rotor designs. **CEAS Aeronautical Journal**, Springer Vienna, v. 1, n. 1, p. 23–54, 2011. ISSN 18695590.

\_\_\_\_\_. Active rotor control for helicopters: Motivation and survey on higher harmonic control. **CEAS Aeronautical Journal**, v. 1, n. 1, p. 3–22, 2011. ISSN 18695590.

KHODAYARI, A.; AHMADI, A.; MOHAMMADI, S. On physical realization of the wireless semi active real time vibration control based on signal statistical behavior. **Sensors and Actuators A: Physical**, Elsevier B.V., v. 167, n. 1, p. 102–109, may 2011. ISSN 09244247.

KIM, H. W.; BATRA, A.; PRIYA, S.; UCHINO, K.; MARKLEY, D.; NEWNHAM, R. E.; HOFMANN, H. F. Energy Harvesting Using a Piezoelectric "Cymbal" Transducer in Dynamic Environment. **Japanese Journal of Applied Physics**, v. 43, n. 9A, p. 6178–6183, sep 2004. ISSN 0021-4922.

KLOEPPPEL, V.; ENENKL, B. Rotor blade control by active helicopter servo flaps. In: **International Forum on Aeroelasticity and Structural Dynamics**. Munich, Germany: [s.n.], 2005. p. Paper IF-158.

KOCBACH, J.; LUNDE, P.; VESTRHEIM, M. **FEMP - Finite Element Modeling of Piezoelectric Structures: Theory and Verification for Piezoceramic Disks**. Bergen, Norway, 1999. 38–39 p.

KONSTANZER, P.; ENENKL, B.; AUBOURG, P. A.; CRANGA, P. Recent advances in Eurocopter's passive and active vibration control. **Annual Forum Proceedings - AHS International**, v. 1, n. MAY 2002, p. 854–871, 2008. ISSN 15522938. Disponível em: <<http://www.scopus.com/inward/record.url?eid=2-s2.0-50249092061&partnerID=tZOtx>>.

- LALLART, M.; GUYOMAR, D. Self-Powered and Low-Power Piezoelectric Vibration Control Using Nonlinear Approaches. **Vibration Control**, n. September, 2010.
- LALLART, M.; LEFEUVRE, É.; RICHARD, C.; GUYOMAR, D. Self-powered circuit for broadband, multimodal piezoelectric vibration control. **Sensors and Actuators A: Physical**, v. 143, n. 2, p. 377–382, may 2008. ISSN 09244247.
- LALLART, M.; YAN, L.; RICHARD, C.; GUYOMAR, D. Damping of periodic bending structures featuring nonlinearly interfaced piezoelectric elements. **Journal of Vibration and Control**, p. 1–12, feb 2015. ISSN 1077-5463.
- LARSON, G. D.; ROGERS, P. H. State switched acoustic source. **The Journal of the Acoustical Society of America**, v. 96, n. 5, p. 3317, 1994. ISSN 00014966.
- LARSON, G. D.; ROGERS, P. H.; MUNK, W. State switched transducers: A new approach to high-power, low-frequency, underwater projectors. **The Journal of the Acoustical Society of America**, v. 103, n. 3, p. 1428, mar 1998. ISSN 00014966.
- LEADENHAM, S.; ERTURK, A. Nonlinear M-shaped broadband piezoelectric energy harvester for very low base accelerations: primary and secondary resonances. **Smart Materials and Structures**, v. 24, n. 5, p. 055021, may 2015. ISSN 0964-1726.
- LEFEUVRE, E. Semi-passive Piezoelectric Structural Damping by Synchronized Switching on Voltage Sources. **Journal of Intelligent Material Systems and Structures**, v. 17, n. 8-9, p. 653–660, may 2006. ISSN 1045-389X.
- LIANG, C.; DAVIDSON, F. M.; SCHETKY, L. M.; STRAUB, F. K. Applications of torsional shape memory alloy actuators for active rotor blade control: opportunities and limitations. In: CHOPRA, I. (Ed.). **Proc. SPIE 2717, Smart Structures and Materials 1996: Smart Structures and Integrated Systems**,. San Diego, CA: [s.n.], 1996. p. 91–100. Disponível em: <<http://proceedings.spiedigitallibrary.org/proceeding.aspx?articleid=1017341>>.
- LORBER, P. F.; PARK, C.; POLAK, D.; ONEIL, J.; WELSH, W. Active Rotor Experiments at Mach Scale Using Root Pitch IBC. In: **57th Annual AHS Forum**. Washington D.C.: [s.n.], 2001.
- MARNEFFE, B. de; PREUMONT, A. Vibration damping with negative capacitance shunts: theory and experiment. **Smart Materials and Structures**, v. 17, n. 3, p. 035015, 2008. ISSN 0964-1726.
- MCGOWAN, A.-m. R.; WILKIE, W. K.; MOSES, R. W.; LAKE, R. C.; FLORANCE, J. P.; WIESEMAN, C. D.; REAVES, M. C.; TALEGHANI, B. K.; MIRICK, P. H.; WILBUR, M. L. Aeroservoelastic and structural dynamics research on smart structures conducted at NASA Langley Research Center. In: **Proceedings of SPIE, the International Society for Optical Engineering; Industrial and commercial applications of smart structures technologies**; San Diego, CA: [s.n.], 1998. v. 3326, p. 188–201.
- MOHAMMADI, S. **Semi-passive vibration control using shunted piezoelectric materials**. 2008. Tese (Doutorado) — ISNA, 2008.

- MOKRANI, B.; RODRIGUES, G.; IOAN, B.; BASTAITS, R.; PREUMONT, A. Synchronized switch damping on inductor and negative capacitance. **Journal of Intelligent Material Systems and Structures**, 2012. ISSN 1045-389X.
- MORBITZER, D.; ARNOLD, U. T. P.; MÜLLER, M. Vibration and noise reduction through individual blade control experimental and theoretical results. In: **Proc. 24th European Rotorcraft Forum**. [S.l.: s.n.], 1998. p. 1–12.
- MOSES, R. W. Vertical-tail-buffeting alleviation using piezoelectric actuators: some results of the actively controlled response of buffet-affected tails (ACROBAT) program. In: **Proceedings of SPIE - The International Society for Optical Engineering**. [S.l.: s.n.], 1997. p. 2065–2075.
- \_\_\_\_\_. Contributions to active buffeting alleviation programs by the NASA Langley Research Center. In: **Collection of Technical Papers - AIAA/ASME/ASCE/AHS/ASC Structures, Structural Dynamics and Materials Conference**. [S.l.: s.n.], 1999. p. 1034–1042.
- NIEDERBERGER, D.; MORARI, M. An autonomous shunt circuit for vibration damping. **Smart Materials and Structures**, v. 15, n. 2, p. 359–364, apr 2006. ISSN 0964-1726.
- NITZSCHE, F. The use of smart structures in the realization of effective semi-active control systems for vibration reduction. **Journal of the Brazilian Society of Mechanical Sciences . . .**, XXXIV, p. 371–377, 2012.
- NITZSCHE, F.; BREITBACH, E. A study on the feasibility of using adaptive structures in the attenuation of vibration characteristics of rotary wings. In: **Proc. 33rd AIAA SDM Conf.** Dallas, TX: [s.n.], 1992. p. 1391–1402.
- NITZSCHE, F.; D'ASSUNCAO, D.; De Marqui Jr., C. Aeroelastic control of non-rotating and rotating wings using the dynamic stiffness modulation principle via piezoelectric actuators. **Journal of Intelligent Material Systems and Structures**, 2015. ISSN 1045-389X.
- NITZSCHE, F.; FESZTY, D. Hybrid device for vibration control. **US Patent 8,210,469**, 2008.
- NITZSCHE, F.; FESZTY, D.; GRAPPASONNI, C.; COPPOTELLI, G. Whirl-tower Open-loop Experiments and Simulations with an Adaptive Pitch Link Device for Helicopter Rotor Vibration Control. In: **54th AIAA/ASME/ASCE/AHS/ASC Structures, Structural Dynamics, and Materials Conference**. Reston, Virginia: American Institute of Aeronautics and Astronautics, 2013. ISBN 978-1-62410-223-3.
- NITZSCHE, F.; FESZTY, D.; WAECHTER, D.; BIANCHI, E.; VOUTSINAS, S.; GENNARETTI, M.; COPPOTELLI, G.; GHIRINGHELLI, G. L. The SHARCS project: smart hybrid active rotor control system for noise and vibration attenuation of helicopter rotor blades. In: **Proceedings of the 31st European Rotorcraft Forum**. Florence, Italy: [s.n.], 2005. p. 52.1–52.15.
- NITZSCHE, F.; GREWAL, A.; ZIMCIK, D. **Structural component having means for actively varying its stiffness to control vibrations**. 1999. 10 p.

- NITZSCHE, F.; HAROLD, T.; WICKRAMASINGHE, V. K. .; YONG, C.; ZIMCIK, D. G. . Development of a Maximum Energy Extraction Control for the Smart Spring. **Journal of Intelligent Material Systems and Structures**, v. 16, n. 11-12, p. 1057–1066, dec 2005. ISSN 1045-389X.
- NITZSCHE, F.; LAMMERING, R.; BREITBACH, E. Can Smart Materials Modify blade root boundary conditions to attenuate helicopter vibration? In: **Proceedings of the 4th International Conference on Adaptive Structures**. Cologne, Germany: [s.n.], 1993. p. 139–150.
- NITZSCHE, F.; ZIMCIK, D. G.; WICKRAMASINGHE, V. K.; YONG, C. Control laws for an active tunable vibration absorber designed for rotor blade damping augmentation. **The Aeronautical Journal**, v. 108, n. 1079, 2004.
- OCHOA, P.; VILLEGAS, M.; LEIDINGER, P.; FERNÁNDEZ, J. F. Vibration Characteristic of Cymbal Type Transducers. **Japanese Journal of Applied Physics**, v. 41, n. Part 1, No. 12, p. 7437–7440, dec 2002. ISSN 0021-4922.
- ONITSUKA, K.; DOGAN, A.; TRESSLER, J. F.; XU, Q.; YOSHIKAWA, S.; NEWNHAM, R. E. Metal-Ceramic Composite Transducer, the "Moonie". **Journal of Intelligent Material Systems and Structures**, v. 6, p. 447–455, 1995. ISSN 1045-389X.
- OXLEY, G.; NITZSCHE, F.; FESZTY, D. Smart Spring Control of Vibration on Helicopter Rotor Blades. **Journal of Aircraft**, v. 46, n. 2, p. 692–696, mar 2009. ISSN 0021-8669.
- PETIT, L.; LEFEUVRE, E.; RICHARD, C.; GUYOMAR, D. A broadband semi passive piezoelectric technique for structural damping. In: WANG, K.-W. (Ed.). **Proc. SPIE 5386, Smart Structures and Materials: Damping and Isolation**. [S.l.: s.n.], 2004. p. 414–425.
- QIU, Z.-c.; HAN, J.-d.; ZHANG, X.-m.; WANG, Y.-c.; WU, Z.-w. Active vibration control of a flexible beam using a non-collocated acceleration sensor and piezoelectric patch actuator. **Journal of Sound and Vibration**, v. 326, n. 3-5, p. 438–455, oct 2009. ISSN 0022460X.
- RICHARD, C.; GUYOMAR, D.; AUDIGIER, D.; CHING, G. Semi-passive damping using continuous switching of a piezoelectric device. In: HYDE, T. T. (Ed.). **Proc. of SPIE 3672, Smart Structures and Materials 1999: Passive Damping and Isolation**. Newport Beach, CA: [s.n.], 1999. v. 3672, n. March, p. 104–111.
- RICHARD, C.; GUYOMAR, D.; AUDIGIER, D.; BASSALER, H. Enhanced semi passive damping using continuous switching of a piezoelectric device on an inductor . In: HYDE, T. T. (Ed.). **Proc. SPIE 3989, Smart Structures and Materials 2000: Damping and Isolation**. [S.l.: s.n.], 2000. v. 3989, p. 288–299.
- RICHARD, C.; GUYOMAR, D.; LEFEUVRE, E. **Self-powered electronic breaker with automatic switching by detecting maxima or minima of potential difference between its power electrodes**. [S.l.]: Patent # PCT/FR2005/003000, 2007.
- RIORDAN, R. Simulated inductors using differential amplifiers. **Electronics Letters**, v. 3, n. 6, p. 291, 1967. ISSN 00135194.



ROTH, D. Advanced Vibratrion Reduction by IBC Technology. In: **Proc. 30th Eropean Rotorcraft Forum**. Marseilles, France: [s.n.], 2004. p. 17.

ROUNDY, S.; WRIGHT, P. K.; RABAEY, J. A study of low level vibrations as a power source for wireless sensor nodes. **Computer Communications**, v. 26, n. 11, p. 1131–1144, jul 2003. ISSN 01403664.

RUPP, C. J.; DUNN, M. L.; MAUTE, K. Analysis of Piezoelectric Energy Harvesting Systems with Non-linear Circuits Using the Harmonic Balance Method. **Journal of Intelligent Material Systems and Structures**, v. 21, n. 14, p. 1383–1396, sep 2010. ISSN 1045-389X.

Scarborough III, L. H.; RAHN, C. D.; SMITH, E. C.; KOUDELA, K. L. Coupled Pitch Links for Multiharmonic Isolation Using Fluidic Circuits. **Journal of the American Helicopter Society**, v. 59, n. 4, p. 1–11, 2014. ISSN 21616027.

Disponível em: <<http://openurl.ingenta.com/content/xref?genre=article{&}issn=2161-6027{&}volume=59{&}issue=4{&}spage=1{&}lpage=11{&}aula>>.

Scarborough III, L. H.; RAHN, C. D.; SMITH, E. C.; KOUDELA, K. L.; JOLLY, M. R. Impedance Tailored Fluidic Pitch Links for Passive Hub Vibration Control and Improved Rotor Efficiency. In: **5th Decennial Specialists' Meeting on AeroMechanics**. [S.l.]: American Helicopter Society International, 2014. ISBN 9781634391788.

SCHIMKE, D.; JÄNKER, P.; BLAAS, A.; KUBE, R.; SCHEWE, G.; KESSLER, C. Individual Blade Control by Servo-Flap and Blade Root Control - A Collaborative Research and Development Programme. In: **23rd European Rotorcraft Forum**. Dresden, Germany: [s.n.], 1997. v. 1, p. 46.1—46.16.

SILVA, T. M. P.; CLEMENTINO, M. A.; ERTURK, A.; De Marqui Junior, C. An experimentally validated piezoelectric nonlinear energy sink for wideband vibration attenuation. **Journal of Sound and Vibration**, Elsevier Ltd, v. 437, p. 68–78, 2018. ISSN 0022460X. Disponível em: <<https://doi.org/10.1016/j.jsv.2018.08.038>>.

SIROHI, J.; CHOPRA, I. Design and Development of a High Pumping Frequency Piezoelectric–Hydraulic Hybrid Actuator. **Journal of Intelligent Material Systems and Structures**, v. 14, n. March 2003, p. 135–147, 2003.

SODANO, H. a.; INMAN, D. J.; PARK, G. A Review of Power Harvesting from Vibration Using Piezoelectric Materials. **The Shock and Vibration Digest**, v. 36, n. 3, p. 197–205, may 2004. ISSN 05831024.

SOLTANI, P. S.; KERSCHEN, G. The nonlinear piezoelectric tuned vibration absorber. **Smart Materials and Structures**, IOP Publishing, v. 24, n. 7, p. 75015, 2015. ISSN 1361665X. Disponível em: <<http://dx.doi.org/10.1088/0964-1726/24/7/075015>>.

SPANGLER, R. L.; HALL, S. R. **Piezoelectric actuators for helicopter rotor control SSL Report**. Cambridge, MA, 1986. 1–89 p.

STRAUB, F. K.; EALEY, M. A.; SCHETKY, L. M. Application of smart materials to helicopter rotor active control. **Smart Structures and Materials 1997: Industrial and Commercial Applications of Smart Structures Technologies**, v. 3044, n. 1, p. 99–113, 1997. ISSN 0277786X.

- STRAUB, F. K.; KENNEDY, D. K.; DOMZALSKI, D. B.; HASSAN, A. A.; NGO, H.; ANAND, V.; BIRCHETTE, T. **Smart Material-Actuated Rotor Technology – SMART**. 2004. 249–260 p.
- STREHLOW, H.; RAPP, H. Smart materials for helicopter rotor active control. In: **Proc. ACARD/SMP Spec. Mtg on Smart Structures for Aircraft and Spacecraft**. Lindau: [s.n.], 1992.
- TEVES, D.; KLÖPPEL, V.; RICHTER, P. Development of Active Control Technology in the Rotating System, Flight Testing and Theoretical Investigations. In: **Proc. 18th European Rotorcraft Forum**. Avignon, France: [s.n.], 1992. p. 89–1 – 89–13.
- TIERSTEN, H. F. **Linear piezoelectric plate vibrations: Elements of the linear theory of piezoelectricity and the vibrations of piezoelectric plates**. New York, USA: Plenum Press, 1969.
- UCHINO, K.; ISHII, T. Mechanical Damper Using Piezoelectric Ceramics. **Journal of the Ceramic Society of Japan**, v. 96, n. 1116, p. 863–867, 1988. ISSN 1882-1022.
- VALLEJO, P.; LOPES, J.; RIOS-TEJADA, F.; AZOFIA, J.; Del Valle, J.; VELASCO, C.; GARCIA-MORA, L. Low Back Pain in Helicopter Pilots. In: **RTO HFM Symposium on Current Issues in Rotary Wing Operations**. San Diego, USA: [s.n.], 1998.
- VIANA, F. A. C. **AMORTECIMENTO DE VIBRAÇÕES USANDO PASTILHAS PIEZELÉTRICAS E CIRCUITOS SHUNT RESSONANTES**. 2005. Tese (Dissertação de Mestrado) — Universidade Federal de Uberlândia, 2005.
- WALL, A. S.; AFAGH, F. F.; LANGLOIS, R. G.; ZAN, S. J. Modeling Helicopter Blade Sailing: Dynamic Formulation and Validation. **Journal of Applied Mechanics**, v. 75, n. 6, p. 061004, 2008. ISSN 00218936.
- WICKRAMASINGHE, V.; CHEN, Y.; ZIMCIK, D. Experimental Evaluation of the Smart Spring Impedance Control Approach for Adaptive Vibration Suppression. **Journal of intelligent material systems and structures**, v. 19, n. 2, p. 171–179, 2008.
- WICKRAMASINGHE, V. K. **Vibration Control Approaches to Improve Dynamic Environment of Helicopter Aircrew**. 2012. Tese (PhD) — Carleton University, 2012.
- WOODS, B. K. S.; CHOI, Y. T.; WERELEY, N. M.; KOTHEA, C. S. Control system development for pneumatic artificial muscle driven active rotor systems. In: **American Helicopter Society 67th International Annual Forum**. Virginia Beach, VA: [s.n.], 2011.
- WU, D.; GUYOMAR, D.; RICHARD, C. A new global approach using a network of piezoelectric elements and energy redistribution for enhanced vibration damping of smart structure. In: SODANO, H. (Ed.). **Proc. SPIE 8688, Active and Passive Smart Structures and Integrated Systems 2013**. [S.l.: s.n.], 2013. v. 8688, p. 86880V.
- WU, S.-y. Piezoelectric shunts with a parallel R-L circuit for structural damping and vibration control. In: JOHNSON, C. D. (Ed.). **Proc. SPIE 2720, Smart Structures and Materials: Passive Damping and Isolation**. [S.l.: s.n.], 1996. v. 27201259, n. Lc, p. 259–269. ISBN 0819420956.

YANG, Y.; TANG, L. Equivalent Circuit Modeling of Piezoelectric Energy Harvesters. **Journal of Intelligent Material Systems and Structures**, v. 20, n. 18, p. 2223–2235, oct 2009. ISSN 1045-389X.

ZHAO, Y. Vibration Suppression of a Quadrilateral Plate Using Hybrid Piezoelectric Circuits. **Journal of Vibration and Control**, v. 16, n. 5, p. 701–720, mar 2010. ISSN 1077-5463.

ZHU, L.; CHEN, R.; LIU, X. Theoretical analyses of the electronic breaker switching method for nonlinear energy harvesting interfaces. **Journal of Intelligent Material Systems and Structures**, v. 23, n. 4, p. 441–451, feb 2012. ISSN 1045-389X.